

NEW METHODS FOR SURFACE RECONSTRUCTION
FROM RANGE IMAGES

A DISSERTATION
SUBMITTED TO THE DEPARTMENT OF ELECTRICAL ENGINEERING
AND THE COMMITTEE ON GRADUATE STUDIES
OF STANFORD UNIVERSITY
IN PARTIAL FULFILLMENT OF THE REQUIREMENTS
FOR THE DEGREE OF
DOCTOR OF PHILOSOPHY

Brian Lee Curless

June, 1997

© Copyright 1997 by Brian Lee Curless
All Rights Reserved

I certify that I have read this dissertation and that in my opinion it is fully adequate, in scope and in quality, as a dissertation for the degree of Doctor of Philosophy.

Marc Levoy (Principal Adviser)

I certify that I have read this dissertation and that in my opinion it is fully adequate, in scope and in quality, as a dissertation for the degree of Doctor of Philosophy.

Pat Hanrahan

I certify that I have read this dissertation and that in my opinion it is fully adequate, in scope and in quality, as a dissertation for the degree of Doctor of Philosophy.

David Heeger

Approved for the University Committee on Graduate Studies:

To Jelena

Abstract

The digitization and reconstruction of 3D shapes has numerous applications in areas that include manufacturing, virtual simulation, science, medicine, and consumer marketing. In this thesis, we address the problem of acquiring accurate range data through optical triangulation, and we present a method for reconstructing surfaces from sets of data known as range images.

The standard methods for extracting range data from optical triangulation scanners are accurate only for planar objects of uniform reflectance. Using these methods, curved surfaces, discontinuous surfaces, and surfaces of varying reflectance cause systematic distortions of the range data. We present a new ranging method based on analysis of the time evolution of the structured light reflections. Using this spacetime analysis, we can correct for each of these artifacts, thereby attaining significantly higher accuracy using existing technology. When using coherent illumination such as lasers, however, we show that laser speckle places a fundamental limit on accuracy for both traditional and spacetime triangulation.

The range data acquired by 3D digitizers such as optical triangulation scanners commonly consists of depths sampled on a regular grid, a sample set known as a range image. A number of techniques have been developed for reconstructing surfaces by integrating groups of aligned range images. A desirable set of properties for such algorithms includes: incremental updating, representation of directional uncertainty, the ability to fill gaps in the reconstruction, and robustness in the presence of outliers and distortions. Prior algorithms possess subsets of these properties. In this thesis, we present an efficient volumetric method for merging range images that possesses all of these properties. Using this method, we are able to merge a large number of range images (as many as 70) yielding seamless, high-detail models of up to 2.6 million triangles.

Acknowledgments

I would like to thank the many people who contributed in one way or another to this thesis. I owe a great debt to my adviser, Marc Levoy, who inspired me to enter the exciting arena of computer graphics. The road to a Ph.D. is usually a bumpy one, and mine was no exception. In the end, Marc's unerring intuitions and infectious enthusiasm sent me down a very rewarding path. I would also thank the members of my reading committee, Pat Hanrahan and David Heeger, for their interest in this work. Early discussions with Pat while developing the ideas about space carving in Chapter 6 were especially helpful.

Next, I would like to thank my colleagues in the Stanford Computer Graphics Laboratory. As members of the 3D Fax Project, Greg Turk, Venkat Krishnamurthy, and Brian Freyburger have been particularly supportive. Brian developed the ideas for space carving with triangulation scanners (Section 6.4). In addition, discussions with Phil Lacroute were crucial to making the volumetric algorithm efficient (Section 7.2). Homan Igehy wrote the fast rasterizer used for range image resampling (Section 7.2), and Matt Pharr wrote the accessibility shader used to create the rendering in Figure 8.6b. Bill Lorensen provided marching cubes tables and mesh decimation software and managed the production of the 3D hardcopy.

Special thanks go to Charlie Orgish and John Gerth for maintaining sanity among the machines (and therefore the students) in the graphics laboratory. Sarah Bezier and Ada Glucksman cheerfully shielded me from the inner-workings of University bureaucracy.

Cyberware Laboratories provided the scanner used to collect data in this thesis. I am particularly grateful to David Addleman and George Dabrowski at Cyberware for their assistance and encouragement. Funding for this work came from the National Science Foundation under contract CCR-9157767 and from Interval Research Corporation.

I would like to thank my parents, Richard and Diane, my brother, Chris, and my sisters,

Ann and Laura. With their support, I knew I would persevere through the years. Finally, my deepest gratitude goes to my wife, Jelena. She calmed me in moments of panic and had faith in me during times of doubt. I dedicate this thesis to her.

Contents

	v
Abstract	vii
Acknowledgments	ix
1 Introduction	1
1.1 Applications	2
1.1.1 Reverse engineering	2
1.1.2 Collaborative design	2
1.1.3 Inspection	3
1.1.4 Special effects, games, and virtual worlds	3
1.1.5 Dissemination of museum artifacts	3
1.1.6 Medicine	3
1.1.7 Home shopping	4
1.2 Methods for 3D Digitization	4
1.3 Surface reconstruction from range images	9
1.3.1 Range images	9
1.3.2 Surface reconstruction	10
1.4 The 3D Fax Project	12
1.5 Contributions	15
1.6 Organization	16
2 Optical triangulation: limitations and prior work	18
2.1 Triangulation Configurations	19
2.1.1 Structure of the illuminant	19

2.1.2	Type of illuminant	20
2.1.3	Sensor	21
2.1.4	Scanning method	21
2.2	Limitations of traditional methods	21
2.2.1	Geometric intuition	22
2.2.2	Quantifying the error	26
2.2.3	Focusing the beam	28
2.2.4	Influence of laser speckle	30
2.3	Prior work on triangulation error	36
3	Spacetime Analysis	38
3.1	Geometric intuition	38
3.2	A complete derivation	40
3.3	Generalizing the geometry	44
3.4	Influence of laser speckle	46
3.5	A Signal Processing Perspective	51
3.5.1	Ideal triangulation impulse response	51
3.5.2	Filtering, noise, sampling, and reconstruction	53
3.5.3	The spacetime spectrum	54
3.5.4	Widening the laser sheet	56
3.5.5	Improving resolution	58
4	Spacetime analysis: implementation and results	60
4.1	Hardware	60
4.2	The spacetime algorithm	62
4.2.1	Fast rotation of the spacetime image	65
4.2.2	Interpolating the spacetime volume	69
4.3	Results	70
4.3.1	Reflectance correction	70
4.3.2	Shape correction	71
4.3.3	Speckle	73
4.3.4	Complex objects	73

4.3.5	Remaining sources of error	77
5	Surface estimation from range images	78
5.1	Prior work in surface reconstruction from range data	79
5.1.1	Unorganized points: polygonal methods	79
5.1.2	Unorganized points: implicit methods	79
5.1.3	Structured data: polygonal methods	80
5.1.4	Structured data: implicit methods	80
5.1.5	Other related work	81
5.2	Range images, range surfaces, and uncertainty	82
5.3	A probabilistic model	85
5.4	Maximum likelihood estimation	86
5.5	Unifying the domain of integration	89
5.6	Calculus of variations	95
5.7	A minimization solution	99
5.8	Discussion	100
6	A New Volumetric Approach	106
6.1	Merging observed surfaces	106
6.1.1	A one-dimensional Example	108
6.1.2	Restriction to vicinity of surface	110
6.1.3	Two and three dimensions	111
6.1.4	Choosing surface weights	114
6.2	Hole filling	116
6.2.1	A hole-filling algorithm	116
6.2.2	Carving from backdrops	118
6.3	Sampling, conditioning, and filtering	121
6.3.1	Voxel resolution and tessellation criteria	121
6.3.2	Conditioning the implicit function	126
6.3.3	Mesh filtering vs. anti-aliasing in hole fill regions	130
6.4	Limitations of the volumetric method	130
6.4.1	Thin surfaces	131

6.4.2	Bridging sharp corners	133
6.4.3	Space carving	134
7	Fast algorithms for the volumetric method	139
7.1	Run-length encoding	139
7.2	Fast volume updating	140
7.2.1	Scanline alignment	141
7.2.2	Resampling the range image	143
7.2.3	Updating the volume	144
7.2.4	A shear-warp factorization	144
7.2.5	Binary depth trees	147
7.2.6	Efficient RLE transposes	148
7.3	Fast surface extraction	149
7.4	Asymptotic Complexity	150
7.4.1	Storage	151
7.4.2	Computation	153
8	Results of the volumetric method	157
8.1	Hardware Implementation	157
8.2	Aligning range images	158
8.3	Results	159
9	Conclusion	168
9.1	Improved triangulation	168
9.2	Volumetrically combining range images	169
9.3	Future work	169
9.3.1	Optimal triangulation	170
9.3.2	Improvements for volumetric surface reconstruction	171
9.3.3	Open problems in surface digitization	172
A	Proof of Theorem 5.1	175
B	Stereolithography	178
	Bibliography	182

List of Tables

- 3.1 Symbol definitions for spacetime analysis. 41
- 7.1 Symbol definitions for complexity analysis. 150
- 8.1 Statistics for reconstructions. 167

List of Figures

1.1	Taxonomy of active range acquisition methods.	5
1.2	Optical triangulation and range imaging.	9
1.3	Range images taken from multiple viewpoints	11
1.4	Data flow in 3D Fax Project	13
1.5	Photograph of the Cyberware scanner.	14
2.1	Optical triangulation geometry	19
2.2	Range errors due to reflectance discontinuities	23
2.3	Range errors due to shape variations	23
2.4	Range error due to sensor occlusion	24
2.5	Image of a rough object formed with coherent light.	25
2.6	Influence of laser speckle on traditional triangulation.	25
2.7	Plot of errors due to reflectance discontinuities	26
2.8	Plot of errors due to corners	27
2.9	Gaussian beam optics.	28
2.10	Imaging geometry and coordinate systems	31
2.11	Speckle due to a diffraction through a lens	32
3.1	Spacetime mapping of a Gaussian illuminant	39
3.2	Triangulation scanner coordinate system.	40
3.3	Spacetime image of the Gaussian illuminant	42
3.4	From geometry to spacetime image to range data	43
3.5	Influence of laser speckle on spacetime triangulation.	48

3.6	Speckle contributions at the sensor due to a moving coherent illuminant with square cross-section.	49
3.7	Spacetime speckle error for a coherent illuminant with square cross-section.	50
3.8	Formation of the spacetime image.	52
3.9	The spacetime spectrum.	55
3.10	Spacetime spectrum for a line.	57
4.1	From range video to range image.	61
4.2	Method for optical triangulation range imaging with spacetime analysis	63
4.3	Run-length encoded spacetime scanline.	65
4.4	Fast RLE rotation.	66
4.5	Reconstruction: send vs. gather.	66
4.6	Building a rotated RLE scanline.	68
4.7	Interpolation of spacetime image data	69
4.8	Measured error due to reflectance step	70
4.9	Reflectance card	71
4.10	Measured error due to corner	72
4.11	Depth discontinuities and edge curl	72
4.12	Shape ribbon	73
4.13	Distribution of range errors over a planar target.	74
4.14	Model tractor	75
4.15	Model alien	76
5.1	From range image to range surfaces	82
5.2	Range imaging frustums.	84
5.3	Range errors for traditional triangulation with two-dimensional imaging.	85
5.4	Range images and a candidate surface	87
5.5	Differential area relations for reparameterization.	90
5.6	Ray density and vector fields in 2D	93
5.7	Aligned range images	103
6.1	Unweighted signed distance functions in 3D	107

6.2	Signed distance and weight functions in one dimension	108
6.3	Combination of signed distance and weight functions in two dimensions. . .	111
6.4	Pseudocode for volumetric integration	112
6.5	Sampling the range surface to update the volume	113
6.6	Discrete isosurface extraction	113
6.7	Dependence of surface sampling rate on view direction.	115
6.8	Tapering vertex weights for surface blending.	116
6.9	Volumetric grid with space carving and hole filling	117
6.10	A hole-filling visualization.	119
6.11	Carving from backdrops	120
6.12	Tessellation artifacts near a planar edge.	127
6.13	Isosurface artifacts and conditioning functions.	129
6.14	Limitation on thin surfaces.	131
6.15	Using the MIN() function to merge opposing distance ramps.	132
6.16	Limitations due to sharp corners.	133
6.17	Intersections of viewing shafts for space carving.	134
6.18	Protrusion generated during space carving.	135
6.19	Errors in topological type due to space carving.	135
6.20	Aggressive strategies for space carving using a range sensor with a single line of sight per sample.	136
6.21	Conservative strategy for space carving with a triangulation range sensor. .	138
6.22	Aggressive strategies for space carving with a triangulation range sensor. .	138
7.1	Overview of range image resampling and scanline order voxel updates . . .	140
7.2	Orthographic range image resampling.	141
7.3	Perspective range image resampling.	142
7.4	Transposing the volume for scanline alignment.	143
7.5	A shear warp method for parallel projection	145
7.6	Correction factor for sheared distances.	145
7.7	Shear-warp for perspective projection.	146
7.8	Binary depth tree	147

7.9	Fast transpose of a multi-valued RLE image.	149
7.10	Carving from “difficult” surfaces.	152
7.11	Storage complexity with and without backdrops.	153
8.1	Noise reduction by merging multiple scans.	159
8.2	Merging range images of a drill bit	161
8.3	Reconstruction of a dragon – Part I of II.	162
8.4	Reconstruction of a dragon – Part II of II.	163
8.5	From the original to a 3D hardcopy of the “Happy Buddha” – Part I of II.	164
8.6	From the original to a 3D hardcopy of the “Happy Buddha” – Part II of II.	165
8.7	Wireframe and shaded renderings of the Happy Buddha model.	166
B.1	The stereolithography process.	179
B.2	Contouring due to layered manufacture.	180
B.3	Supports for stereolithography manufacturing.	181

Chapter 1

Introduction

Methods to digitize and reconstruct the shapes of complex three dimensional objects have evolved rapidly in recent years. The speed and accuracy of digitizing technologies owe much to advances in the areas of physics and electrical engineering, including the development of lasers, CCD's, and high speed sampling and timing circuitry. Such technologies allow us to take detailed shape measurements with precision better than 1 part per 1000 at rates exceeding 10,000 samples per second. To capture the complete shape of an object, many thousands, sometimes millions of samples must be acquired. The resulting mass of data requires algorithms that can efficiently and reliably generate computer models from these samples.

In this thesis, we address methods of both digitizing and reconstructing the shapes of complex objects. The first part of the thesis is concerned with a popular range scanning method known as optical triangulation. We show that traditional approaches to optical triangulation have fundamental limitations that can be overcome with a novel method called *spacetime analysis*. The second part of this thesis concerns reconstruction of surfaces from range data. Many rangefinders, including optical triangulation scanners, can acquire regular, dense samplings called *range images*. We describe a new method for building complex models from range images in a way that satisfies a number of desirable properties.

In this chapter, we describe some of the applications of 3D shape acquisition (Section 1.1) followed by a description of the variety of acquisition methods (Section 1.2). In

Section 1.3, we pose the problem of surface reconstruction from range images. In Section 1.4, we place the goals of this thesis in the context of Stanford's 3D Fax Project. In Section 1.5, we describe the contributions of this thesis, and in the last section we outline the remainder of the thesis.

1.1 Applications

The applications of 3D shape digitization and reconstruction are wide-ranging and include manufacturing, virtual simulation, scientific exploration, medicine, and consumer marketing.

1.1.1 Reverse engineering

Many manufacturable parts are currently designed with Computer Aided Design (CAD) software. However, in some instances, a mechanical part exists and belongs to a working system but has no computer model needed to regenerate the part. This is frequently the case for machines currently in service that were designed before the advent of computers and CAD systems, as well as for parts that were hand-tuned to fit into existing machinery. If such a part breaks, and neither spare parts nor casting molds exist, then it may be possible to remove a part from a working system and digitize it precisely for re-manufacture.

1.1.2 Collaborative design

While CAD tools can be helpful in designing parts, in some cases the most intuitive design method is physical interaction with the model. This is especially true when the model must have esthetic appeal, such as the exteriors of consumer products ranging from perfume bottles to automobiles. Frequently, companies employ sculptors to design these models in a medium such as clay. Once the sculpture is ready, it may be digitized and reconstructed on a computer. The computer model is then suitable for dissemination to local engineers or remote clients for careful review, or it may serve as a starting point for constructing a CAD model suitable for manufacture.

1.1.3 Inspection

After a manufacturer has created a computer model for a part either by shape digitization of a physical model or through interactive CAD design, he has a variety of options for creating this part, both as a working prototype and as a starting point for mass manufacture. Ultimately, the dimensions of the final manufactured part must fall within some tolerances of the original computer model. In this case, shape digitization can aid in determining where and to what extent the computer model and the shape of the actual part differ. These differences can serve as a guide for modifying the manufacturing process until the part is acceptable.

1.1.4 Special effects, games, and virtual worlds

Synthetic imagery is playing an increasingly prominent role in creating special effects for cinema. In addition, video games and gaming hardware are moving steadily toward interactive 3D graphics. Virtual reality as a means of simulating worlds of experience is also growing in popularity. All of these applications require 3D models that may be taken from real life or from sculptures created by artists. Digitizing the shapes of physical models will be essential to populating these synthetic environments.

1.1.5 Dissemination of museum artifacts

Museum artifacts represent one-of-a-kind objects that attract the interest of scientists and lay people world-wide. Traditionally, to visualize these objects, it has been necessary to visit potentially distant museums or obtain non-interactive images or video sequences. By digitizing these parts, museum curators can make them available for interactive visualization. For scientists, computer models afford the opportunity to study and measure artifacts remotely using powerful computer tools.

1.1.6 Medicine

Applications of shape digitization in medicine are wide ranging as well. Prosthetics can be custom designed when the dimensions of the patient are known to high precision. Plastic surgeons can use the shape of an individual's face to model tissue scarring processes and

visualize the outcomes of surgery. When performing radiation treatment, a model of the patient's shape can help guide the doctor in directing the radiation accurately.

1.1.7 Home shopping

As the World Wide Web provides a backbone for interaction over the Internet, commercial vendors are taking advantage of the ability to market products through this medium. By making 3D models of their products available over the Web, vendors can allow the customer to explore their products interactively. Standards for disseminating 3D models over the web are already underway (e.g., the Virtual Reality Modeling Language (VRML)).

1.2 Methods for 3D Digitization

A vast number of shape acquisition methods have evolved over the last century. These methods follow two primary directions: passive and active sensing. Passive approaches do not interact with the object, whereas active methods make contact with the object or project some kind of energy onto it. The computer vision research community is largely focused on passive methods that extract shape from one or more digitized images. Computer vision approaches include shape-from-shading for single images, stereo triangulation for pairs of images, and optical flow and factorization methods for video streams. While these methods require very little special purpose hardware, they typically do not yield dense and highly accurate digitizations required of a number of applications.

The remainder of this section summarizes the active range acquisition methods. Figure 1.1 introduces a taxonomy which we follow. This taxonomy is by no means comprehensive; rather, it is intended to introduce the reader to the variety of methods available.

Among active sensing methods, we can discern two different approaches: contact and non-contact sensors. Contact sensors are typically touch probes that consist of jointed arms or pulley-mounted tethers attached to a narrow pointer. The angles of the arms or the lengths of the tethers indicate the location of the pointer at all times. By touching the pointer to the surface of the object, a contact event is signaled and the position of the pointer is recorded. Touch probes come in a wide range of accuracies as well as costs. Coordinate Measuring

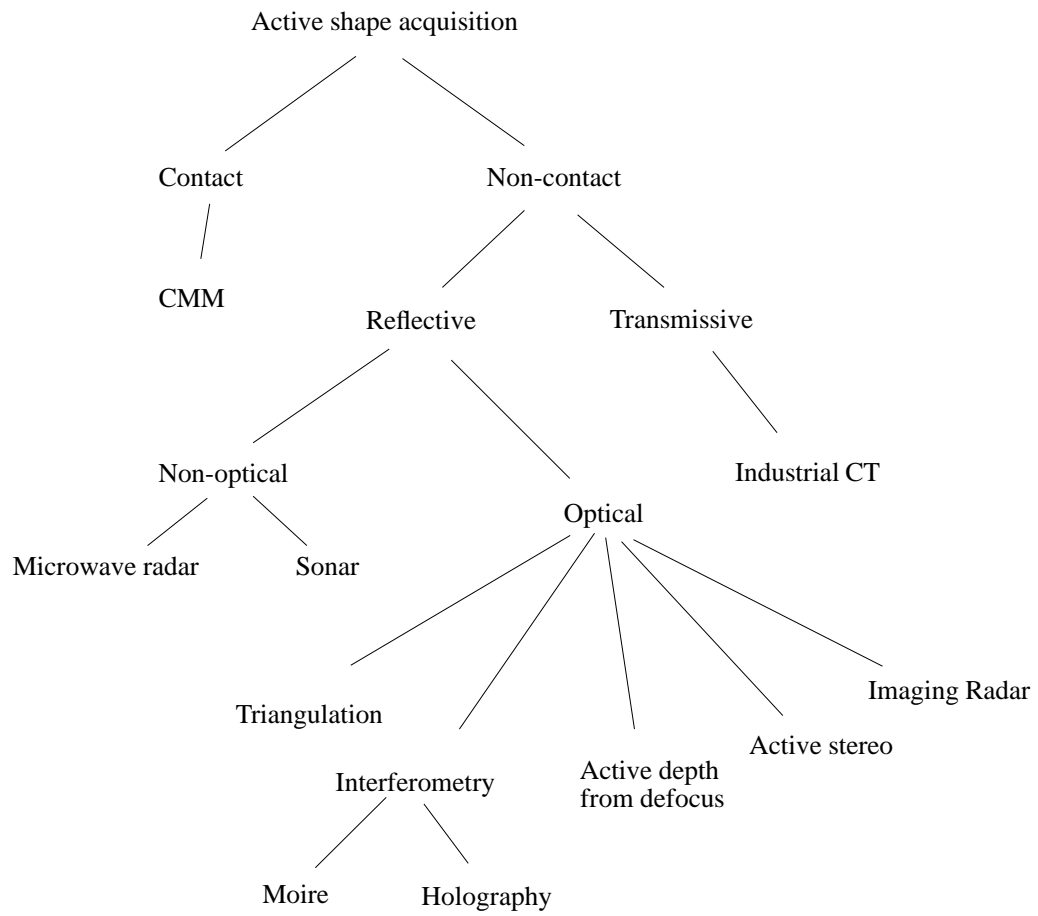


Figure 1.1: Taxonomy of active range acquisition methods.

Machines (CMM's) are extremely precise (and costly), and they are currently the standard tool for making precision shape measurements in industrial manufacturing. The main drawbacks of touch probes are:

- They are slow.
- They can be clumsy to manipulate.
- They usually require a human operator.
- They must make contact with the surface, which may be undesirable for fragile objects.

Active, non-contact methods generally operate by projecting energy waves onto an object followed by recording the transmitted or reflected energy. A powerful transmissive approach for shape capture is industrial computer tomography (CT). Industrial CT entails bombarding an object with high energy x-rays and measuring the amount of radiation that passes through the object along various lines of sight. After back projection or Fourier projection slice reconstruction, the result is a high resolution volumetric description of the density of space in and around the object. This volume is suitable for direct visualization or surface reconstruction. The principal advantages of this method over reflective methods are: it is largely insensitive to the reflective properties of the surface, and it can capture the internal cavities of an object that are not visible from the outside. The principal disadvantages of industrial CT scanners are:

- They are very expensive.
- Large variations in material densities (e.g., wood glued to metal) can degrade accuracy.
- They are potentially very hazardous due to the use of radioactive materials.

Among active, reflection methods for shape acquisition, we subdivide into two more categories: non-optical and optical approaches. Non-optical approaches include sonar and

microwave radar (Radio Detecting And Ranging), which typically measure distances to objects by measuring the time required for a pulse of sound or microwave energy to bounce back from an object. Amplitude or frequency modulated continuous energy waves can also be used in conjunction with phase or frequency shift detectors. Sonar range sensors are typically inexpensive, but they are also not very accurate and do not have high acquisition speeds. Microwave radar is typically intended for use with long range remote sensing, though close range optical radar is feasible, as described below.

The last category in our taxonomy consists of active, optical reflection methods. For these methods, light is projected onto an object in a structured manner, and by measuring the reflections from the object, we can determine shape. In contrast to passive and non-optical methods, many active optical rangefinders can rapidly acquire dense, highly accurate range samplings. In addition, they are safer and less expensive than industrial CT, with the limitation that they can only acquire the optically visible portions of the surface. Several surveys of optical rangefinding methods have appeared in the literature; the survey in [Besl 1989] is especially comprehensive. These optical methods include imaging radar, interferometry, active depth-from-defocus, active stereo, and triangulation.

Imaging radar is the same as microwave radar operating at optical frequencies. For large objects, a variety of imaging radars have been demonstrated to give excellent results. For smaller objects, on the order of one meter in size, attaining 1 part per 1000 accuracy with time-of-flight radar requires very high speed timing circuitry, because the time differences to be detected are in the femtosecond (10^{-12} second) range. A few amplitude and frequency modulated radars have shown promise for close range distance measurements.

Interferometric methods operate by projecting a spatially or temporally varying periodic pattern onto a surface, followed by mixing the reflected light with a reference pattern. The reference pattern demodulates the signal to reveal the variations in surface geometry. Moire interferometry involves the projection of coarse, spatially varying light patterns onto the object, whereas holographic interferometry typically relies on mixing coherent illumination with different wave vectors. Moire methods can have phase discrimination problems when the surface does not exhibit smooth shape variations. This difficulty usually places a limit on the maximum slope the surface can have to avoid ranging errors. Holographic methods typically yield range accuracy of a fraction of the light wavelength over microscopic fields

of view.

Active depth from focus operates on the principal that the image of an object is blurred by an amount proportional to the distance between points on the object and the in-focus object plane. The amount of blur varies across the image plane in relation to the depths of the imaged points. This method has evolved as both a passive and an active sensing strategy. In the passive case, variations in surface reflectance (also called surface texture) are used to determine the amount of blurring. Thus, the object must have surface texture covering the whole surface in order to extract shape. Further, the quality of the shape extraction depends on the sharpness of surface texture. Active methods avoid these limitations by projecting a pattern of light (e.g., a checkerboard grid) onto the object. Most prior work in active depth from focus has yielded moderate accuracy (up to one part per 400 over the field of view [Nayar et al. 1995]).

Active stereo uses two or more cameras to observe features on an object. If the same feature is observed by two cameras, then the two lines of sight passing through the feature point on each camera's image plane will intersect at a point on the object. As in the depth from defocus method, this approach has been explored as both a passive and an active sensing strategy. Again, the active method operates by projecting light onto the object to avoid difficulties in discerning surface texture.

Optical triangulation is one of the most popular optical rangefinding approaches. Figure 1.2a shows a typical system configuration in two dimensions. The location of the center of the reflected light pulse imaged on the sensor corresponds to a line of sight that intersects the illuminant in exactly one point, yielding a depth value. The shape of the object is acquired by translating or rotating the object through the beam or by scanning the beam across the object. Due to the finite width of the light beam, inaccuracies arise when the surface exhibits significant changes in reflectance and shape. The first part of this thesis is concerned with describing the range accuracy limitations inherent in traditional methods, followed by the introduction of a new method of optical triangulation, called spacetime analysis, which substantially removes these limitations.

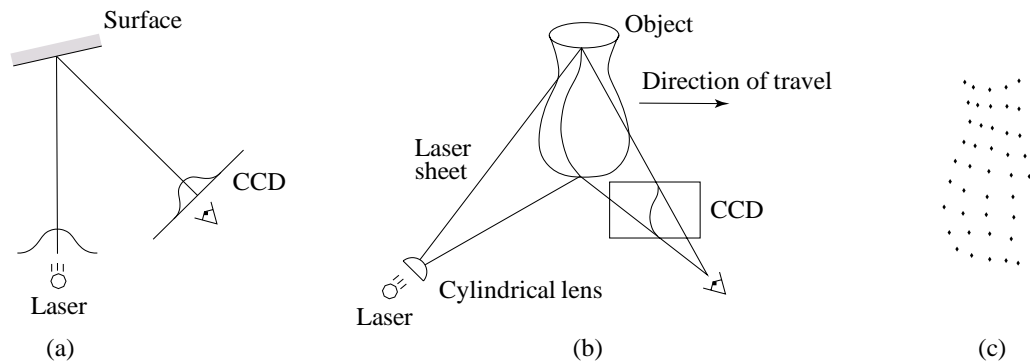


Figure 1.2: Optical triangulation and range imaging. (a) In 2D, a narrow laser beam illuminates a surface, and a linear sensor images the reflection from an object. The center of the image pulse maps to the center of the laser, yielding a range value. (b) In 3D, a laser stripe triangulation scanner first spreads the laser beam into a sheet of light with a cylindrical lens. The CCD observes the reflected stripe from which a depth profile is computed. The object sweeps through the field of view, yielding a range image. Other scanner configurations rotate the object to obtain a cylindrical scan or sweep a laser beam or stripe over a stationary object. (c) A range image obtained from the scanner in (b) is a collection of points with regular spacing.

1.3 Surface reconstruction from range images

In this section, we describe the goal of the second part of this thesis: surface reconstruction from range images. We begin with a brief explanation of range imaging.

1.3.1 Range images

Many active optical rangefinders sample the shape of an object along a set of regularly spaced lines of sight, yielding a grid of depths known as a range image. These rangefinders may be thought of as range cameras; i.e., they take pictures of a scene, but each image pixel contains a depth instead of a color. While conventional cameras typically take pictures that correspond to a perspective projection, the imaging geometry of rangefinders may vary widely, as discussed in Chapter 5. Figure 1.2 illustrates how a laser stripe triangulation scanner can acquire a range image. If we think of a surface as being described by a function, f , then a range image, \hat{f} is a sampling of this surface, where each sample $\hat{f}(j, k)$ is the observed distance to the surface as seen along the line of sight indexed by (j, k) .

1.3.2 Surface reconstruction

Each range image provides a detailed description of an object as seen from one point of view. Before attempting to reconstruct the entire shape of an object, we require multiple range images. As depicted in Figure 1.3, a single range image generally cannot acquire all sides of an object, thus requiring multiple range images to be taken. In fact, many objects are too complex to be captured by a small number of range images taken, for instance, from mutually orthogonal directions and their opposites (i.e., from the six faces of a cube). Due to self occlusions, an object may require a large number of range scans to see every visible point¹. In some cases, points on the surface of an object are shiny enough to reflect most light that strikes them in a mirror-like fashion. Such points may only be seen when observed from particular angles, requiring multiple range images in order to see all of them.

Taking many range images offers two additional advantages: noise reduction and improved sampling rate. Real sensors suffer from noise due to a variety of causes including laser speckle and CCD scanline jitter. Multiple noisy sightings of a point on a surface can contribute to a reduced-variance estimate of the location of that point. Also, portions of a surface observed at a grazing angle from one point of view tend to be undersampled. Taking many range images increases the likelihood of sampling the surface when it is directly facing the sensor.

Since we require multiple range images to capture the shape of an object, we must devise a method to reconstruct a single description of this shape. The problem of reconstructing a surface from range images can be stated as follows:

Given a set of p aligned, noisy range images, $\hat{f}_1, \dots, \hat{f}_p$, find the 2D manifold that most closely approximates the points contained in the range images.

Note that in order to merge a set of range images into a single description of an object, it is necessary to place them all in the same coordinate system; i.e., they must be registered or aligned with respect to each other. The alignment may arise from prior knowledge of the pose of the rangefinder when acquiring the range image, or it may be computed using one

¹Indeed, for some scanning technologies, points on the visible surface of an object may be “unacquirable” due to the geometry of the sensor. Optical triangulation scanners, for example, cannot acquire concavities inaccessible to a triangular probe with probe angle defined by the optical triangulation angle.

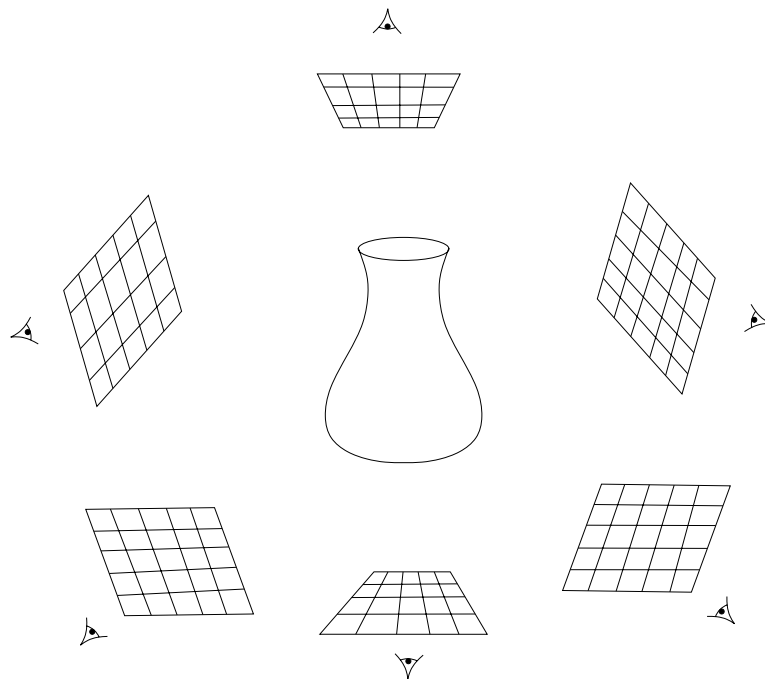


Figure 1.3: Range images taken from multiple viewpoints

of a number of algorithms. We assume in this thesis that the range images are aligned to a high degree of accuracy before we attempt to merge them.

A number of algorithms have been proposed for surface reconstruction from range images. Our experience with these algorithms has led us to develop a list of desirable properties:

- *Representation of range uncertainty.* The data in range images typically have asymmetric error distributions with primary directions along sensor lines of sight. The method of surface reconstruction should reflect this fact.
- *Utilization of all range data,* including redundant observations of each object surface. If properly used, this redundancy will provide a reduction of sensor noise.
- *Incremental and order independent updating.* Incremental updates allow us to obtain a reconstruction after each scan or small set of scans and allow us to choose the next best orientation for scanning. Order independence is desirable to ensure that results

are not biased by earlier scans. Together, incremental and order independent updating allows for straightforward parallelization.

- *Time and space efficiency.* Complex objects may require many range images in order to build a detailed model. The range images and the model must be represented efficiently and processed quickly to make the algorithm practical.
- *Robustness.* Outliers and systematic range distortions can create challenging situations for reconstruction algorithms. A robust algorithm needs to handle these situations without catastrophic failures such as holes in surfaces and self-intersecting surfaces.
- *No restrictions on topological type.* The algorithm should not assume that the object is of a particular genus. Simplifying assumptions such as “the object is homeomorphic to a sphere” yield useful results in only a restricted class of problems.
- *Ability to fill holes in the reconstruction.* Given a set of range images that do not completely cover the object, the surface reconstruction will necessarily be incomplete. For some objects, no amount of scanning would completely cover the object, because some surfaces may be inaccessible to the sensor. In these cases, we desire an algorithm that can automatically fill these holes with plausible surfaces, yielding a model that is both “watertight” and esthetically pleasing.

Prior algorithms possess subsets of these properties. In this thesis, we present an efficient volumetric method for merging range images that possesses all of these properties.

1.4 The 3D Fax Project

The work described in this thesis fits into a framework for digitizing the shape and appearance of objects: the 3D Fax Project at Stanford University. Figure 1.4 shows the flow of data in this framework from scanning through construction of CAD models and manufacture of a hardcopy.

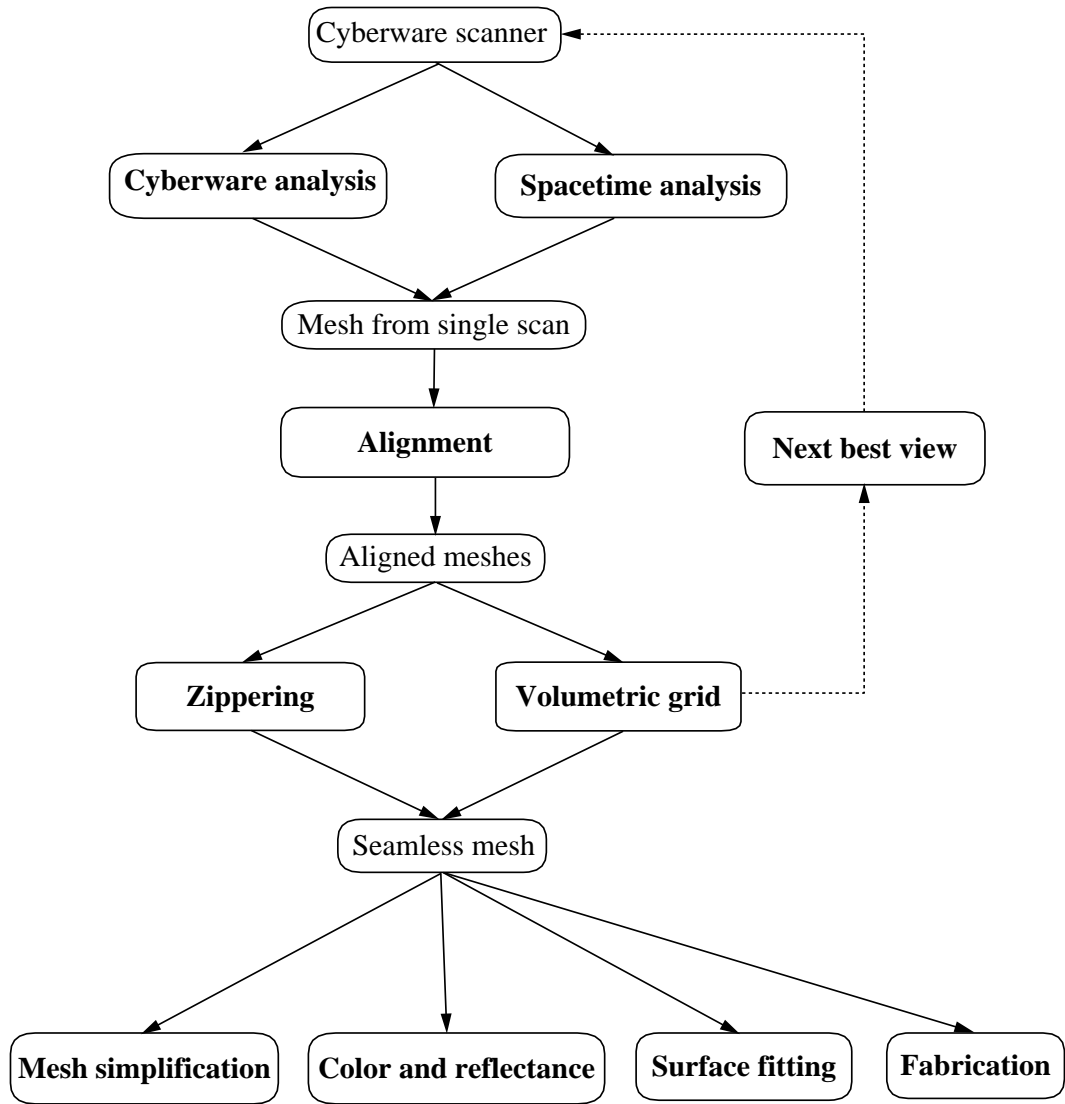


Figure 1.4: Data flow in the 3D Fax Project



Figure 1.5: A photograph of the Cyberware Model MS 3030 optical triangulation scanner used for acquiring range images in this thesis.

The input device for this project is an optical triangulation scanner manufactured by Cyberware Laboratories (pictured in Figure 1.5). The scanner performs triangulation in hardware using a traditional method of analysis which is prone to range errors. Alternatively, we can apply a triangulation method called “spacetime analysis” to minimize these range artifacts, as described in this thesis.

The range data obtained from the scanner is in the form of a dense range image. By repeatedly scanning an object from different points of view, we obtain a set of range images that are not necessarily aligned with respect to one another. Using an iterated closest point algorithm developed in [Besl & McKay 1992] and modified for aligning partial shape digitizations in [Turk & Levoy 1994], we transform the scans into a common coordinate system.

After alignment, the range images provide the starting point for performing a surface reconstruction. One method for merging the range images into a single surface is called “zippering.” This method operates directly on triangle meshes, and while it is well-behaved for relatively smooth surfaces, it has been show to fail in regions of high curvature. An

alternative method is to merge the meshes in a volumetric domain followed by an isosurface extraction. This method has a number of advantages over the zipping approach, as will be shown in this thesis.

After merging a set of range images, it is typically the case for a complex object that some portion of the object remains to be digitized. The problem of deciding how best to orient the object relative to the scanner is the so-called “next best view” problem, an active area of research in the 3D Fax Project. We believe that defining the emptiness of space around an object using the volumetric method described in this thesis will play an important role in developing an effective next best view algorithm.

Once a satisfactory model is obtained, it is suitable for a number of operations including simplification, color texturing, smooth-surface fitting, and rapid prototyping. The meshes generated by the merging process are typically dense, with vertices spaced less than 0.5 mm apart. Objects containing large flat areas may be represented with much fewer triangles, thus the need for mesh simplification algorithms. Color data may also be collected for scanned objects, and one research goal is to derive illumination independent body color and “shininess” for each point on the surface. In addition, the merged meshes are triangular tessellations, but CAD packages for manufacture and animation typically require NURBS surfaces. To address this need, Krishnamurthy & Levoy [1996] have developed a method for interactively creating tensor product B-spline surfaces from dense polygonal meshes. Finally, the models generated by the volumetric method of merging meshes are generally manufacturable with rapid prototyping technology. Near the end of this thesis, we describe the manufacture of one of our models using stereolithography.

1.5 Contributions

The contributions of this thesis are two-fold. First, we describe and demonstrate a new method for optical triangulation, known as spacetime analysis. We show that this new method yields:

- Immunity to reflectance variations
- Immunity to shape variations

We also show that the influence of laser speckle remains a fundamental limit to the accuracy of both traditional and spacetime triangulation methods.

Second, we describe a new, volumetric algorithm for building complex models from range images. We demonstrate the following:

- The method is incremental, order independent, represents sensor uncertainty, and behaves robustly.
- The method is optimal under a set of reasonable assumptions.
- Extending the method to qualify the emptiness of space around an object permits us to construct hole-free models.
- Through careful choice of data structures and resampling methods, the method can be made time and space efficient.

Using the volumetric algorithm to combine the range images generated with our optical triangulation method, we have constructed the most complex computer models published to date. In addition, because these models are hole-free, we are able demonstrate their manufacturability using a layered manufacturing method called stereolithography.

1.6 Organization

Chapter 2 begins with a more detailed description of optical triangulation methods. We then characterize the primary sources of error in traditional optical triangulation and conclude with a discussion of some previous work.

Next, in Chapter 3, we develop a new method for optical triangulation called “spacetime analysis”. We show how this method corrects for errors due to changes in reflectance and shape, but is still limited in accuracy by laser speckle.

In Chapter 4, we describe an efficient implementation of the spacetime method, and we demonstrate results using an existing optical triangulation scanner modified to allow digitization of the imaged light reflections. Portions of Chapters 2-4 are described in [Curless & Levoy 1995].

The next four chapters concern the problem of surface reconstruction from range images. In Chapter 5, we describe some previous work in the area, and then provide a mathematical framework that motivates a new method for surface reconstruction. This new method shows that the maximum likelihood surface is an isosurface of a function in 3-space.

In Chapter 6, we develop a new volumetric algorithm for surface reconstruction from range images. This algorithm utilizes the mathematical framework described in the previous chapter and extends it to allow description of the occupancy of space around the surface. This extension leads to a method for generating models without boundaries. In addition, we discuss some of the limitations of the volumetric method and suggest some possible solutions.

The potential storage and computational costs of the volumetric method require implementation of an efficient algorithm. In Chapter 7, we describe one such algorithm and then analyze its asymptotic complexity.

Next, in Chapter 8, we demonstrate the results of reconstructing range surfaces using the volumetric method and the data acquired with the scanning system described in Chapter 4. Portions of Chapters 5-8 are also described in [Curless & Levoy 1996].

Finally, in Chapter 9, we summarize the contributions of this thesis and describe some areas of future work.

Chapter 2

Optical triangulation: limitations and prior work

Active optical triangulation is one of the most common methods for acquiring range data. Although this technology has been in use for over two decades, its speed and accuracy has increased dramatically in recent years with the development of geometrically stable imaging sensors such as CCD's and lateral effect photodiodes.

Researchers and manufacturers have used optical triangulation scanning in a variety of applications. In medicine, optical triangulation has provided range data for plastic surgery simulation, offering safer, cheaper, and faster shape acquisition than conventional volumetric scanning technologies [Pieper et al. 1992]. In industry, engineers have used triangulation scanners for applications that include postal package processing [Garcia 1989] and printed circuit board inspection [Juha & Souder 1987]. Triangulation scanners also provide data to drive computer graphics applications, such as digital film-making [Duncan 1993].

Figure 2.1 shows a typical system configuration in two dimensions. The location of the center of the reflected light pulse imaged on the sensor corresponds to a line of sight that intersects the illuminant in exactly one point, yielding a depth value. The shape of the object is acquired by translating or rotating the object through the beam or by scanning the beam across the object.

In this chapter, we begin with an overview of optical triangulation configurations (Section 2.1). Next, we discuss the limitations of traditional methods in both qualitative and

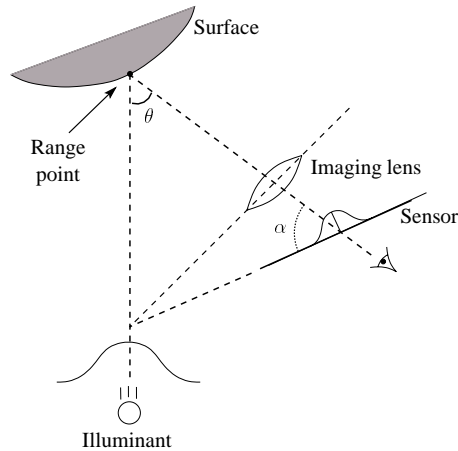


Figure 2.1: Optical triangulation geometry. The illuminant reflects off of the surface and forms an image on the sensor. The center of the illuminant maps to a unique position on the sensor based on the depth of the range point. In order for all points along the center of the laser sheet to be in focus, the angles θ and α are related to one another by Equation 2.1.

a quantitative contexts (Section 2.2). Finally, we describe previous efforts to evaluate and correct for the errors inherent in traditional triangulation methods (Section 2.3).

2.1 Triangulation Configurations

The range acquisition literature contains many descriptions of optical triangulation range scanners, of which we list a handful [Rioux et al. 1987] [Hausler & Heckel 1988] [Mundy & Porter 1987]. Several survey articles have also appeared [Jarvis 1983] [Strand 1983], including Besl's excellent survey [Besl 1989] which describes numerous optical range imaging methods and estimates relative performances. The variety of optical triangulation configurations differ primarily in the structure of the illuminant (typically point, stripe, multi-point, or multi-stripe), the dimensionality of the sensor (linear array or CCD grid), and the scanning method (move the object or move the scanner hardware).

2.1.1 Structure of the illuminant

The structure of the illuminant can take a variety of forms. A beam of light forms a spot on a surface and provides a single range value. By passing the beam through a cylindrical

lens, a light stripe can be projected onto an object to collect a range profile (Figure 1.2b). Researchers have also tried projecting multiple spots or multiple stripes onto an object for more parallelized shape acquisition, though multiple steps are usually required to disambiguate the light reflections. When imaging the reflected light onto a sensor with lenses, the single point and stripe illuminants offer the advantage that, at any instant, all intersections of the light with the object must lie in a plane. Since lenses image points in a plane to points in another plane, the sensor can be oriented to keep the beam or sheet of light in focus, thus reducing depth of field problems. When the focal plane is tilted, the image plane must also be tilted so as to satisfy the Scheimpflug condition [Slevogt 1974]:

$$\tan \alpha = M \tan \theta \quad (2.1)$$

where θ and α are the tilt angles of the focal and image planes, respectively, as shown in Figure 2.1, and M is the magnification on the optical axis. The resulting triangulation geometry has the property that the focal, image, and lens planes all intersect in a single line. Note that multi-point and multi-stripe systems generally cannot take advantage of this optimal configuration, because the illumination usually does not lie in a plane.

2.1.2 Type of illuminant

The type of illuminant can be either coherent or incoherent. Coherent illuminants such as lasers offer several distinct advantages over their incoherent counterparts. First, lasers can be held in tight focus over a long range. Second, since laser light is tuned to a single wavelength, the sensor can be coated with a bandpass wavelength filter, decreasing sensitivity to ambient light. In addition, the optics do not have to be corrected for chromatic aberrations, and elements such as prisms can be used with ease. Lasers used in triangulation also do not typically have problems with heat dissipation, whereas incoherent illuminants of sufficient power frequently do. The disadvantages of using lasers are laser speckle (random coherent interference due to surface roughness) and the need for special safety precautions among lasers operating at visible and ultraviolet wavelengths. We will discuss the impact of laser speckle on range accuracy in Sections 2.2.4 and 3.4.

2.1.3 Sensor

Sensors for optical triangulation systems also come in a variety of forms. For narrow beam illumination, point (zero-dimensional) sensors such as photodiodes or line (one-dimensional) sensors such as lateral effect photodiodes and linear array CCD's are sufficient, though point sensors must be scanned to provide another dimension. For light stripe, multi-point, and multi-stripe systems, a two-dimensional sensor is necessary and typically comes in the form of a CCD array, though point and line sensors can also be scanned to provide the required dimensions.

2.1.4 Scanning method

The method of scanning an object is also a matter of choice. During a single range imaging sweep, the illumination-sensor system can be stationary while a platform translates and rotates the object through the field of view, or the object may be stationary while the scanner moves. Alternatively, both the object and the scanning equipment may be stationary while rotating mirrors sweep the illuminant and sensor viewing directions across the object. For this latter scanning approach, the sensor viewpoint must sweep in synchrony with the illuminant to ensure that the sensor tracks the moving illuminant and keeps it in focus (see, for example, [Rioux et al. 1987]). In addition, an optical triangulation scanner can collect range data in continuous sweeps such that consecutive range points are adjacent in space (barring surface discontinuities). Alternatively, the scanning may proceed in spatially disjoint steps where the object moves an arbitrary amount relative to the scanner between acquisitions. In Chapters 3 - 4, we will be concerned with scanners which perform continuous sweeps or which move in small steps relative to the object, because these types of motion permit correction of systematic artifacts.

2.2 Limitations of traditional methods

For optical triangulation systems, the accuracy of the range data depends on proper interpretation of imaged light reflections. The most common approach is to reduce the problem to one of finding the "center" of a one dimensional pulse, where the "center" refers to the

position on the sensor which hopefully maps to the center of the illuminant. Typically, researchers have opted for a statistic such as mean, median or peak of the imaged light as representative of the center. Each of these statistics gives the correct answer when the surface is perfectly planar. In this case, the sensor records a compressed or expanded image of the illuminant's shape, depending on the orientation of the surface with respect to the illuminant and sensor. The location of the center of the imaged pulse is not altered under these circumstances.

2.2.1 Geometric intuition

The general accuracy of these statistics breaks down, however, whenever the surface perturbs the shape of the illuminant. Perturbations of the shape of the imaged illuminant occur whenever:

- The surface reflectance varies.
- The surface geometry deviates from planarity.
- The light paths to the sensor are partially occluded.
- The light is coherent, and the surface is sufficiently rough to introduce laser speckle.

In Figures 2.2-2.4, we give examples of how the first three circumstances result in range errors even for an ideal triangulation system with infinite sensor resolution and perfect calibration. For purposes of illustration, we omit the imaging optics of Figure 2.1 and treat the sensor as one-dimensional and orthographic. Further, we assume an illuminant of Gaussian cross-section, and we use the mean for determining the center of an imaged pulse. Figure 2.2 shows how a step reflectance discontinuity results in range points that do not lie on the surface. A comparison of Figures 2.2a and 2.2b shows that the range error worsens with larger reflectance steps. Figure 2.3 provides two examples of shape variations resulting in range errors. Note that in Figure 2.3b, the center of the illuminant is not even striking a surface. In this case, a measure of the center of the pulse results in a range value, when in fact the correct answer is to return no range value whatever. Finally, Figure 2.4 shows the effect of

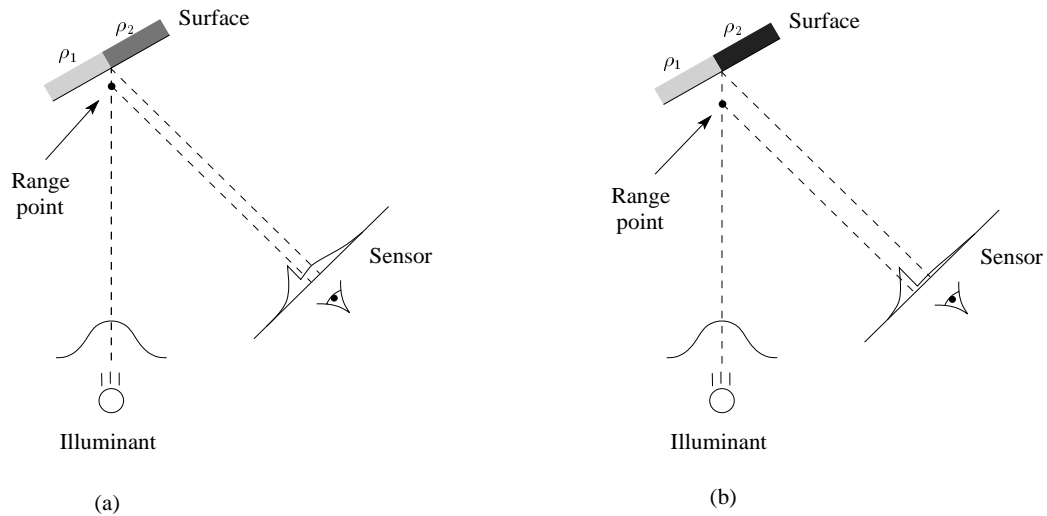


Figure 2.2: Range errors due to reflectance discontinuities. (a) The change in reflectance from light gray to dark gray distorts the image of the illuminant, perturbing the mean and resulting in an erroneous range point. (b) Same as (a), but the reflectance step is larger, causing a larger range error.

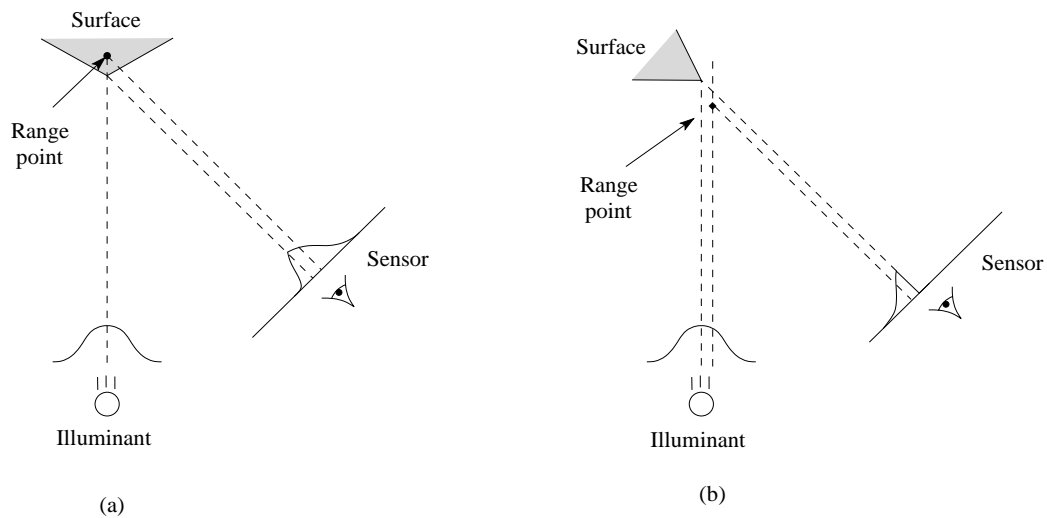


Figure 2.3: Range errors due to shape variations. (a) When reflecting off of the surfaces at the corner shown, the left half of the Gaussian is much more compressed than the right half. The result is a shift in the mean and an erroneous range point. (b) When the illuminant falls off the edge of an object, the sensor images *some* light reflection. In this case, a range point is found where there is no surface at all along the center of the illuminant.

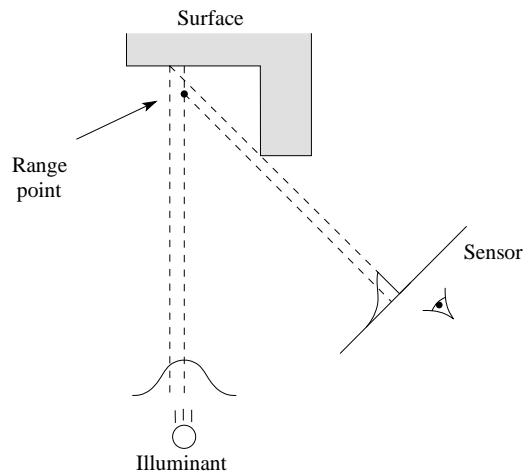


Figure 2.4: Range error due to sensor occlusion. A portion of the light reflecting from the object is blocked before reaching the sensor. The mean yields an erroneous range point, even when the center of the illuminant is not visible.

occluding the line of sight between the illuminated surface and the sensor. This range error is very similar to the error encountered in Figure 2.3b.

The fourth source of range error is laser speckle, which arises when coherent laser illumination bounces off of a surface that is rough compared to a wavelength [Goodman 1984]. The surface roughness introduces random variations in optical path lengths, causing a random interference pattern throughout space and at the sensor. Figure 2.5 shows a photograph of laser speckle arising from a rough surface¹. For triangulation systems, the result is an imaged pulse with a noise component that affects the mean pulse detection, causing range errors even from a planar target (see Figure 2.6).

¹Although optically smooth surfaces (i.e., mirrors) do not introduce laser speckle, they are also extremely hard to measure. Mirrored surfaces only reflect light to the sensor when the surface is properly oriented. Further, mirrored surfaces generally result in interreflections that significantly complicate range analysis. As a result, diffusely reflecting surfaces are desirable for range scanning. Diffuseness arises from surface roughness, which in turn leads to laser speckle.

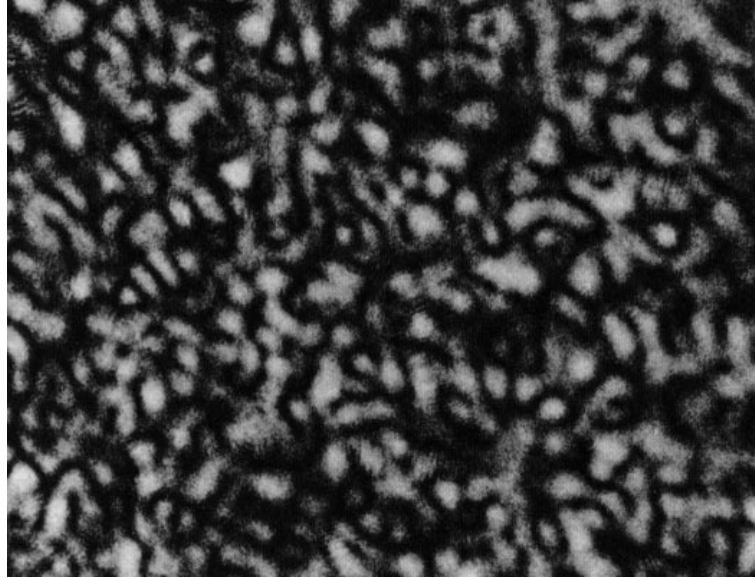


Figure 2.5: Image of a rough object formed with coherent light. Source: [Goodman 1984].

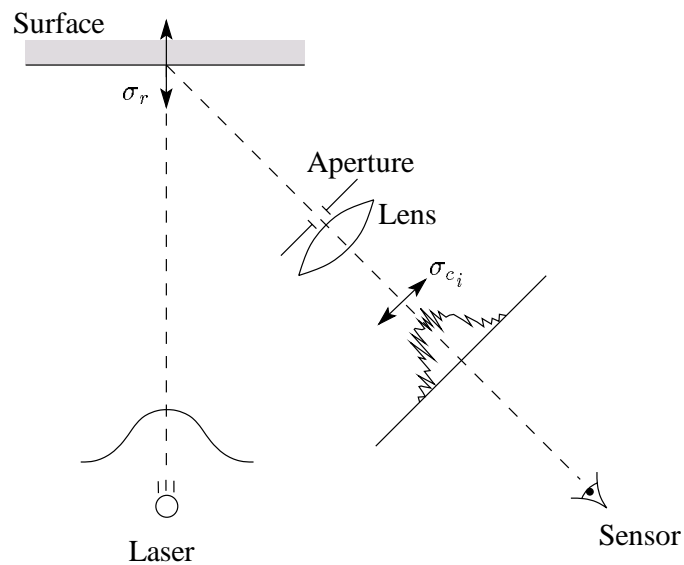


Figure 2.6: Influence of laser speckle on traditional triangulation. The image of the Gaussian is noisy, causing a random shift in the position of the mean, c_i . The uncertainty in the mean's position, σ_{c_i} maps to an uncertainty in the observed range, σ_r . Note that the direction of range uncertainty follows the center of the laser beam.

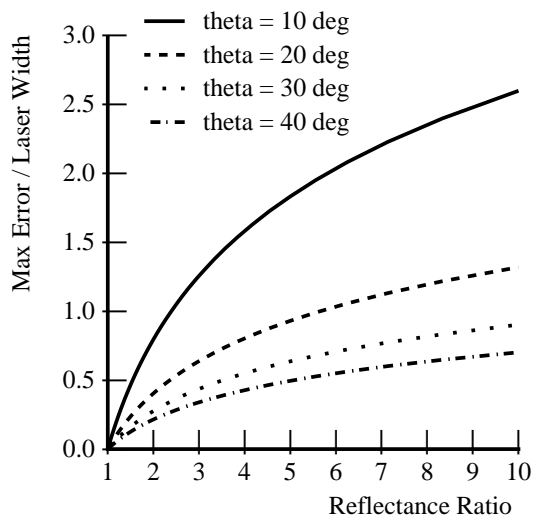


Figure 2.7: Plot of errors due to reflectance discontinuities. As the size of the reflectance step (represented as the ratio of reflectances on either side of the step), the deviation from planarity increases accordingly. Smaller triangulation angles (theta) exhibit greater errors.

2.2.2 Quantifying the error

To quantify the errors inherent in using traditional mean analysis, we numerically computed the errors introduced by reflectance and shape variations for an ideal triangulation system with a single Gaussian illuminant. We define the normally incident irradiance profile of the Gaussian illuminant as:

$$E_L(x) = I_L \exp \left[\frac{-2x^2}{w^2} \right] \quad (2.2)$$

where I_L is the power of the beam at its center, and w is a measure of beam width, taken to be the distance between the beam center and the e^{-2} point. This measure of beam width is common in the optics literature. We present the range errors in a scale invariant form by dividing all distances by the beam width. Figure 2.7 illustrates the maximum deviation from planarity introduced by scanning a reflectance discontinuity of varying step magnitudes for four different triangulation angles. As the size of the step increases, the error increases correspondingly. In addition, smaller triangulation angles, which are desirable for reducing the likelihood of missing data due to sensor occlusions, actually result in larger range errors.

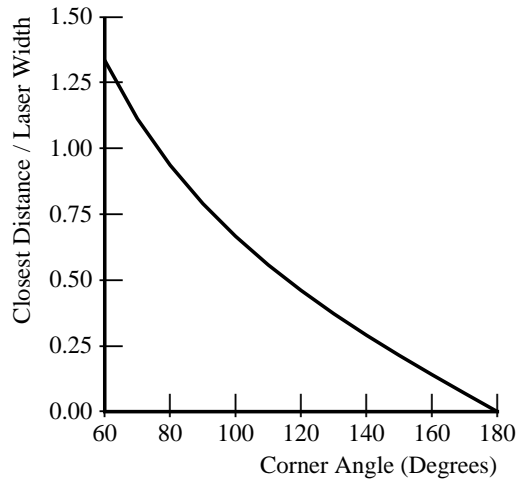


Figure 2.8: Plot of errors due to corners. The y-axis indicates the closest distance between the range data and the actual corner, while the x-axis measures the angle of the corner. Tighter corners result in greater range errors.

This result is not surprising, as sensor mean positions are converted to depths through a division by $\sin \theta$, where θ is the triangulation angle, so that errors in mean detection translate to larger range errors for smaller triangulation angles.

Figure 2.8 shows the effects of a corner on range error, where the error is taken to be the shortest distance between the computed range data and the exact corner point. The corner is oriented so that the illumination direction bisects the corner's angle as shown in Figure 2.3a. As we might expect, a sharper corner results in greater compression of the left side of the imaged Gaussian relative to the right side, pushing the mean further to the right on the sensor and pushing the triangulated point further behind the corner. In this case, the triangulation angle has little effect as the greater mean error to depth error amplification is offset almost exactly by the smaller observed left/right pulse compression imbalance.

We can estimate what the absolute values of these errors are for a typical triangulation system. For example, the triangulation angle of our scanner hardware is 30° , and the laser width is about 1 mm across a depth of 0.3 m. For this configuration, we would expect errors of 0.8 mm for a 10:1 reflectance step and 0.5 mm for a corner angle of 110° .

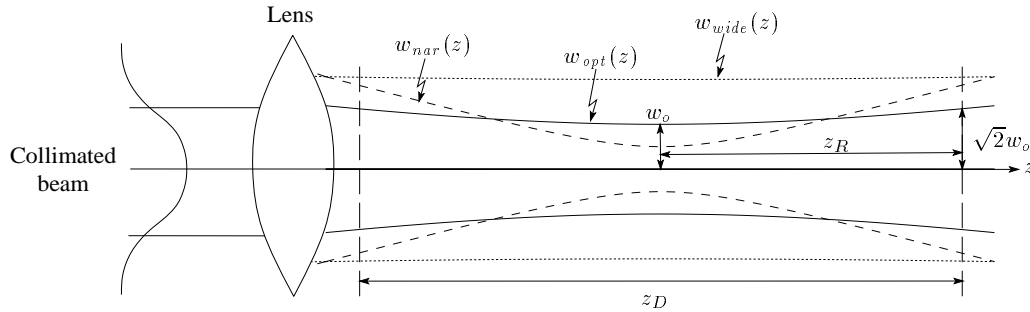


Figure 2.9: Gaussian beam optics. A collimated beam is focused by the lens to a width, w_o , and spans a desired depth of field z_D . Bringing the beam into tight focus results in a rapidly expanding beam ($w_{nar}(z)$). A wide beam expands slowly ($w_{wide}(z)$), but may be too wide over the desired depth of field. The optimal beam ($w_{opt}(z)$) expands only by a factor of $\sqrt{2}$ over the depth of field. For this optimal configuration, the distance between the beam waist and the $\sqrt{2}$ point is called the Rayleigh range, z_R .

2.2.3 Focusing the beam

One possible strategy for reducing the errors described in the previous section is to narrow the illuminating beam. Unfortunately, there are practical limitations to implementing this strategy. First, in order to take advantage of the smaller beam width, the sensor resolution must increase. This leads to expensive sensors. Second, using lenses to focus a Gaussian beam arbitrarily over the field of view is not possible due to diffraction limits. The best candidate for a tightly focused illuminant over a large depth of field is a laser beam. The irradiance profile of a laser beam is typically Gaussian as described by Equation 2.2, and the width of the beam expands from its narrowest point as [Siegman 1986]:

$$w(z) = w_o \sqrt{1 + \left(\frac{\lambda z}{\pi w_o^2} \right)^2}$$

where w_o is the beam waist or width of the beam at its narrowest point, z is the distance from this point, and λ is the wavelength of the laser. Figure 2.9 shows how the beam expands for various beam waists. Note that as the waist becomes narrower, the beam expands faster. For a given depth of field, z_D , we want the beam to be as tight as possible to limit the effects of triangulation errors. If the waist is too narrow, then the beam expands too rapidly and becomes too large at the edges of the field of view. If the waist is too large, it expands slowly,

but is still too large at the edges of the field of view. The optimum beam width is attained when the waist obeys the relation:

$$w_o = \sqrt{\frac{\lambda z_D}{2\pi}}$$

In this case, the beam reaches a maximum width of $w = \sqrt{2}w_o$ and the value $z_R = z_D/2$ corresponds to what is known as the Rayleigh range of the beam. The variation in width is thus:

$$\sqrt{\frac{\lambda z_D}{2\pi}} \leq w \leq \sqrt{\frac{\lambda z_D}{\pi}}$$

The best width to range ratio at the edges of the field of view is:

$$\frac{w}{z_D} = \sqrt{\frac{\lambda}{\pi z_D}} \quad (2.3)$$

The discussion of range errors due to reflectance and shape variations in the previous section shows that the errors of an optical triangulation system are on the order of the width of the illuminant. Thus, the beam width to range ratio is a measure of the relative accuracy of the system. Equation 2.3 tells us that once we have selected a range of interest, diffraction limits impose a bound on the relative accuracy in the presence of reflectance and shape variations.

Note that Bickel et al. [1985] have explored the use of axicons (e.g., glass cones and other surfaces of revolution) to attain tighter focus of a Gaussian beam. The refracted beam, however, has a zeroth order Bessel function cross-section; i.e., it has numerous side-lobes of non-negligible irradiance. The influence of these side-lobes is not well-documented and would seem to complicate triangulation. In addition, once the sensor resolution is fixed, then arbitrarily narrowing the beam actually becomes undesirable. If the image of the beam spans only one or two pixels, then the computed mean will not attain sub-pixel accuracy. See Section 3.5 for a discussion of the beam width in a signal processing context.

2.2.4 Influence of laser speckle

Even under the most ideal circumstances of scanning a planar object with no reflectance variations, the accuracy of optical triangulation methods using coherent illumination are still limited by an unavoidable interference phenomenon: laser speckle. In this section, we describe how laser speckle arises and how it results in range errors.

In order to analyze the effects of laser speckle, we must consider the wave nature of light and, in particular, the effects of diffraction. One of the most powerful tools for studying these effects is scalar diffraction theory. Scalar diffraction theory treats light as a scalar field rather than as a coupled electric and magnetic field. Experiment has shown that this approximation is valid as long as (1) the diffracting aperture is large compared to a wavelength and (2) the diffracted fields are not being observed too close to the aperture. Both of these criteria are satisfied in the current context.

Throughout this section we adopt the notation of Goodman [1968]. For a monochromatic wave, the scalar field at a point in space may be written:

$$u(\mathbf{x}, t) = U(\mathbf{x}) \cos[2\pi\nu t + \phi(\mathbf{x})]$$

where $U(\mathbf{x})$ and $\phi(\mathbf{x})$ are the amplitude and phase of the wave at position \mathbf{x} , and ν is the optical frequency. It proves convenient to re-write this expression as:

$$u(\mathbf{x}, t) = \text{Re}[\mathbf{U}(\mathbf{x}) \exp(-i2\pi\nu t)]$$

where $\mathbf{U}(\mathbf{x})$ is a complex function (called a phasor):

$$\mathbf{U}(\mathbf{x}) = U(\mathbf{x}) \exp[-i\phi(\mathbf{x})]$$

and $\text{Re}[\]$ is the real part of its argument. When solving problems in scalar diffraction theory, it suffices to represent the field with $\mathbf{U}(\mathbf{x})$, because the time dependence is the same everywhere and is known a priori. Researchers sometimes refer to $\mathbf{U}(\mathbf{x})$ as the field “amplitude”, though it should be remembered that it is a complex quantity. Note that when taking physical measurements, we evaluate the intensity of a field, given by:

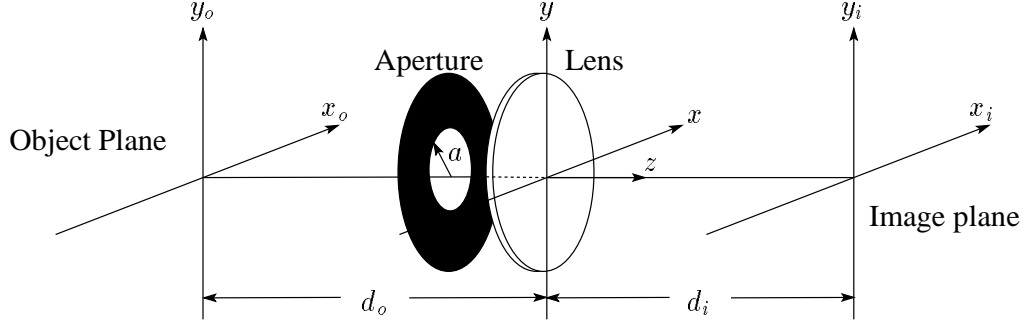


Figure 2.10: Imaging geometry and coordinate systems.

$$I(\mathbf{x}) = |\mathbf{U}(\mathbf{x})|^2 = \mathbf{U}(\mathbf{x})\mathbf{U}^*(\mathbf{x})$$

Now consider the imaging geometry shown in Figure 2.10. A striking result from scalar diffraction theory is the fact that the image formed by a lens is the same as the image described by geometrical optics, filtered by an amplitude spread function (also known as a point spread function):

$$\mathbf{U}_i(x_i, y_i) = \mathbf{U}_g(x_i, y_i) * h(x_i, y_i) \quad (2.4)$$

where \mathbf{U}_i is the resulting image field, and \mathbf{U}_g is the geometrical optics image, which is in turn given by the relation:

$$\mathbf{U}_g(x_i, y_i) = \frac{1}{M} \mathbf{U}_o \left(-\frac{x_i}{M}, -\frac{y_i}{M} \right) \quad (2.5)$$

where \mathbf{U}_o is the field in the object plane, and M is the magnification factor. The amplitude spread function is simply the Fourier transform of the lens pupil:

$$h(x_i, y_i) = \iint_{-\infty}^{\infty} P(\lambda d_i s_x, \lambda d_i s_y) \exp[-i2\pi(x_i s_x + y_i s_y)] ds_x ds_y \quad (2.6)$$

where $P(x, y)$ describes the shape of the pupil (usually a circular disc), d_i is the distance to the image, and λ is the optical wavelength. For a circular lens aperture, the pupil function is unity with a radius of a and zero outside. The amplitude spread function for such an aperture

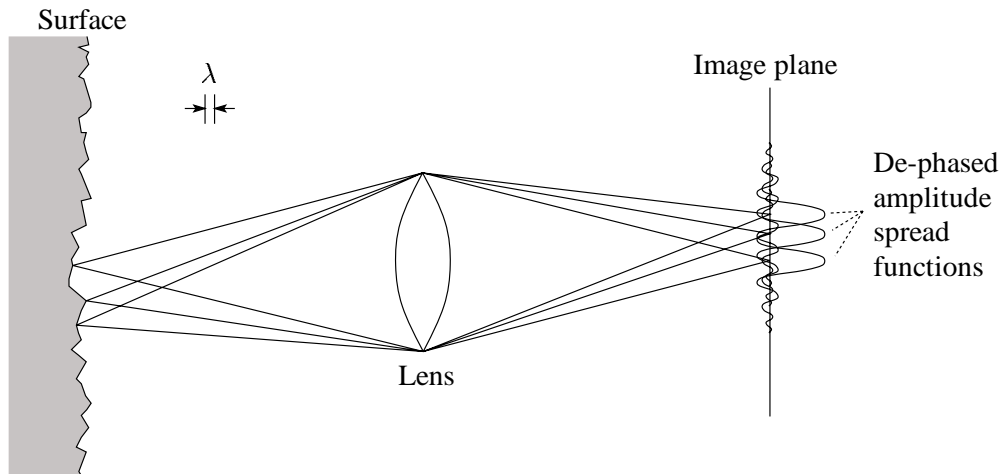


Figure 2.11: Speckle due to diffraction through a lens. The image of the surface is filtered by the amplitude spread function. Because the surface is rough compared to a wavelength, the image contains noisy phase terms that influence nearby points on the surface through the amplitude spread function. The result is laser speckle. Source: [Goodman 1984].

resembles a circularly symmetric “sinc” function², where the first zero crossing is at:

$$r \approx 0.61 \frac{\lambda d_i}{a}$$

Note that the imaging equations (2.4 - 2.6) relate object and image *fields*, not intensities. The intensities must be computed by finding the square magnitude of the fields.

Speckle arises in an image when the surface is rough compared to the optical wavelength. The result is random variations in the relative phases of imaged points. If the imaging system were to exhibit no diffraction effects (i.e., if the amplitude spread function were an impulse function), then these phases would have no impact, because they would vanish when computing the intensities. However, real imaging systems do exhibit diffraction effects, and the amplitude spread function serves to distribute the random variations across the image plane. The result is laser speckle. Figure 2.11 illustrates the this phenomenon.

In the remainder of this section, we attempt to quantify the effect of laser speckle on

² $\text{sinc}(x) \equiv \frac{\sin(\pi x)}{\pi x}$

range accuracy. To do so, we consider the case of a two-dimensional world, which permits us to remove references to the y coordinate in the equations above. This simplification will aid in the discussion of the issues of laser speckle, but will not significantly alter the basic results. Note that in this two-dimensional world, the amplitude spread function for an imaging aperture is simply the “sinc” function. In addition, we will treat the triangulation imaging geometry as though it were an axially aligned imaging geometry. This approximation introduces some error, because some of the imaged light originates from regions outside of the plane in focus (the center of the illuminant), but for narrow illuminants, this error is negligible [Francon 1979].

For a Gaussian illuminant incident on the surface of an object, the field at the surface of the object takes the form:

$$\mathbf{U}_o(x_o) = G_o(x_o) \exp[i\phi_o(x_o)] \quad (2.7)$$

where $G_o(x_o)$ is the Gaussian illuminant and $\phi_o(x_o)$ represents the random phase variations introduced by the roughness of the surface. We can now write the field at the image plane as:

$$\mathbf{U}_i(x_i) = \{G_g(x_i) \exp[i\phi_g(x_i)]\} * h(x_i)$$

where $G_g(x_i)$ and $\phi_g(x_i)$ are the images of the Gaussian and phase terms, respectively, as given by geometric optics. From this equation, we can compute the intensity measured at the image plane:

$$I_i(x_i) = \mathbf{U}_i(x_i)\mathbf{U}_i^*(x_i) \quad (2.8)$$

Equations 2.7 - 2.8 describe the physical image of a Gaussian illuminant after experiencing random phase variations and diffraction “filtering.” Errors in determining the mean of this image result in range errors in triangulation systems using traditional analysis. The mean is defined by:

$$c_i = \frac{\int_{-\infty}^{\infty} x_i I_i(x_i) dx_i}{\int_{-\infty}^{\infty} I_i(x_i) dx_i} \quad (2.9)$$

For a centered Gaussian, this mean should be exactly zero; however, the random phase variations introduce statistical variations in the mean that we can quantify as:

$$\sigma_{c_i} = [\langle c_i^2 \rangle - \langle c_i \rangle^2]^{\frac{1}{2}} = \langle c_i^2 \rangle^{\frac{1}{2}} \quad (2.10)$$

where the expected value of the mean is assumed to be zero. Figure 2.6 illustrates the influence of laser speckle in a triangulation system. The error in the mean maps to a range error through the relation:

$$\sigma_r = \frac{M \sigma_{c_i}}{\sin \theta}$$

In other words, once we have computed the variations in detecting the mean at the sensor, we must map it into a range error through multiplication by the imaging system's magnification factor, M , and division by the triangulation factor, $\sin \theta$.

Computing the standard deviation described by Equations 2.9 and 2.10 analytically has proven to be extremely difficult. Instead, we have performed numerical simulations. These simulations require some characterization of the phase function, $\phi_o(x_o)$, which describes the roughness of the surface. Researchers typically model this function to be proportional to the height profile, $\beta(x_o)$ of the surface:

$$\phi_o(x_o) = \frac{2\pi}{\lambda} \beta(x_o)$$

This $\beta(x_o)$ is typically taken to be a random process with Gaussian statistics at each point on the surface and a Gaussian autocorrelation spectrum. The pointwise statistics are thus parameterized by the surface height variance, R_q , also called the roughness, and the correlation length, α [Fujii et al. 1976]. As a result, the parameter space we must explore is four dimensional: a function of the width of the laser, the width of the point spread function, the surface roughness and the correlation length. To date, we have thoroughly studied the

deviation of the mean for surfaces rough compared to a wavelength with zero correlation length, and we have arrived at a qualitative understanding of the behavior when the surface roughness parameters are varied. For uncorrelated rough surfaces, the variation of the mean follows the relation:

$$\sigma_{c_i} \approx \frac{1}{2} \sqrt{\frac{w_i \lambda d_i}{2a}}$$

where w_i is the width of the image of the Gaussian illuminant, d_i is the distance from the lens to the aperture, and a is the aperture radius. Mapping this into a range error we obtain:

$$\sigma_r \approx \frac{M}{2 \sin \theta} \sqrt{\frac{w_i \lambda d_i}{2a}}$$

Noting that $w = Mw_i$ is the width of the illuminant in object space, and $d_o = Md_i$ is the distance to the object, the range error can be re-written as:

$$\sigma_r \approx \frac{1}{2 \sin \theta} \sqrt{\frac{w \lambda d_o}{2a}} \quad (2.11)$$

This relation yields several insights. First of all, the range error is fundamentally independent of the resolution of the sensor; it is an inescapable consequence of the speckle phenomenon. Secondly, we expect that narrowing the aperture will increase the speckle noise and thereby increase the range error. Finally, the range error varies with the square root of the width of the laser as seen from the sensor. Narrowing the laser ought to decrease range noise.

Numerical experiments with various surface roughness and correlation length parameters have yielded some quantitative results that follow qualitative expectations. In summary, as the correlation length grows, we observe a decrease in the computed range error. Similarly, as the surface roughness decreases, the range error also decreases. This result is not surprising; the limiting case of a perfectly smooth planar surface should result in no laser speckle and thus no range error. Increasing the correlation length and decreasing the roughness bring the results closer to the perfectly smooth case.

To give a sense for the size of the range errors, we can substitute some typical values into Equation 2.11. The triangulation system used for experiments in Chapter 4 has a 30

degree triangulation angle, an aperture radius of about 5 mm, a stand-off of 1 meter and uses a HeNe laser source ($\lambda = 632.8$ nm). We would therefore expect the range error due to reflections from a “perfectly” rough surface to be approximately 0.25 mm. This error corresponds to roughly half the resolution of the sensor being used. Real surfaces, however, are not perfectly rough, so we would expect smaller range errors in practice.

2.3 Prior work on triangulation error

Several researchers have observed the limitations in triangulation accuracy due to reflectance and shape variations [Buzinski et al. 1992] [Soucy et al. 1990] [Mundy & Porter 1987]. In addition, researchers have studied the effect of laser speckle on range determination and have indicated that speckle is a fundamental limit to the accuracy of laser range triangulation, as described in the previous section, though its effects can be reduced with well-known speckle reduction techniques [Baribeau & Rioux 1991] [Dorsch et al. 1994]. These speckle reduction methods, however, typically require spatial averaging, resulting in a trade-off between noise and spatial resolution. Using a less coherent light source appears to be a better alternative, as it leads to less speckle noise without loss of resolution. Regardless, changing the viewpoint generally results in a different speckle pattern, so multiple range images acquired from different viewpoints can be combined to reduce noise without loss of resolution. We demonstrate this last idea in Section 8.3.

Mundy & Porter [1987] attempt to correct for variations in surface reflectance by noting that two imaged pulses, differing in position or wavelength are sufficient to overcome the reflectance errors on a planar surface, though some restrictive assumptions are necessary for the case of differing wavelengths, and they do not address errors due to shape variations. Kanade et al. [1991] describe a rangefinder that finds peaks in time for a stationary sensor with pixels that view fixed points on an object as the illuminant sweeps across the scene. This method is very similar to the spacetime analysis presented in this thesis for solving some of the problems of optical triangulation; however, the authors in [Kanade et al. 1991] do not indicate awareness that their design addresses these problems. Further, we show that the principle generalizes to other scanning geometries.

Chapter 3

Spacetime Analysis

Many optical triangulation scanners operate by sweeping the illumination over an object while imaging the reflected light over time. The previous chapter clearly demonstrates that analyzing the imaged pulses at each time step leads to systematic range errors. In this chapter, we describe a new method for optical triangulation called *spacetime analysis*. We show that by analyzing the time evolution of the imaged pulses, this new method can reduce or eliminate range errors associated with traditional methods.

We begin with an intuitive description of how the spacetime analysis works (Section 3.1), followed by a rigorous derivation of its properties under a set of assumptions such as linear scanning and orthographic sensing (Section 3.2). We then describe how the method generalizes when weakening or removing these assumptions (Section 3.3). In Section 3.4, we consider the role of laser speckle in spacetime analysis and show that it still imposes a limit on triangulation accuracy. Finally, we put optical triangulation scanners into a signal processing context and draw conclusions about how to improve them (Section 3.5).

3.1 Geometric intuition

Figure 3.1 illustrates the principle of spacetime analysis for a laser triangulation scanner with Gaussian illuminant and orthographic sensor as it translates across the edge of an object. As the scanner steps to the right, the sensor images a smaller and smaller portion of the laser cross-section. By time t_3 , the sensor no longer images the center of the illuminant, and

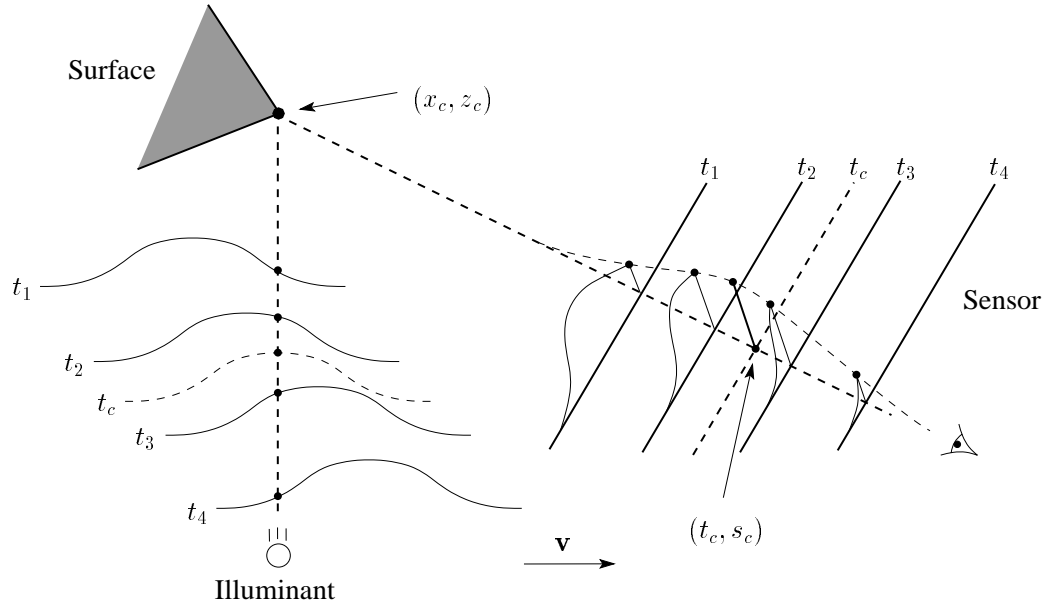


Figure 3.1: Spacetime mapping of a Gaussian illuminant. The Gaussians at left represent the profile of the illuminant at times t_1 through t_4 . The solid Gaussians at right represent the images of the illuminant at these same times. The dashed Gaussian represents the time evolution of these images for a single line of sight, corresponding to a single point on the targeted surface. Although the solid Gaussians at right may be distorted or clipped by depth discontinuities or reflectance changes in the surface, the dashed Gaussian is always the same shape (unless it is missing entirely), and it is centered at a location that corresponds exactly to a range point. These properties of the dashed Gaussian are the keys to the spacetime analysis.

conventional methods of range estimation fail. However, if we look along the lines of sight from the corner to the laser and from the corner to the sensor, we see that the profile of the laser is being imaged *over time* onto the sensor (indicated by the dotted Gaussian envelope). Thus, we can find the coordinates of the corner point (x_c, z_c) by searching for the mean of a Gaussian along a constant line of sight through the sensor images. We can express the coordinates of this mean as a time and a position on the sensor, where the time is in general between sensor frames and the position is between sensor pixels. The position on the sensor indicates a depth, and the time indicates the lateral position of the center of the illuminant. In the example of Figure 3.1, we find that the spacetime Gaussian corresponding to the exact corner has its mean at position s_c on the sensor at a time t_c between t_2 and t_3 during the scan. We establish the corner's position by triangulating the center of the illuminant at time t_c

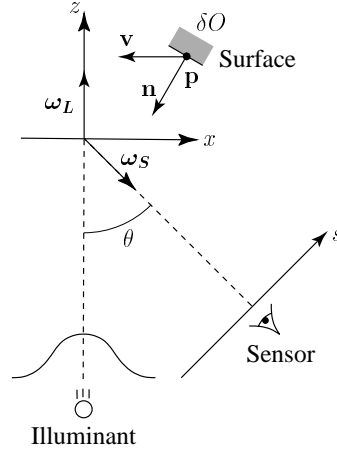


Figure 3.2: Triangulation scanner coordinate system.

with the sensor line of sight corresponding to the sensor coordinate s_c and the lateral sensor position at t_c .

3.2 A complete derivation

For a more rigorous analysis, we consider the time evolution of the irradiance from a translating differential surface element, δO , as recorded at the sensor. We refer the reader to Figure 3.2 and Table 3.1 for a description of coordinate systems and symbols. Note that in contrast to the previous section, the surface element is translating instead of the illuminant-sensor assembly. The element has a normal \mathbf{n} and an initial position \mathbf{p}_o and is translating with velocity \mathbf{v} , so that:

$$\mathbf{p}(t) = \mathbf{p}_o + t\mathbf{v}$$

Our objective is to compute the coordinates $\mathbf{p}_o = (x_o, z_o)$ given the temporal irradiance variations on the sensor. For simplicity, we assume that $\mathbf{v} = (-v, 0)$. The illuminant we consider is a laser with a unidirectional Gaussian radiance profile:

$$L_L(\mathbf{x}, \omega) = I_L \exp\left[\frac{-2x^2}{w^2}\right] \delta(\omega - \omega_L) \quad (3.1)$$

δO	Differential surface element
$\mathbf{p}(t)$	Position of surface element
\mathbf{p}_o	Position of surface element (x_o, z_o) at time $t = 0$
\mathbf{n}	Normal of surface element
\mathbf{v}	Velocity of whole object
$\boldsymbol{\omega}_L$	Direction of illuminant
$\boldsymbol{\omega}_S$	View direction

Table 3.1: Symbol definitions for spacetime analysis.

where I_L is the power of the beam at its center, w is the e^{-2} half width, and the delta function indicates the directionality of the beam. In accordance with Figure 3.2, we will assume that $\boldsymbol{\omega}_L = (0, 1)$. The differential reflected radiance from the element in the direction of the sensor is simply:

$$dL(\mathbf{p}(t), \boldsymbol{\omega}_S) = f_r(\boldsymbol{\omega}, \boldsymbol{\omega}_S) |\mathbf{n} \cdot \boldsymbol{\omega}_L| L_L(\mathbf{p}(t), \boldsymbol{\omega}) d\boldsymbol{\omega} \quad (3.2)$$

where $f_r(\boldsymbol{\omega}, \boldsymbol{\omega}_S)$ is the bidirectional reflection distribution function (BRDF) of the point \mathbf{p}_o , evaluated at the incident direction, $\boldsymbol{\omega}$, and outgoing sensor direction, $\boldsymbol{\omega}_S$. Note that we assume that the BRDF is defined in a global sense for the surface element, rather than relative to its normal. Further, we treat incoming directions as pointing toward the surface rather than away from the surface, which is consistent with the description of the radiance field in terms of position and direction.

Substituting Equation 3.1 into Equation 3.2 and integrating over all incident directions, we find the total radiance reflected from the element to the sensor to be:

$$L(\mathbf{p}(t), \boldsymbol{\omega}_S) = f_r(\boldsymbol{\omega}_L, \boldsymbol{\omega}_S) |\mathbf{n} \cdot \boldsymbol{\omega}_L| I_L \exp \left[\frac{-2(x_o - vt)^2}{w^2} \right] \quad (3.3)$$

Projecting the point $\mathbf{p}(t)$ onto the sensor, we find:

$$s = (x_o - vt) \cos \theta - z_o \sin \theta \quad (3.4)$$

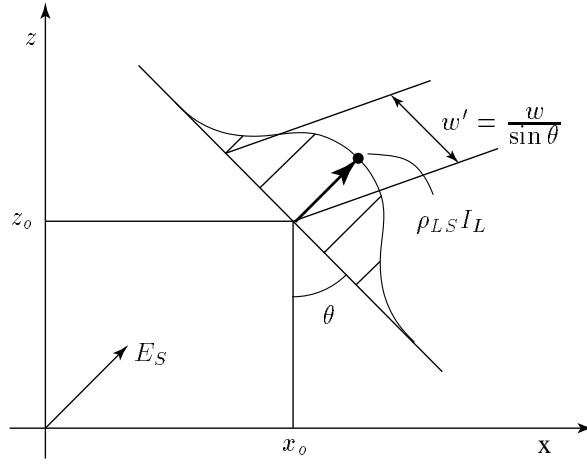


Figure 3.3: Spacetime image of the Gaussian illuminant. After scaling the sensor scanlines to map to depth and lateral displacement, we see that a point is imaged to a tilted Gaussian in the spacetime image. The center of the Gaussian maps to the coordinates of the point, the amplitude depends on the reflectance coefficient and beam strength, and the width is fixed by the scanner geometry.

where s is the position on the sensor and θ is the angle between the sensor and laser directions. We combine Equations 3.3-3.4 to give us an equation for the irradiance observed at the sensor as a function of time and position on the sensor:

$$E_S(t, s) = f_r(\omega_L, \omega_S) |\mathbf{n} \cdot \omega_L| I_L \exp \left[\frac{-2(x_o - vt)^2}{w^2} \right] \delta(s - (x_o - vt) \cos \theta - z_o \sin \theta)$$

To simplify this expression, we condense the light reflection terms into one measure:

$$\rho_{LS} = f_r(\omega_L, \omega_S) |\mathbf{n} \cdot \omega_L|$$

which we will refer to as the reflectance coefficient of point \mathbf{p} . We also note that $x = vt$ is a measure of the relative x -displacement of the point during a scan, and $z = s / \sin \theta$ is the relation between sensor coordinates and depth values along the center of the illuminant. Making these substitutions we have:

$$E_S(x, z) = \rho_{LS} I_L \exp \left[\frac{-2(x - x_o)^2}{w^2} \right] \delta((x - x_o) \cos \theta + (z - z_o) \sin \theta) \quad (3.5)$$

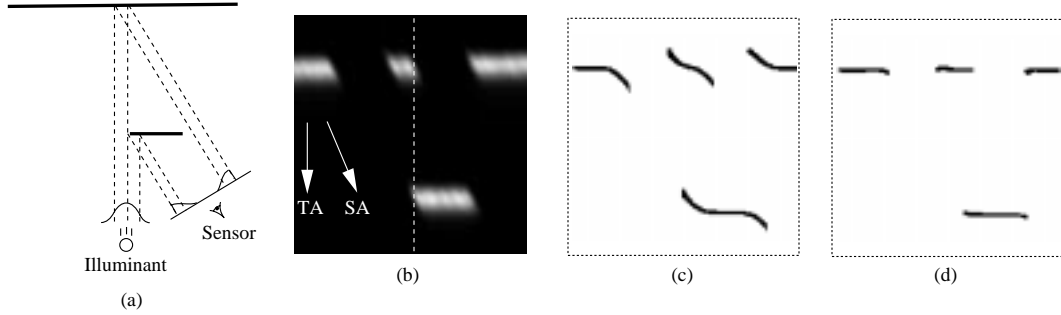


Figure 3.4: From geometry to spacetime image to range data. (a) The original geometry. (b) The resulting spacetime image. TA indicates the direction of traditional analysis, while SA is the direction of the spacetime analysis. The dotted line corresponds to the scanline generated at the instant shown in (a). (c) Range data after traditional mean analysis. (d) Range data after spacetime analysis.

This equation describes a Gaussian running along a *tilted line* through the spacetime sensor plane or *spacetime image* as depicted in Figure 3.3. We define the spacetime image to be the image whose columns are filled with sensor scanlines that evolve over time. Through the substitutions above, position within a column of this image represents displacement in depth, and position within a row represents time or displacement in lateral position. From Figure 3.3, we see that the tilt angle is θ with respect to the z -axis, and the width of the Gaussian along the line is:

$$w' = \frac{w}{\sin \theta}$$

The peak value of the Gaussian is $\rho_{LS} I_L$, and its mean along the line is located at (x_o, z_o) , the exact location of the range point. Note that the angle of the line and the width of the Gaussian are solely determined by the fixed parameters of the scanner, *not* the position, orientation, or BRDF of the surface element. Thus, extraction of range points should proceed by computing low order statistics along tilted lines through the spacetime image, rather than along columns (scanlines) as in the conventional method. Figure 3.4 illustrates this distinction. Further, we establish the position of the surface element independent of the orientation and BRDF of the element and, assuming no interreflections, independent of any other nearby surface elements. The decoupling of range determination from local shape and reflectance is *complete*. As a side effect, the peak of the Gaussian yields the irradiance at the

sensor due to the point. Thus, we automatically obtain an intensity image precisely registered to the range image, information which can assist in a task such as object segmentation.

3.3 Generalizing the geometry

We can easily generalize the previous results to other scanner geometries under the following conditions:

- The illumination direction is constant over the path of each range point.
- The sensor is orthographic.
- The motion is purely translational.
- The illumination and sensing directions are different.
- The illumination and translation directions are different

The first three conditions ensure that the reflectance coefficient, $\rho_{LS} = f_r(\omega_L, \omega_S) |\mathbf{n} \cdot \omega_L|$, is constant, the fourth condition guarantees that actual triangulation can occur, and the fifth condition ensures that the illumination is scanning *across* points in the scene. Note that the illumination need only be directional; coherent or incoherent light of any pattern is acceptable, though a narrow pattern will avoid potential depth of field problems for the sensor optics. In addition, the translational motion need not be of constant speed, only constant direction. We can correct for known variations in speed by applying a suitable warp to the spacetime image.

We can weaken the need for orthography if we assume that the BRDF does not vary appreciably over the sensor's viewing directions. The range of viewing directions depends on the focal length of the lens system and the range of positions a single point can occupy while being illuminated during a scan, which in turn depends on the width of the illuminant. In the general perspective case, the spacetime analysis proceeds along curves rather than straight lines. If the image of a point traverses a small displacement on the sensor relative to the

focal length, then assumption of local orthography is reasonable. In addition, general perspective can lead to changes in occlusion relationships during a scan that cause an illuminated point to be visible for a finite time and then become invisible while still illuminated. This effect results in a partial image of the occluded point's spacetime Gaussian and will result in a range error for this point. These points will be easy to identify: they will be near step discontinuities in the resulting range image. When acquiring multiple range images, these points can be eliminated in favor of unoccluded acquisitions of the same portions of the surface. Thus, while perspective sensors can create some complications in applying the spacetime analysis, typical lens configurations will yield reasonable results.

We can also weaken the requirement for pure translation, as long as the rotational component of motion represents a small change in direction with respect to the $f_r(\omega_L, \omega_S)|\mathbf{n} \cdot \omega_L|$ product. This constraint is reasonable for motion trajectories with large radii of curvature relative to the beam width. As in the perspective case, the spacetime analysis proceeds in general along curves, and changes in occlusion relationships can lead to erroneous range data. Nonetheless, for moderate rotational trajectories, the spacetime analysis will lead to improved range data.

3.4 Influence of laser speckle

In the previous chapter, we developed the equations that are needed to analyze the influence of laser speckle on range determination. The results of statistical analysis show that laser speckle places a limit on the attainable accuracy when using traditional triangulation. Does spacetime analysis eliminate this limitation? One encouraging observation is the fact that the imaging equation (2.4) is space-invariant, so that moving the object field corresponds to moving the image field. In this way, speckle behaves as though it adheres to the surface, much like a noisy reflectance variation. This observation would seem to indicate that the spacetime analysis would correct for speckle noise. However, when we move the object with respect to a non-uniform illuminant (such as a laser beam with Gaussian cross-section), then the object field is *not* simply translating. As a result, the speckle does not completely adhere to the surface, and spacetime analysis faces the same limitation as traditional triangulation: laser speckle imposes a fundamental limit on accuracy. In this section, we will develop some of the equations necessary to demonstrate this result.

For the spacetime analysis, we must consider a moving surface and follow a single point on the surface to observe the image of the Gaussian mapped over time. Conversely, we can consider a moving illuminant, and follow a single line of sight from a stationary sensor. These two cases are equivalent as far as the resulting speckle patterns are concerned, but the latter yields a simpler analysis.

We can describe the field at the surface of the object in terms of the moving illuminant:

$$\mathbf{U}_o(x_o, t) = G_o(x_o - v_o t) \exp[i\phi_o(x_o)]$$

where the Gaussian is moving with velocity v_o . Mapping this to the image plane:

$$\mathbf{U}_i(x_i, t) = \{G_g(x_i - v_i t) \exp[i\phi_g(x_i)]\} * h(x_i)$$

where G_g and ϕ_g are the images of the Gaussian and phase functions given by geometric optics, and v_i is the velocity of the imaged Gaussian. To simplify this relation, we can first expand the convolution:

$$\mathbf{U}_i(x_i, t) = \int_{-\infty}^{\infty} G_g(x_i - v_i t - \alpha) \exp[i\phi_g(x_i - \alpha)] h(\alpha) d\alpha$$

Next, we consider a single line of sight, $x_i = 0$, so that:

$$\mathbf{U}_i(0, t) = \int_{-\infty}^{\infty} G_g(-v_i t - \alpha) \exp[i\phi_g(-\alpha)] h(\alpha) d\alpha$$

For a symmetric amplitude spread function, and after some straightforward manipulations, this relation becomes:

$$\mathbf{U}_i(0, t) = G_g(\eta) * \{\exp[i\phi_g(\eta)] h(\eta)\} \Big|_{\eta=v_i t} \quad (3.6)$$

As described in the previous chapter, the intensity is the square magnitude of the field, but in this case, the mean we seek is with respect to *time*:

$$c_t = \frac{\int_{-\infty}^{\infty} t I_i(0, t) dt}{\int_{-\infty}^{\infty} I_i(0, t) dt} \quad (3.7)$$

The error can be solved as the variance of the mean as described in the previous chapter:

$$\sigma_{c_t} = [\langle c_t^2 \rangle - \langle c_t \rangle^2]^{\frac{1}{2}} = \langle c_t^2 \rangle^{\frac{1}{2}} \quad (3.8)$$

Figure 3.5 illustrates the influence of laser speckle when using spacetime triangulation. For traditional analysis, the uncertainty in the position of the mean on a sensor scanline corresponds directly to a depth error along the center of the illuminant. For spacetime triangulation, the error in the mean maps to an error in determining *when* the laser sheet's center intersects a line of sight at a range point. The range error is distributed along the sensor's line of sight, and obeys the relation:

$$\sigma_r = \frac{v_o \sigma_{c_t}}{\sin \theta} \quad (3.9)$$

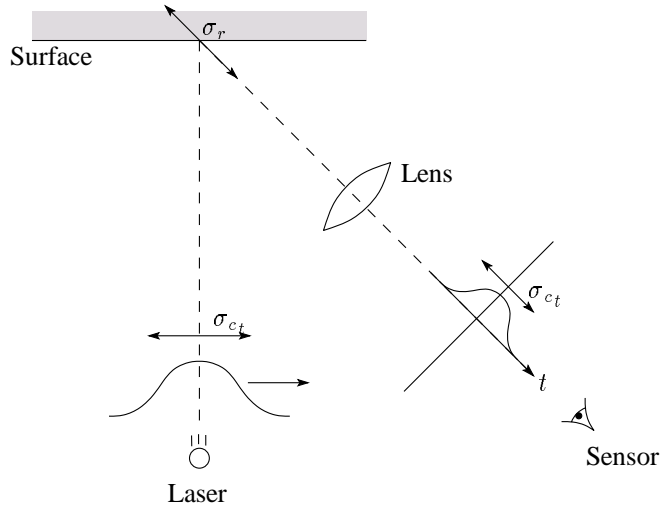


Figure 3.5: Influence of laser speckle on spacetime triangulation. When performing the spacetime analysis, the line of sight to the point is fixed, but the time at which the center of the laser passes over the range point varies with range. Laser speckle introduces uncertainty, σ_{ct} as to when the laser is centered over the range point. The effect is range uncertainty, σ_r , along the line of sight from the sensor.

As in the case for traditional analysis, computing an analytical solution using Equations 3.6-3.9 has proven to be extremely difficult. Instead, we have performed numerical simulations that lead us to the same result as we found for traditional analysis (Equation 2.11):

$$\sigma_r \approx \frac{1}{2 \sin \theta} \sqrt{\frac{w \lambda d_o}{2a}} \quad (3.10)$$

Thus, the error in spacetime triangulation under coherent illumination is independent of sensor resolution and increases with the narrowing of the aperture and the widening of the laser sheet. In addition, numerical analysis reveals that, just as in the case for traditional triangulation, smoother surfaces lead to reductions in range error.

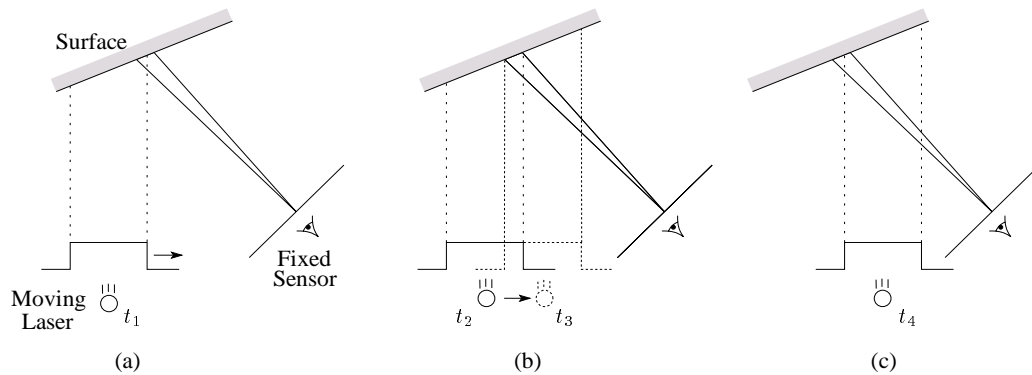


Figure 3.6: Speckle contributions at the sensor due to a moving coherent illuminant with square cross-section. The sensor and surface are stationary while the illuminant sweeps across the surface. A single pixel maps to a single point on the surface, but a neighborhood of points on the surface influence the pixel intensity as a result of diffraction at the aperture. This neighborhood is indicated by the region between the lines drawn from the sensor to the surface. (a) As the illumination translates to the right (shown here at time t_1), only part of the neighboring points, mostly to the left of the range point, are illuminated. Only these points will contribute to the observed, speckle-corrupted intensity at the sensor. (b) At time t_2 , the illumination uniformly covers the neighborhood and continues to do so until time t_3 . During this time, the pixel intensity will not vary as the illumination moves. (c) As the left edge of the illumination crosses into the neighborhood near the range point (shown here at time t_4), then only the the points mostly to the *right* of the range point will affect the pixel intensity. Thus, we expect the speckle noise in (a) and (c) to be uncorrelated.

The impact of laser speckle on *traditional* triangulation is not surprising, given the obvious corruption of the imaged illuminant. The effect of speckle on *spacetime* triangulation, however, is harder to visualize. To gain a more intuitive grasp, consider the example in Figure 3.6, which illustrates the didactic example of a stationary object and sensor and a moving illuminant with square irradiance profile. A single pixel on the sensor maps to a single point on the surface, but due to diffraction at the aperture, neighboring points on the surface influence the intensity measured at this pixel. When the sensor approaches the range point from the left, then surface points to the left of the range point affect the pixel intensity. When the illumination is completely covering the neighborhood of the range point, then translations of the illuminant do not affect the measured intensity. As the illumination passes the range point to the right, the surface points to the *right* of the range point affect the pixel intensity. Thus, when the illuminant is mostly to the left or right of the range point, the pixel intensity is determined by *different* points on the surface.

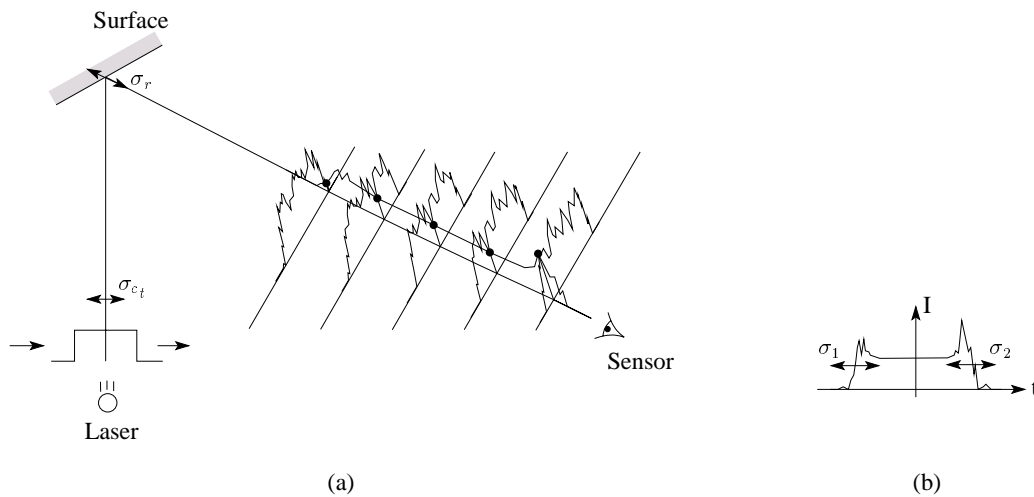


Figure 3.7: Spacetime speckle error for a coherent illuminant with square cross-section. (a) As the sensor and illuminant sweep over the surface, the sensor images noisy square waves. For regions near the center of the square wave, the speckle behaves as though it adheres to the surface as the scanning progresses. Near the edges, however, the speckle influence reveals itself. For the range point being tracked, the amplitude in the first image depends on the properties of the left portion of the surface, while the amplitude in the last image depends on the right portion of the surface. In (b) we see the resulting spacetime image of the range point. The central regions of the pulse are very flat, unlike the individual images of the square pulse at each time step in (a). However, the speckle influences the edges of the pulse, resulting in uncertainty about the mean of the pulse.

Figure 3.7 illustrates how this distinction leads to errors in spacetime triangulation, this time including the motion of the sensor along with the illuminant. As the center of the square illuminant moves over the object, the speckled image of the surface does indeed move with the surface, because the illuminant is fairly constant near the center. This explains why the spacetime pulse is very flat in the center (Figure 3.7b). However, near the edges of the pulse, the illumination is not at all constant, and speckle noise appears. The result is an uncertainty in determining the location of these edges. The noise at the edges has different properties for the left edge versus the right edge as described above, meaning that the uncertainty in determining the position of the two edges is fairly uncorrelated. Since resolving the edges is the only way of determining the center of the spacetime pulse, spacetime triangulation is limited in accuracy by laser speckle.

3.5 A Signal Processing Perspective

With insights provided by the previous section, we can now study optical range triangulation in a signal processing context. This signal processing point of view aids in visualizing how the ideal spacetime image is formed and how it is modified during acquisition and reconstruction. Further, analysis of the Fourier spectrum of the spacetime image leads to insights about how we might improve range extraction.

3.5.1 Ideal triangulation impulse response

In examining the response of a scanner to a differential element in Section 3.2, we have discovered the impulse response of a translating triangulation scanner with Gaussian illuminant and orthographic sensor. The key is to re-write Equation 3.5, as a convolution:

$$E_S(x, z) = f(x, z) * h_{ST}(x, z) \quad (3.11)$$

where h_{ST} is the spacetime impulse response,

$$h_{ST}(x, z) = I_L \exp \left[\frac{-2x^2}{w^2} \right] \delta(z \sin \theta - x \cos \theta) \quad (3.12)$$

and $f(x, z)$ is a point in space,

$$f(x, z) = \rho_{LS}(x_o) \delta(x - x_o) \delta(z - z_o) \quad (3.13)$$

In general, $f(x, z)$ describes the piecewise continuous set of points on the surface of the object that are visible to both the laser and the CCD. This set of points can be represented as a function, $z = r(x)$, with corresponding reflectance variations $\rho_{LS} = \rho_{LS}(x)$, so that we arrive at:

$$f(x, z) = \rho_{LS}(x) \delta(z - r(x)) \quad (3.14)$$

Figure 3.8 illustrates how the spacetime image is derived from a two dimensional scene.

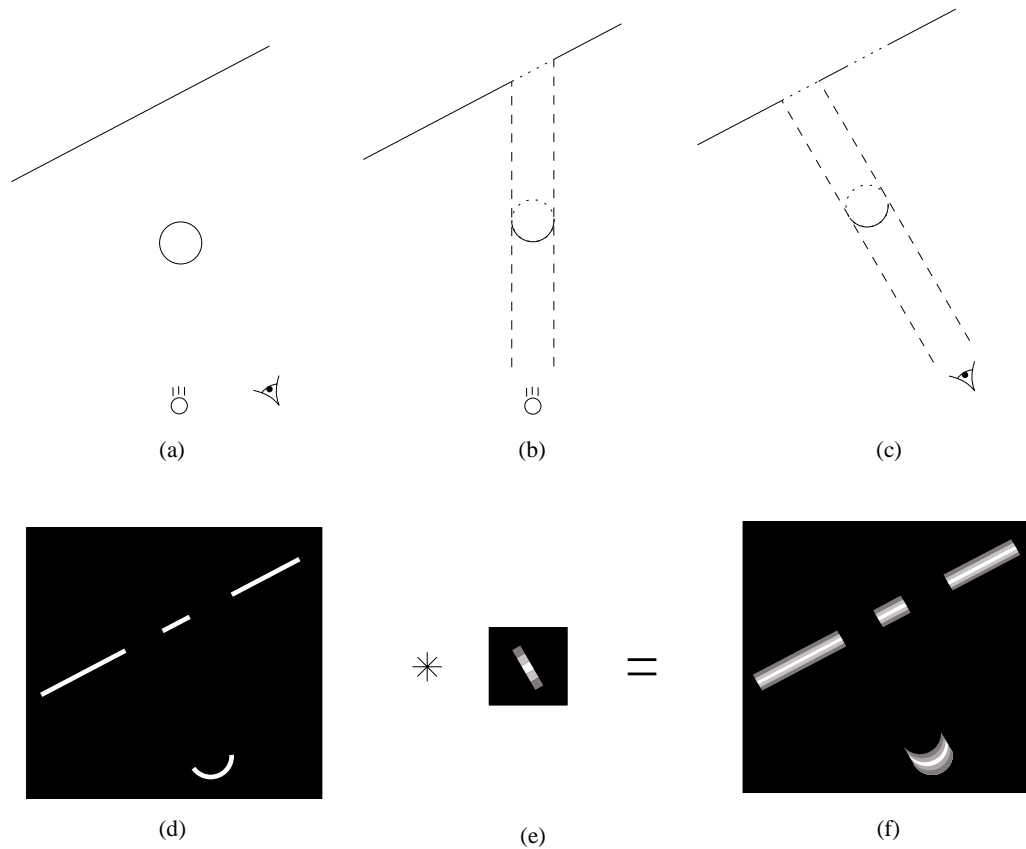


Figure 3.8: Formation of the spacetime image. The scene in (a) is being scanned horizontally. First we determine the portions of the surface visible to the laser (b) and to the sensor (c). The laser and sensor lines of sight that clip the surface are shown dashed, while the removed portions of the surface are shown dotted. The resulting surface (d) is convolved with the spacetime Gaussian (e) to create the spacetime image (f). For the purposes of this illustration, the contribution of $\rho_{LS}(x)$ has been omitted. The result of $\rho_{LS}(x)$ would be to modulate the amplitude of the spacetime Gaussian as it is being convolved across the surface.

3.5.2 Filtering, noise, sampling, and reconstruction

The function $E_S(x, z)$ represents the ideal spacetime image, and if we could acquire it perfectly, then we would be able to compute the *exact* shape of the object. In the real world, however, this image is filtered, corrupted by noise, sampled, and ultimately reconstructed before being analyzed for shape extraction.

The filtering can be decomposed into two components: spatial and temporal. Spatial blurring occurs at the sensor due to the imaging optics and the fact that each sensor cell has a finite area over which it gathers photons and accumulates a charge. We call this filter $h_{pix}(z)$, because it spans sensor pixels. The other filtering component operates temporally; as the object moves relative to the scanner, the sensor captures photons over a fixed interval of time before sampling the result and starting over. The motion is effectively blurred during this interval. We call this temporal filter $h_{frame}(x)$, where “frame” refers to the time interval and x is the representative of the time component (remember, $x = vt$).

Several noise sources also affect the spacetime image. As described in the previous section, coherent illumination leads to speckle noise that corrupts the spacetime Gaussian. In addition, the sensor will have some inherent noisiness caused by a variety of factors (see, e.g., [Janesick et al. 1987]). Finally, during the sampling step, the pixel values will be quantized for representation in the computer, introducing quantization noise. We will represent all of these noise sources with one function, $\eta(\cdot)$.

Putting the filtering and noise sources together, we arrive at an expression for the spacetime image prior to sampling and reconstruction:

$$E_S^{filt}(x, z) = \eta[E_S(x, z) * h_{pix}(z) * h_{frame}(x)] \quad (3.15)$$

This image is then sampled according to the spatial resolution of the sensor and the frame rate. We represent this sampling process as an impulse train, $i(\frac{x}{\tau_x}, \frac{z}{\tau_z})$, where τ_z is the sensor pixel separation projected along the laser sheet and τ_x is the distance the object moves relative to the scanner between frames. Once we have the sampled, filtered spacetime image, we can employ a reconstruction filter, $h_{rec}(x, z)$, to obtain an approximation to the original continuous image. This final image is then:

$$\tilde{E}_S(x, z) = \left[E_S^{filt}(x, z) \cdot i \left(\frac{x}{\tau_x}, \frac{z}{\tau_z} \right) \right] * h_{rec}(x, z) \quad (3.16)$$

One of the first observations that arises from these equations is the fact that the reconstructed spacetime image is a *continuous* function. Thus, this reconstruction yields a (piece-wise) continuous surface, rather than a set of range samples. In the next chapter, we exploit this observation to extract as much range data as possible.

3.5.3 The spacetime spectrum

Taking the Fourier transforms of Equations 3.11 - 3.16 will provide several insights. For simplicity, we omit the influence of noise and arrive at the following relations:

$$\mathcal{F}(E_S) = F(s_x, s_z) H_{ST}(s_x, s_z) \quad (3.17)$$

$$\mathcal{F}(E_S^{filt}) = \mathcal{F}(E_S) H_{pix}(s_z) H_{frame}(s_x)] \quad (3.18)$$

$$\mathcal{F}(\tilde{E}_S) = [\mathcal{F}(E_S^{filt}) * \tau_x \tau_z i(\tau_x s_x, \tau_z s_z)] H_{rec}(s_x, s_z) \quad (3.19)$$

where $\mathcal{F}()$ is the Fourier transform operator, s_x and s_z are the spatial frequencies in x and z , and F , H_{ST} , H_{pix} , H_{frame} , and H_{rec} are the Fourier transforms of f , h_{ST} , h_{pix} , h_{frame} , and h_{rec} , respectively. Figure 3.9 shows the steps in creating, filtering, and sampling the spacetime image.

Several observations arise from thinking about the Fourier spectrum of the spacetime image. The least surprising is the fact that higher sampling rates permit (and are usually accompanied by) wider H_{pix} and H_{frame} filters, allowing for the acquisition of more of the spacetime spectrum, i.e., higher frequencies. In other words, a higher sampling rate leads to more captured detail.

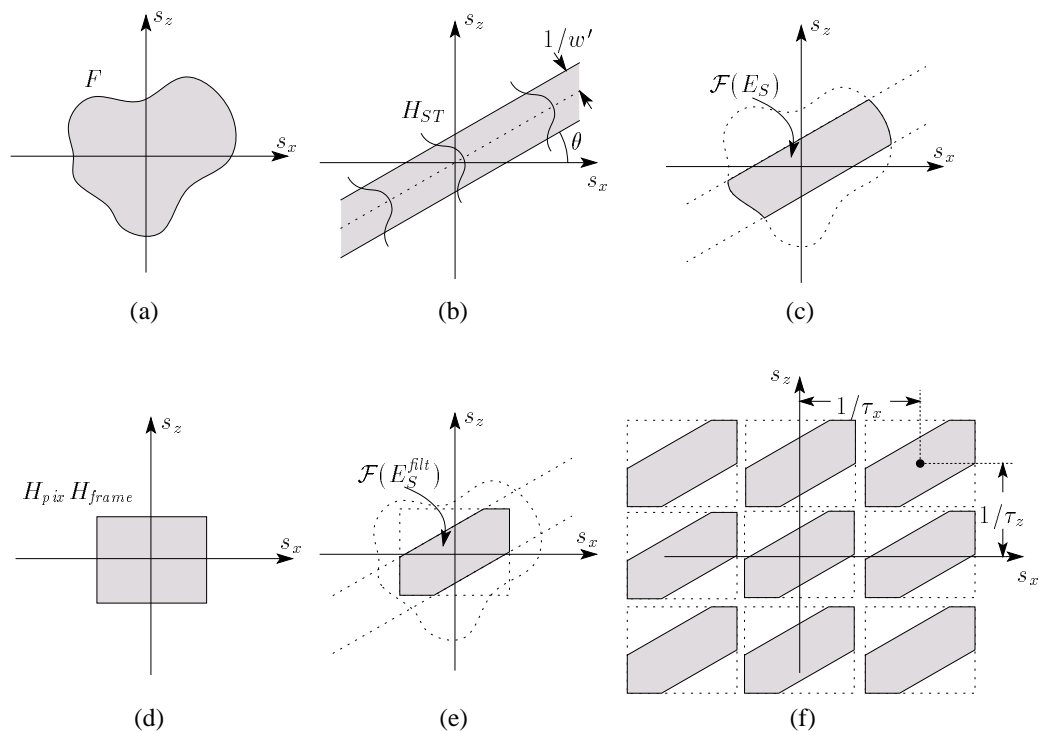


Figure 3.9: The spacetime spectrum: a visualization for Equations 3.17 - 3.19. The Fourier transform of the shape function (a) is multiplied by the spectrum of the spacetime Gaussian (b) to give the spectrum of the ideal spacetime image (c). Before sampling, this spectrum is multiplied by the pixel and frame filters (shown as idealized low-pass filters in (d)) to give the filtered spacetime spectrum without noise (e). The sampling process creates replicas of this filtered spectrum (f) spaced $1/\tau_x$ and $1/\tau_z$ apart in s_x and s_z respectively. The reconstruction step entails extracting the central replica of the spectrum after multiplying by H_{rec} (not shown).

3.5.4 Widening the laser sheet

The Fourier spectrum also tells us that the spacetime Gaussian acts like a bandlimiting filter that runs along the sensor lines of sight, as indicated in Figure 3.9c. Note that this “filter” does not remove detail, as in the case of the pixel and frame filters. The resulting spacetime image is still ideal and contains all the information required to extract the original surface geometry precisely. Thus, by narrowing the spectrum of the spacetime Gaussian, we can restrict the spectrum of the spacetime image without loss of detail. The surprising conclusion: *widening* the illuminant can improve results.

Consider scanning a line (a plane in 3D), as depicted in Figure 3.10. The Fourier transform of this line is another line, perpendicular to the first. After superimposing the spectrum of the spacetime Gaussian, we arrive at the ideal spacetime spectrum, which is basically a line segment in the Fourier plane. The length of this line segment corresponds to the maximum frequency content of the spectrum and thus determines the sampling rate needed to acquire the surface. The parameters that determine the length of the Fourier line segment are the orientation of the original line, the width of the laser sheet, and the triangulation angle. For a fixed laser width and triangulation angle, the spectral line segment grows in length as the line is rotated to be at more of a grazing angle to the sensor. At a critical angle, the pixel and frame filters begin to clip the spectral line segment and degrade the quality of the reconstruction; worse, if the filters are not ideal (and, generally, they are not), aliasing will occur. By widening the laser sheet, however, this critical angle can be extended closer to the triangulation angle.

This notion of widening the laser sheet runs counter to the intuition that a narrower illuminant gives better localization of the point on the surface being acquired. This intuition, however, stems from thinking of triangulation in the traditional context. In the spacetime context, the wider beam does not degrade resolution by “blurring” neighboring points together. It is interesting to note that while the accuracy of the traditional method improves with a narrower laser sheet in principle, in practice the laser must have a minimum thickness to avoid range errors due to aliasing. For a surface of fixed orientation, narrowing the laser sheet also narrows the imaged Gaussian on the sensor, until eventually it is narrower than a pixel cell. At this point, the accuracy is limited by the width of a pixel projected onto the

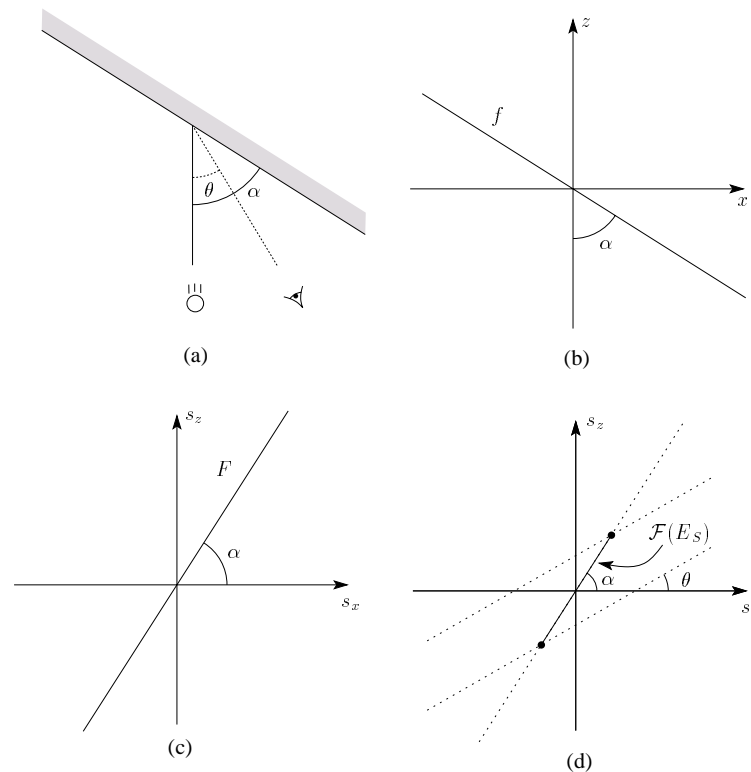


Figure 3.10: Spacetime spectrum for a line. (a) A line at angle α to the laser is scanned. (b) The function to be convolved with the spacetime Gaussian is a delta function line. (c) Its Fourier transform is another delta function line oriented perpendicular to the original. (d) After “filtering” with the spacetime Gaussian, the spacetime spectrum is essentially a line segment in the Fourier plane.

laser sheet, *not* the width of the laser.

In practice, the laser sheet cannot be widened arbitrarily. The primary limitation is the depth of field of the sensor. As the laser is widened, the sensor must record more of the object that is out of the plane of focus. The out of focus points will be blurred, and the improvement from the laser sheet will be countered. One solution might be to use a brighter beam and then stop down the sensor’s aperture to increase the depth of field. However, for coherent illumination, the narrowed aperture leads to increased speckle noise which can also defeat the improved accuracy. Even incoherent imaging systems will approach a diffraction limit as the aperture is narrowed. In addition, as the laser sheet widens, then the effects of using a sensor with perspective projection become more prevalent, as noted in Section 3.3. Further, speckle analysis indicates that widening the laser sheet increases the influence due

to speckle noise. Nevertheless, by balancing these trade-offs, it should be possible to realize a system with improved accuracy. This remains an area for future work.

3.5.5 Improving resolution

Fourier analysis of the spacetime image also reminds us of the importance of using good bandlimiting filters, H_{pix} and H_{frame} , to avoid aliasing artifacts. However, we do not have much control over these filters. The pixel filter is essentially the convolution of the blurring due to finite pixel cell size with any optical blurring that may occur. When the laser sheet is in focus, then the sensor's pixel response is the primary filter, which in turn is set by the design of the sensor. The frame filter is essentially a rectangle function in x with width proportional to the exposure time. In addition, sensors generally have a time interval when they stop capturing light while shifting out the recorded signals. The spectral bandwidth of the temporal filter is thus wider than the distance between samples. In both the spatial and temporal cases, some aliasing artifacts are bound to occur. This aliasing generally leads to reduction in image quality; however, it also means that multiple spacetime images may be combined to improve the accuracy of the range data. Techniques such as the one described in [Irani & Peleg 1991] could be used to combine these spacetime images. In order for such an approach to work, a sequence of spacetime images must be acquired after translating the object (or scanner) between scans. Rotating the object (or scanner) between scans generates an entirely new spacetime image that may not be combined with prior acquisitions. Increased resolution through combination of multiple spacetime images remains an area for future work.

Chapter 4

Spacetime analysis: implementation and results

The previous chapter provides a theoretical foundation for accurate optical triangulation through spacetime analysis. In this chapter, we demonstrate that the method can be adapted to work with an existing commercial laser triangulation scanner (Section 4.1). We develop an efficient algorithm for performing the spacetime analysis and show how increased resolution can be obtained by interpolating the imaged light reflections (Section 4.2). Finally, we show the results of applying the spacetime analysis to some real objects (Section 4.3).

4.1 Hardware

We have implemented the spacetime analysis presented in the previous chapter using a commercial laser triangulation scanner and a real-time digital video recorder. The optical triangulation system we use is a Cyberware MS 3030 platform scanner (shown in Figure 1.5). This scanner collects range data by casting a laser stripe onto the object and by observing reflections with a CCD camera positioned at an angle of 30° with respect to the plane of the laser. The platform can either translate or rotate an object through the field of view of the triangulation optics. Figure 1.2b illustrates the principle of operation. The laser width (the distance between the beam center and the e^{-2} point) varies from 0.8 mm to 1.0 mm over the field of view which is approximately 30 cm in depth and 30 cm in height. Each CCD pixel

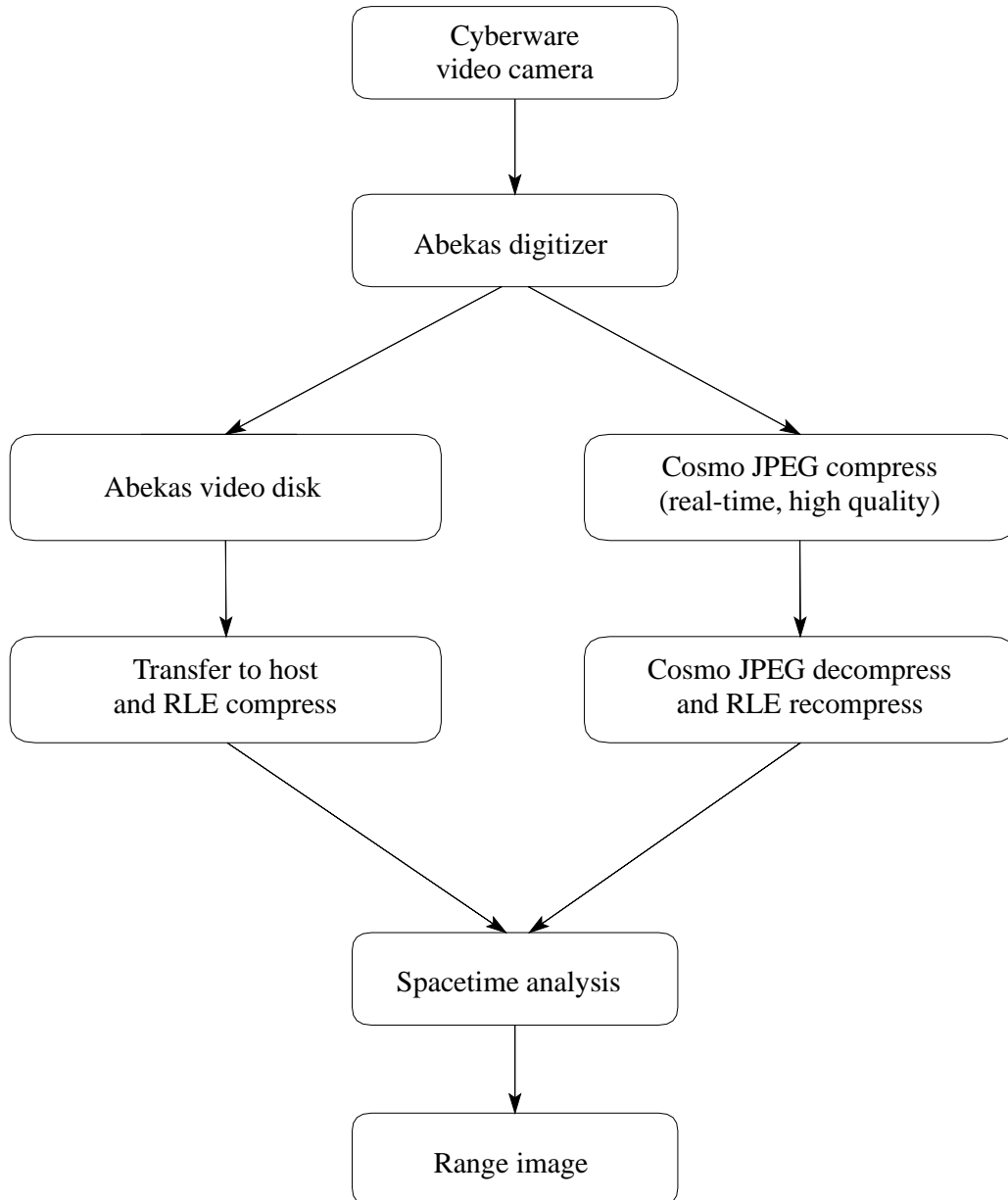


Figure 4.1: From range video to range image. To perform the spacetime analysis, we digitize the Cyberware video with an Abekas digitizer. We can then either store the digitized video to disk and copy it to the host computer, or perform a real-time JPEG compression and fast decompression through an SGI Cosmo board. The JPEG compression approach has proven to be more time efficient, but the results in this chapter were originally obtained with the video disk option. In either case, the frames are run-length encoded and then converted to a range image through the spacetime analysis.

images a portion of the laser plane about 0.5 mm square. Although the Cyberware scanner performs a form of peak detection in real time, we require the actual video frames of the camera for our analysis. Figure 4.1 illustrates the possible routes for processing the range video. We can digitize these frames with an Abekas A20 video digitizer, which can acquire 486 by 720 pixel frames at 30 Hz. The captured frames have approximately the same resolution as the Cyberware CCD camera, though the scanlines are first converted to analog video before being resampled and digitized. The digitized frames can then be stored in real time with an Abekas A60 digital video disk. Alternatively, we can run the digitized signal through a commercially available JPEG compression board. Because each frame is an image of the narrow laser sheet intersecting the surface, it is mostly blank. As a result, we can JPEG compress the frame with a high quality factor, but still obtain high compression. The JPEG compression efficiently encodes the blocks of empty space without sacrificing the quality of the imaged light reflections. The key advantage of this approach is that the range video compresses well enough to be stored on the host computer's main memory, as opposed to a video disk which limits the speed of recovery of the recorded frames. The results in this chapter were obtained with the Abekas digital video disk, but the results described in Chapter 8 are based on range data acquired with the help of JPEG compression.

4.2 The spacetime algorithm

Using the principles of the previous chapter, we can devise a procedure for extracting range data from spacetime images:

1. Perform the range scan and capture the spacetime images.
2. Rotate the spacetime images by θ .
3. Find the statistics of the Gaussians in the rotated coordinates.
4. Rotate the means back to the original coordinates.

Figure 4.2 illustrates this new method graphically. In order to implement step 1 of this algorithm, we require a sequence of CCD images. Most commercial optical triangulation

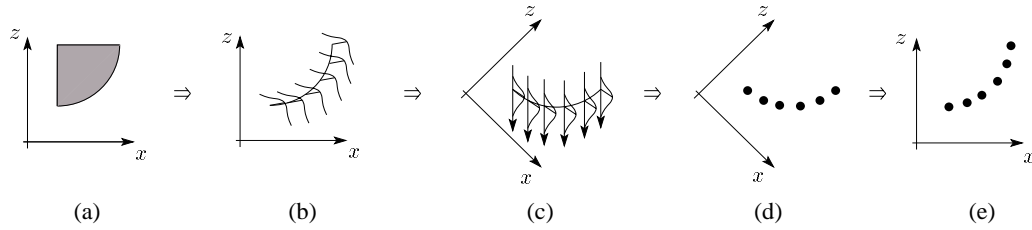


Figure 4.2: Method for optical triangulation range imaging with spacetime analysis. (a) The original geometry. (b) The resulting spacetime image when scanning with the illuminant in the $+z$ direction. (c) Rotation of the spacetime image followed by evaluation of Gaussian statistics. (d) The means of the Gaussians. (e) Rotation back to world coordinates.

systems discard each CCD image after using it (e.g. to compute a stripe of the range map). As described in the previous section, we have assembled the necessary hardware to record the CCD frames. In the previous chapter, we discussed a one dimensional sensor scenario and indicated that perspective imaging could be treated as locally orthographic. For a two dimensional sensor, we can imagine the horizontal scanlines as separate one dimensional sensors with varying vertical (y) offsets. Each scanline generates a spacetime image, and by stacking the spacetime images one atop another, we define a spacetime *volume*. Complications arise when we have perspective projection in the vertical direction, as the image of a point sweeping through the Gaussian illuminant can cross scanlines (i.e., a point is not constrained to lie in a single spacetime image plane). We have not yet implemented the general spacetime ranging method that accounts for this effect, so we restrict most of our analysis to the spacetime volume near the vertical centerline of the CCD where range points will not cross scanlines while passing through the illuminant (i.e., we can visualize the spacetime volume as a stack of spacetime images). Nevertheless, toward the end of this chapter, we demonstrate some results for larger objects that show improvement even though they are not restricted to the center of the field of view in the vertical direction. This improvement is probably due to the fact that even at the extreme positions of the field of view a point does not traverse more than half a scanline while passing through the illuminant.

In step 2, we rotate the spacetime images so that Gaussians are vertically aligned. In a practical system with different sampling rates in x and z , the correct rotation angle can be computed as:

$$\tan \theta_{ST} = \frac{\tau_z}{\tau_x} \tan \theta \quad (4.1)$$

where θ_{ST} is the new rotation angle, τ_x and τ_z are the sample spacings in x and z respectively, and θ is the triangulation angle. In order to determine the rotation angle, θ_{ST} , for a given scanning rate and region of the field of view of our Cyberware scanner, we first determined the local triangulation angle and the sample spacings in depth, z , and lateral position, x . Equation 4.1 then yields the desired angle. When performing the rotation, we avoid aliasing artifacts which would lead to range errors by employing high-quality filters. For this purpose, we use a bicubic interpolant.

After performing the rotation of each spacetime image, we compute the statistics of the Gaussians along each rotated spacetime image raster¹. Our method of choice for computing these statistics is a least squares fit of a parabola to the log of the data; i.e, given a Gaussian of the form:

$$G(x) = a \exp \left[-\frac{2(x-b)^2}{w^2} \right]$$

where a is the amplitude and b is the desired center, we can take the log of the Gaussian:

$$\log[G(x)] = \log[a] - \frac{2(x-b)^2}{w^2} = \left(-\frac{2}{w^2} \right) x^2 + \left(\frac{4b}{w^2} \right) x + \left(\log[a] - \frac{2b^2}{w^2} \right)$$

and fit a parabola to the result. The linear coefficient contains the center, b .

We have also experimented with fitting the data directly to Gaussians using the Levenberg-Marquardt non-linear least squares algorithm [Press et al. 1986], but the results have been substantially the same as the log-parabola fits.

The Gaussian statistics consist of a mean, which corresponds to a range point, as well as a width and a peak amplitude, both of which indicate the reliability of the data. Widths that are far from the expected width and peak amplitudes near the noise floor of the sensor imply unreliable data which may be down-weighted or discarded during later processing (e.g.,

¹Actually, we do not expect to find perfect Gaussians on the rotated image rasters. The filtering and sampling processes described in Section 3.5 alter the ideal spacetime image. Nevertheless, fitting Gaussians is a reasonable approximation that has yielded excellent results in practice

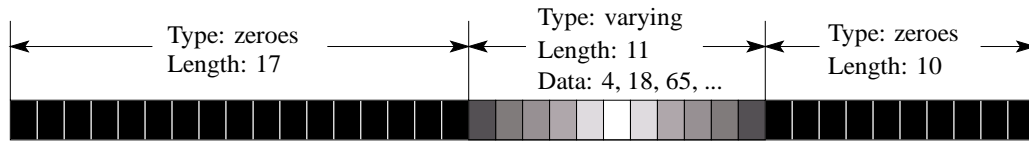


Figure 4.3: Run-length encoded spacetime scanline. Each scanline is composed of runs of zeroes and runs of varying intensity data.

when combining multiple range meshes). For the purposes of this thesis, we discard unreliable data and rely on future scans to fill in reliable data used in the surface reconstruction process.

Finally, in step 4, we rotate the range points back into the global coordinate system.

4.2.1 Fast rotation of the spacetime image

In order to process the spacetime images, we first compress the frames into a run length encoded (RLE) representation as shown in Figure 4.3. The time evolution of a single scanline is thus a run length encoded spacetime image which we must rotate in order to extract range data. The naive approach to rotating each image would be to expand it into uncompressed form, and then visit the pixels of the target image while walking through the rotated source slice, i.e., while “gathering” data from the source slice. Alternatively, we can process the source image’s runs, and only “send” data to the source image in the regions of runs with varying data [Lacroute 1995]. Figure 4.4 illustrates this principle.

Note that when performing the traditional gather approach, we step through the target image and resample the source image using a reconstruction filter. As a result, a neighborhood of source pixels will influence the value of each target pixel, as shown in Figure 4.5c. We can also look at this in another way: each source pixel will influence a neighborhood of target pixels. Thus, when performing the send operation, each pixel adds weighted copies of itself to a neighborhood of pixels in the target image. This send operation is illustrated in Figure 4.5d.

The RLE send method we have described so far will significantly reduce the computational expense, because it visits only the interesting pixels in the source image. Nevertheless, it still creates an uncompressed target image whose pixels must all be visited in the

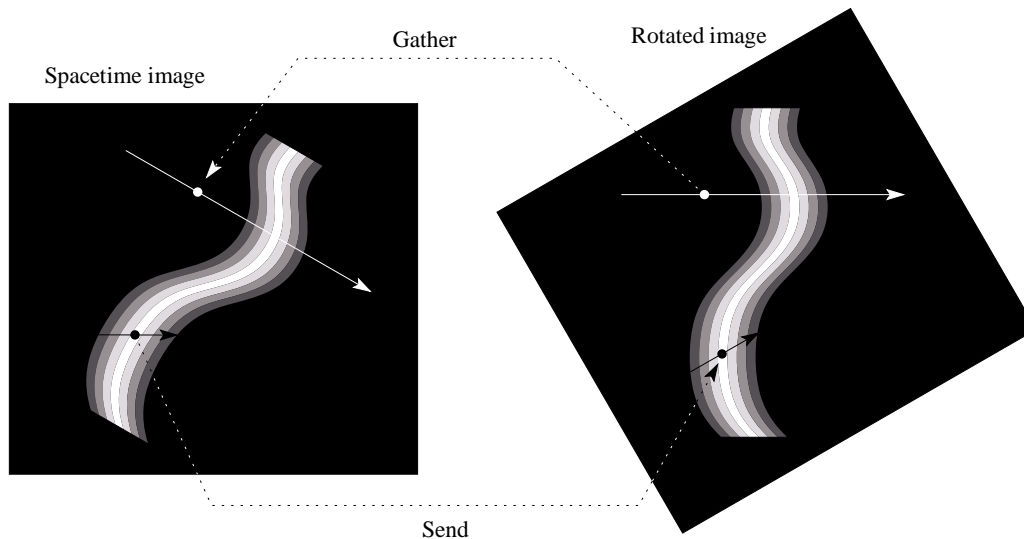


Figure 4.4: Fast RLE rotation. The naive approach to rotating an image would be to expand the RLE source image, and then traverse all of the pixels of the target image while “gathering” data from (resampling) the source image. A much more efficient approach is to traverse the RLE structure in the source image and “send” only non-zero data to the target image.

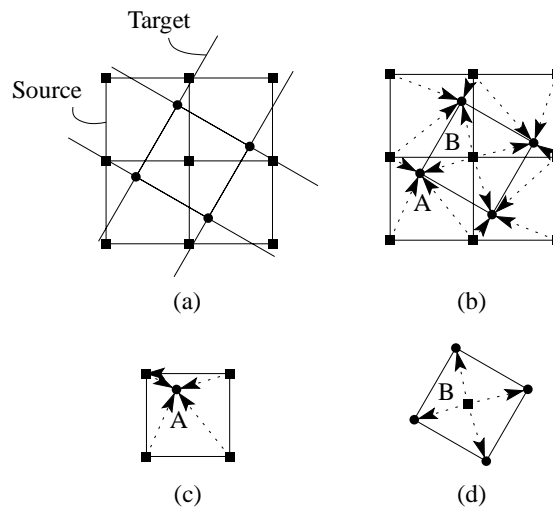


Figure 4.5: Reconstruction: send vs. gather. (a) The target image is rotated with respect to the source image. (b) We can find the values at the target pixels by interpolating among the source pixels. (c) “Gather” interpolation for a single target image pixel, A. (d) “Send” interpolation for a single source pixel. The example in this figure illustrates the case for a bilinear filter with a 2x2 support; extension to filters with larger supports is straightforward.

next step of the spacetime algorithm. Ideally, we would like to create an RLE target image directly. We can achieve this goal with the following procedure:

1. Allocate space for each scanline in the target image.
2. Stream through each source scanline, ignoring runs of zeroes. When sending varying data:
 - If the data being sent is not within the current target run being constructed:
 - Mark the current target run as finished.
 - Declare a run of zeroes between the finished run and the new target position.
 - Start a new run of varying pixels.
 - Else,
 - Deposit the pixel value into the existing run, increasing its length as needed.
3. Mark the last run on each scanline as being a run of zeroes.

Figure 4.6 shows a scanline as it is being constructed.

This RLE rotation algorithm delivers a dramatic performance improvement. If we consider a spacetime volume of n voxels on a side, then the brute force rotation would execute in time proportional to the size of the volume, i.e., $O(n^3)$. On the other hand, the fast algorithm described here requires time proportional to the part of the volume with non-zero data. The sensor samples the surface onto a grid of size roughly $n \times n$, which is then “blurred” into the spacetime volume by the spacetime impulse response (Equation 3.11). The width of this impulse response function is constant, so the overall size of the spacetime surface embedded in the volume is $O(n^2)$. Thus, the fast rotation algorithm runs in $O(n^2)$ time, substantially faster than the brute force method. In practice, we observe a typical speed-up of 50:1 over the brute force approach.

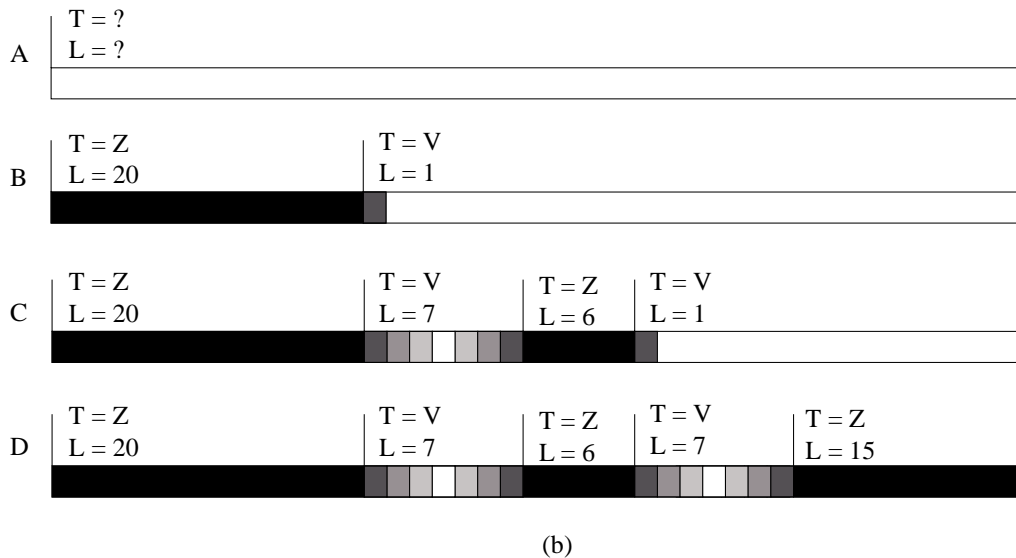
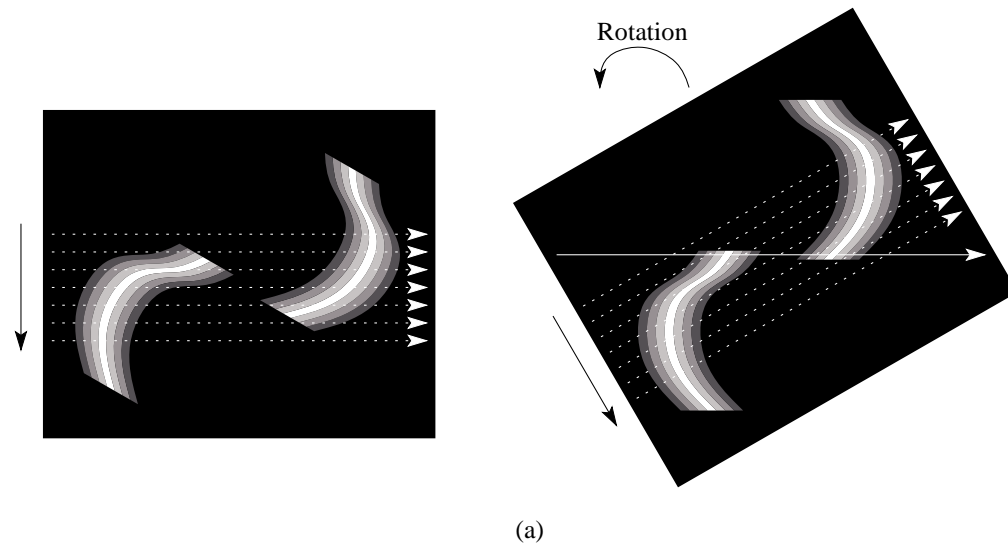


Figure 4.6: Building a rotated RLE scanline. (a) The source image is traversed in scanline order (dotted white lines) from top to bottom (solid black arrow to the left), and the non-zero values are deposited in the target image. (b) The scanline indicated by the solid white arrow in the target image is constructed in steps. “T” is the data type, and “L” is the run length. In A, The scanline is initialized to have no data or length. In B, when the first source scanline intersects the target scanline, the first run is declared to be zeroes (T = Zero or “Z”) and its length is computed. In addition, a varying run (T = Varying or “V”) is begun. As successive source scanlines intersect the target scanline, more varying data is added to the current run, which grows as needed. At C, more varying data is laid down, but it is offset from the first varying run. Thus, a new run of zeroes is declared with its length, and a new varying run is begun. Eventually, the source scanline sweep finishes, and the remainder of the scanline is declared to be zeroes, as shown in D.

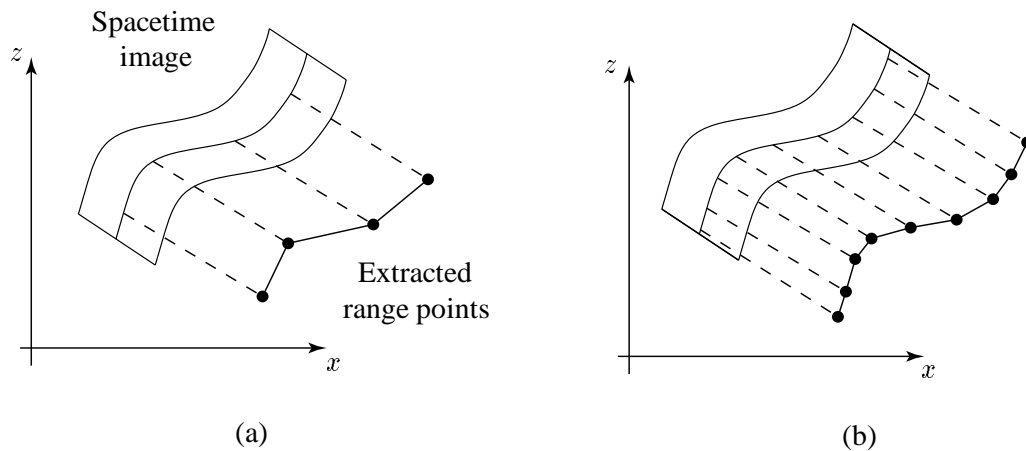


Figure 4.7: Interpolation of spacetime image data. (a) Extraction of range data from a spacetime image followed by linear interpolation of the range points. (b) Same as (a) but more interpolation in the spacetime image rather than the among the range points.

4.2.2 Interpolating the spacetime volume

Traditionally, researchers have extracted range data at sampling rates corresponding to one range point per sensor scanline per unit time. Interpolation of shape between range points has consisted of fitting primitives (e.g., linear interpolants like triangles) to the range points. Instead, we can regard the spacetime volume as the primary source of information we have about an object. After performing a scan, we have a sampled representation of the spacetime volume, which we can then reconstruct to generate a continuous function. In the previous chapter, we described this reconstruction for a spacetime image; for the spacetime volume, we have added a vertical dimension, but the principle remains the same. This reconstructed function then acts as our range “oracle,” which we can query for range data at a resampling rate of our choosing. Figure 4.7 illustrates this idea for a single spacetime image. In practice, we can magnify the sampled spacetime volume prior to applying the range imaging steps described above. The result is a range grid with a higher sampling density directly derived from the imaged light reflections.

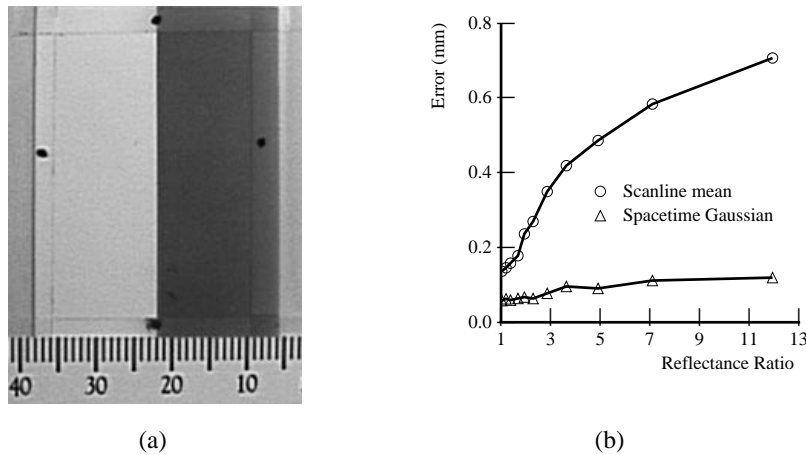


Figure 4.8: Measured error due to reflectance step. (a) Printed cards with reflectance discontinuities were carefully taped to a machined planar surface. The black dots were used to distinguish the taped boundary from the target surface. (b) A plot of range errors shows that the spacetime method yields a 60-80% reduction in range error for steps varying from 1:1 to 12:1.

4.3 Results

We have performed a variety of tests to evaluate the performance of traditional triangulation and spacetime analysis. These tests include experiments with reflectance variations, simple shape variations, errors due to speckle, and scanning complex objects.

4.3.1 Reflectance correction

To evaluate the tolerance of the spacetime method to changes in reflectance, we performed two experiments, one quantitative and the other qualitative. For the first experiment, we produced reflectance steps by printing alternating white and gray stripes with a color printer. By varying the reflectances of the solid gray stripes, we obtained reflectance ratios (white:gray) of about 1:1 to 10:1. We scanned them at an angle of 30° (roughly facing the sensor) and extracted range data using both the traditional method and the spacetime method. To measure deviations from planarity, we first computed the parameters of the plane by deleting those range points lying in the neighborhood of the reflectance discontinuity. This step avoids permitting erroneous data to influence the estimated orientation of the plane. When computing range errors, we used all range data, including points near the reflectance discontinuity.

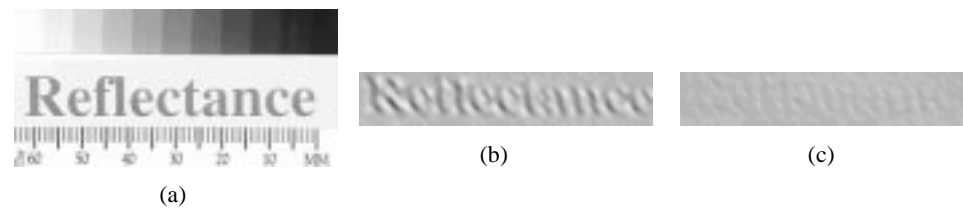


Figure 4.9: Reflectance card. (a) Photograph of a planar card with the word “Reflectance” printed on it. (b) and (c) Shaded renderings of the range data generated by traditional mean analysis and spacetime analysis, respectively. With traditional mean analysis, the planar card appears embossed with the lettering, indicating a confusion between reflectance and shape. The spacetime analysis yields a nearly planar surface, showing a disambiguation of reflectance and shape.

Figure 4.8 shows a plot of maximum deviations from planarity. The spacetime method has clearly improved over the old method. The reduction in range errors varies from 65% for a reflectance change of 2:1 up to 85% for a reflectance change of 12:1.

For qualitative comparison, we produced a planar sheet with the word “Reflectance” printed on it. Figure 4.9 shows the results. The old method yields a surface with the characters well-embossed into the geometry, whereas the spacetime method yields a much more planar surface indicating successful decoupling of geometry and reflectance.

4.3.2 Shape correction

We conducted several experiments to evaluate the effects of shape variation on range acquisition. In the first experiment, we generated corners of varying angles by abutting sharp edges of machined aluminum wedges which were painted white. Figure 4.10 shows the range errors that result for traditional and spacetime methods. Again, we see an increase in accuracy, though not as great as in the reflectance case.

We also scanned two 4 mm strips of paper at an angle of 30° (roughly facing the sensor) to examine the effects of depth discontinuities. Figure 4.11b shows the “edge curl” observed with the old method, while the spacetime method in Figure 4.11c shows a significant reduction of this artifact under spacetime analysis. We have found that the spacetime method reduces the length of the edge curl from an average of 1.1 mm to an average of approximately 0.35 mm.

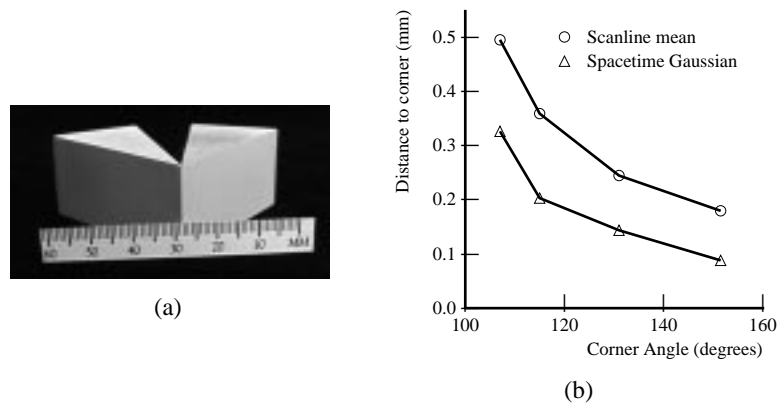


Figure 4.10: Measured error due to corner. (a) Two machined wedges with razor sharp corners were placed at varying angles to each other to study the effect of corner angle on range accuracy. (b) A plot of range errors shows that the spacetime method yields a 35-50% reduction in range error for corners of angles varying from 110° to 150° .

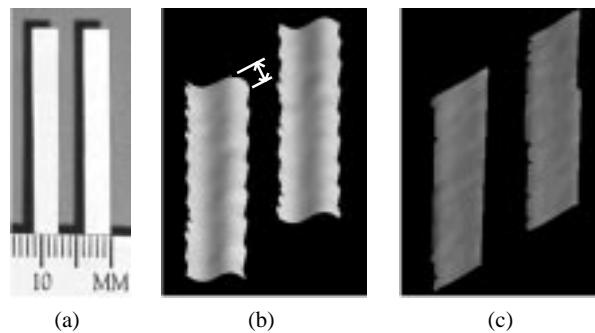


Figure 4.11: Depth discontinuities and edge curl. (a) Photograph of two strips of paper. (b) and (c) Shaded renderings of the range data generated by traditional mean analysis and spacetime analysis, respectively. With traditional mean analysis, the edges of the strips exhibit large edge curl artifacts (1.1 mm between the hash marks in (b)). The curl is nearly eliminated when using the spacetime analysis.

Finally, we impressed the word “SHAPE” onto a plastic ribbon using a commonly available label maker. In Figure 4.9, we wanted the word “Reflectance” to disappear because it represented changes in reflectance rather than in geometry. In Figure 4.12, we want the word “SHAPE” to stay because it represents real geometry. Furthermore, we wish to resolve it as highly as possible. Figure 4.12 shows the result. Using traditional mean analysis, the word is barely visible. Using spacetime analysis, the word becomes legible.

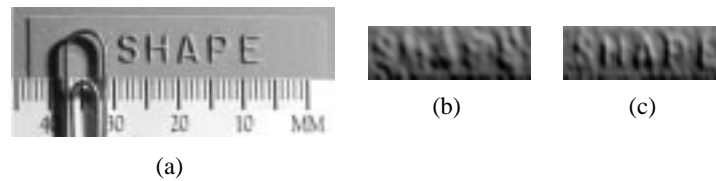


Figure 4.12: Shape ribbon. (a) Photograph of a surface with raised lettering (letters are approx. 0.3 mm high). (b) and (c) Shaded renderings of the range data generated by traditional mean analysis and spacetime analysis, respectively. Using mean pulse analysis, the lettering is hardly discernible, while the spacetime analysis yields a legible copy of the original shape.

4.3.3 Speckle

To evaluate the influence of laser speckle, we scanned planar surfaces of varying roughness under coherent and incoherent light. First, we verified the existence of the laser speckle. Recording the light reflections from the surfaces under incoherent (single filament, non-diffuse) illumination showed negligible variation ($< 5\%$) in image intensity, while the images of laser reflections showed significant variations ($> 20\%$) in peak intensity. These facts, coupled with the observation that surfaces with roughness finer than the resolution of the pixels yielded variations at a scale larger than a pixel, lead us to believe that we are observing laser speckle.

Next, we performed range scans on the planar surfaces and generated range points using the traditional and spacetime methods. After fitting planes to range points, we found that both methods resulted in range errors with a standard deviation of about 0.06 mm and a distribution that is very nearly Gaussian (see Figure 4.13). As expected, both traditional and spacetime triangulation are susceptible to errors due to laser speckle. In Section 2.2.4, we computed the range error for a perfectly rough surface to be 0.25 mm. Since the surface being measured is unlikely to be perfectly rough, it is not surprising that the measured error is less.

4.3.4 Complex objects

To show how the spacetime analysis performs with more complex objects occupying a larger portion of the field of view, we scanned two models. Figure 4.14 shows the results for a model tractor. Figure 4.14b is a rendering of the data generated by the Cyberware scanner

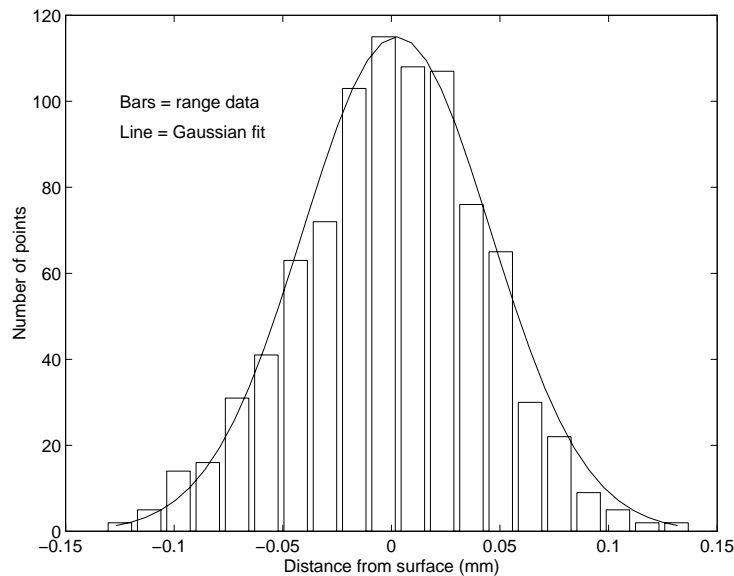


Figure 4.13: Distribution of range errors over a planar target. We extracted the range data using spacetime analysis and fit a plane through the resulting data. The bar graph represents a histogram of distances from the planar fit, while the curve corresponds to a Gaussian approximation to the histogram.

hardware and is particularly noisy. This added noisiness results from the method of pulse analysis performed by the hardware, a method similar to peak detection. Peak detection is especially susceptible to speckle noise, because it extracts a range point based on a single value or small neighborhood of values on a noisy curve. Mean analysis tends to average out the speckle noise, resulting in smoother range data as shown in Figure 4.14c. Figure 4.14d shows our spacetime results and Figure 4.14e shows the spacetime results with 3X interpolation and resampling of the spacetime volume as described in Section 4.2. Note the sharper definition of features on the body of the tractor.

Figure 4.15 shows the result for a model of an alien creature. As with the tractor image, the Cyberware output is noisier than the traditional mean analysis results. Note, however, that the traditional mean analysis appears to smooth the geometric detail more than the Cyberware method. Both the Cyberware and the mean analysis suffer from edge curl. By contrast, the spacetime method reduces edge curl, exhibits less noise, and attains comparable or greater detail than either of the other methods.

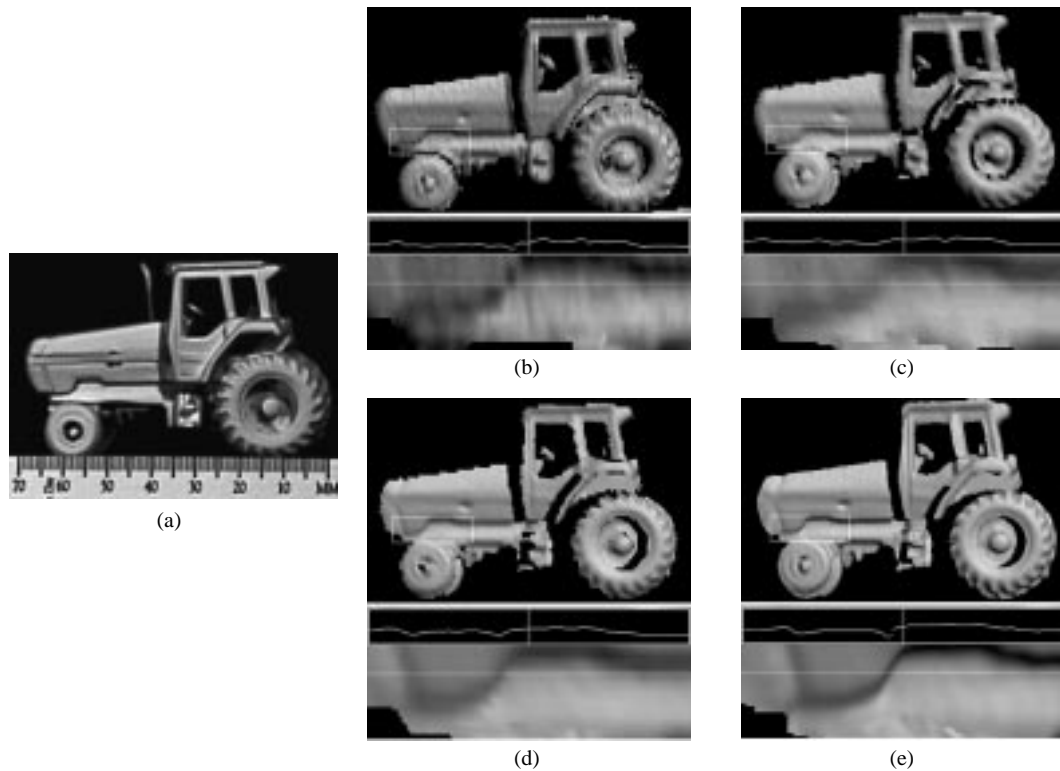


Figure 4.14: Model tractor. (a) Photograph of original model and shaded renderings of range data generated by (b) the Cyberware scanner hardware, (c) mean pulse analysis, (d) our spacetime analysis, and (e) the spacetime analysis with 3X interpolation of the spacetime volume before fitting the Gaussians. Below each of the renderings is a blow-up of one section of the tractor body (indicated by rectangle on rendering) with a plot of one row of pixel intensities. Because of the scanner hardware's peak detection method, it is the most susceptible to speckle noise as is evident in the rendering and in the "bumpy" intensity plot. Mean analysis yields a decrease in noise and spacetime analysis yields even less noise and more detail. The 3X interpolated spacetime analysis reveals the most detail of all.

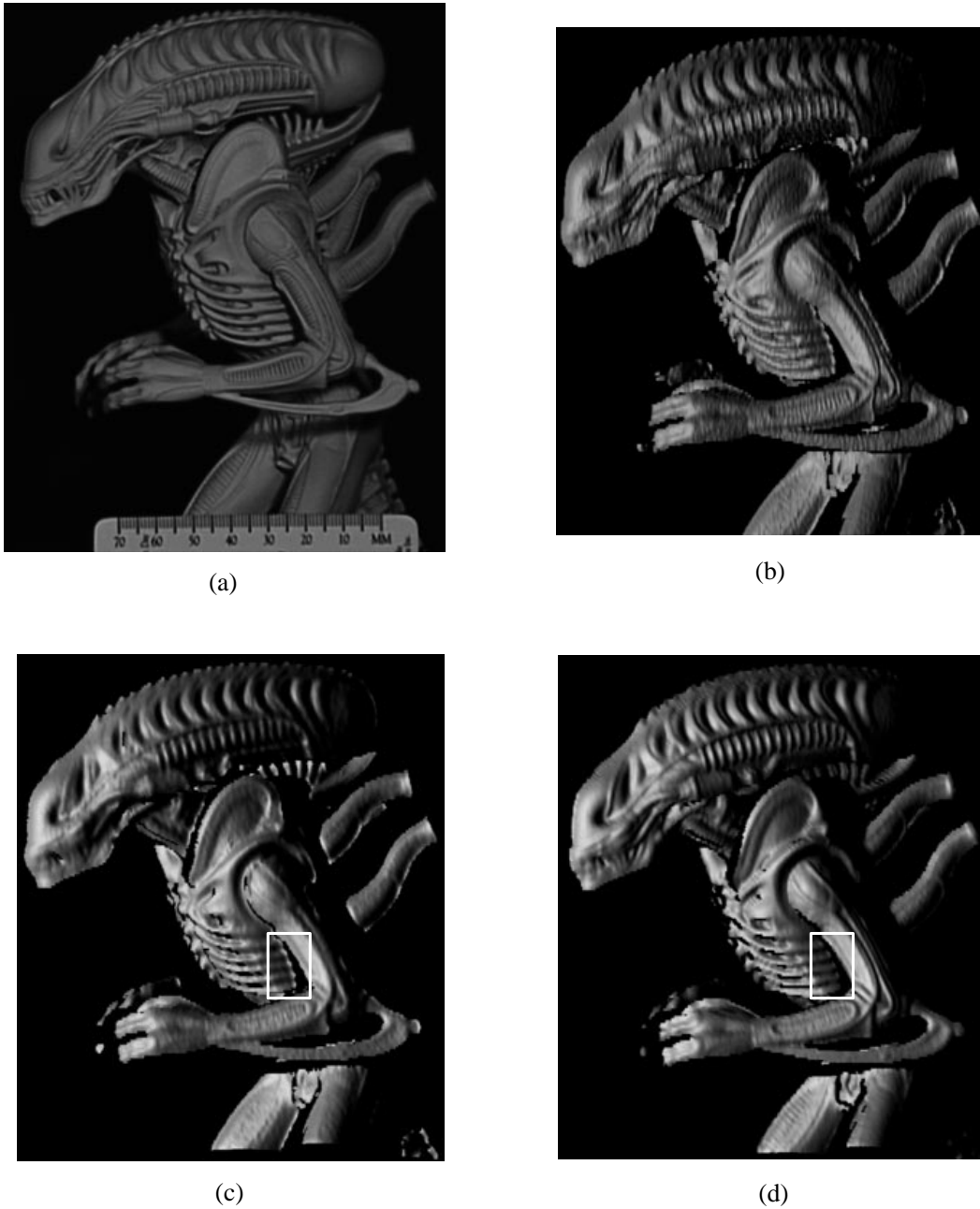


Figure 4.15: Model alien. (a) Photograph of original model and shaded renderings of range data generated by (b) the Cyberware scanner hardware, (c) mean pulse analysis, and (d) our spacetime analysis. The highlighted box in (c) and (d) shows the reduction of edge curl along the depth discontinuity at the alien's torso where the CCD line of sight was occluded. Note that only the spacetime method resolves the ridges in the right leg.

4.3.5 Remaining sources of error

The results we presented in this section clearly show that the spacetime analysis yields more accurate range data, but the results are imperfect due to system limitations. These limitations include:

- CCD noise
- Finite sensor resolution
- Optical blurring and electronic filtering
- Quantization errors
- Calibration errors
- Surface-surface inter-reflections

In addition, we observed some electronic artifacts in our Cyberware scanner that influenced our results. We expect, however, that any measures taken to reduce the effects of the limiting factors described above will lead to higher accuracy. By contrast, if one uses traditional methods of range extraction, then increasing sensor resolution and reducing the effects of filtering alone will *not* significantly increase tolerance to reflectance and shape changes when applying the traditional methods of range extraction.

Chapter 5

Surface estimation from range images

The second part of this thesis is concerned with building computer models from range images such as might be generated using the method described in the first part of the thesis.

As stated in Chapter 1, the problem of reconstructing a surface from range images can be stated as follows:

Given a set of p aligned, noisy range images, $\hat{f}_1, \dots, \hat{f}_p$, find the 2D manifold that most closely approximates the points contained in the range images.

where each function, \hat{f}_i is a sampling of the actual surface f , and each sample, $\hat{f}_i(j, k)$ is the observed distance to the surface as seen along the line of sight indexed by (j, k) . The problem of finding this manifold hinges on defining how well any manifold approximates the range images, and then solving for the “best” manifold. In this chapter, we begin with a discussion of prior work in reconstructing surfaces from range data. Next, we describe range imaging in more detail and then construct a probabilistic model relating possible manifolds to range image samples. In Section 5.4, we define the best surface as the Maximum Likelihood surface, and we define the integral that this surface must minimize. In Section 5.5, we show how to bring the integral under a unified domain using a vector field analogy for range image sampling. In Section 5.6, we derive some results from the calculus of variations needed for the solution of this minimization problem. Finally, in Section 5.7, we solve the minimization equation for surface reconstruction from range images. As a special case,

we relate the least squares minimization (corresponding to Gaussian statistics) to the search for a zero crossing of weighted sums of signed distance functions.

5.1 Prior work in surface reconstruction from range data

Surface reconstruction from dense range data has been an active area of research for several decades. The strategies have proceeded along two basic directions: reconstruction from unorganized points, and reconstruction that preserves the underlying structure of the acquired data. These two strategies can be further subdivided according to whether they operate by reconstructing polygonal surfaces or by reconstructing an implicit function.

5.1.1 Unorganized points: polygonal methods

A major advantage of the unorganized points algorithms is the fact that they do not make any prior assumptions about connectivity of points. In the absence of range images or contours to provide connectivity cues, these algorithms are the only recourse. Among the polygonal surface approaches, Boissonnat [1984] describes a method for Delaunay triangulation of a set of points in 3-space. Edelsbrunner & Mücke [1992] generalize the notion of a convex hull to create surfaces called alpha-shapes.

5.1.2 Unorganized points: implicit methods

Examples of implicit surface reconstruction include the method of Hoppe et al. [1992] for generating a signed distance function followed by an isosurface extraction. More recently, Bajaj et al. [1995] used alpha-shapes to construct a signed distance function to which they fit implicit polynomials.

Although unorganized points algorithms are widely applicable, they discard useful information such as surface normal and reliability estimates. As a result, these algorithms are well-behaved in smooth regions of surfaces, but they are not always robust in regions of high curvature and in the presence of systematic range distortions and outliers.

5.1.3 Structured data: polygonal methods

Among the structured data algorithms, several polygonal approaches have been proposed. Soucy & Laurendeau [1992] describe a method using Venn diagrams to identify overlapping data regions, followed by re-parameterization and merging of regions. Turk & Levoy [1994] employ an incremental algorithm that updates a reconstruction by eroding redundant geometry, followed by zippering along the remaining boundaries, and finally a “consensus” step that reintroduces the original geometry to establish final vertex positions. Rutishauser et al. [1994] use errors along the sensor’s lines of sight to establish consensus surface positions followed by a re-tessellation that incorporates redundant data. These algorithms typically perform better than unorganized point algorithms, but they can still fail catastrophically in areas of high curvature.

5.1.4 Structured data: implicit methods

Several algorithms have been proposed for integrating structured data to generate implicit functions. These algorithms can be classified as to whether voxels are assigned one of two (or three) states or are samples of a continuous function.

Discrete-state voxels

Among the discrete-state volumetric algorithms, Connolly [1984] casts rays from a range image accessed as a quad-tree into a voxel grid stored as an octree, and generates results for synthetic data. Chien et al. [1988] efficiently generate octree models under the severe assumption that all views are taken from the directions corresponding to the 6 faces of a cube. Li & Crebbin [1994] and Tarbox & Gottschlich [1994] also describe methods for generating binary voxel grids from range images. None of these methods has been used to generate surfaces. Further, without an underlying continuous function, there is no mechanism for representing range uncertainty in the volumes.

Continuous-valued voxels

The last category of our taxonomy is implicit function methods that use samples of a continuous function to combine structured data. Our method falls into this category. Previous efforts in this area include the work of Grosso et al. [1988], who generate depth maps from stereo and average them into a volume with occupancy ramps of varying slopes corresponding to uncertainty measures; they do not, however, perform a final surface extraction. Succi et al. [1990] create depth maps from stereo and optical flow and merge them volumetrically using a straight average of estimated voxel occupancies. The reconstruction is an isosurface extracted at an arbitrary threshold. In both the Grosso and Succi papers, the range maps are sparse, the directions of range uncertainty are not characterized, they use no time or space optimizations, and the final models are of low resolution. Recently, Hilton et al. [1996] have developed a method similar to ours in that it uses weighted signed distance functions for merging range images, but it does not address directions of sensor uncertainty, incremental updating, space efficiency, and characterization of the whole space for potential hole filling, all of which we believe are crucial for the success of this approach.

5.1.5 Other related work

Other relevant work includes the method of probabilistic occupancy grids developed by Elfes & Matthies [1987]. Their volumetric space is a scalar probability field which they update using a Bayesian formulation. The results have been used for robot navigation, but not for surface extraction. A difficulty with this technique is the fact that the best description of the surface lies at the peak or ridge of the probability function, and ridge finding is not a problem with robust solutions [Eberly et al. 1994].

The discrete-state implicit function algorithms described above also have much in common with the methods of extracting volumes from silhouettes [Connolly 1974] [Martin & Aggarwal 1983] [Hong & Shneier 1985] [Potmesil 1987] [Szeliski 1993]. The idea of using backdrops to help carve out the emptiness of space is one we demonstrate in Chapter 6.

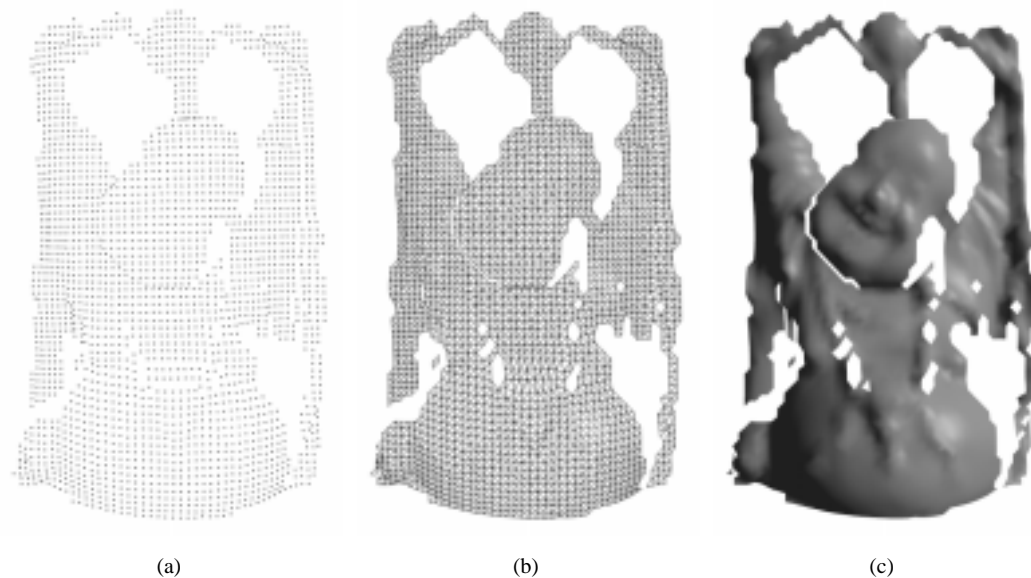


Figure 5.1: From range image to range surface. The range image, $\hat{f}(i, j)$ in (a) is a set of points in 3D acquired on a regular sampling lattice. (b) shows the reconstruction of a range surface, $\tilde{f}(x, y)$, using triangular elements. (c) is a shaded rendering of the range surface.

5.2 Range images, range surfaces, and uncertainty

In the remainder of this chapter, we focus on the problem of reconstructing a surface exclusively from range images. We begin by describing range imaging in more detail.

Numerous range scanning technologies acquire the shape of an object by generating range images. A *range image* is a 2D lattice of range samples, where each sample corresponds to a distance from the sensor along a single line of sight. A *range surface*, \tilde{f} , is a piecewise continuous function reconstructed from a range image. Figure 5.1 shows a range surface reconstructed using triangular elements to connect nearest neighbors in the range image. Such a range surface is a piecewise linear reconstruction, and corresponds to a partial estimate of the shape and topology of the object. To avoid making topological errors such as bridging depth discontinuities, researchers typically set an edge length or surface orientation threshold when establishing connectivity of samples.

Rangefinders might have lines of sight distributed across a range image in any one of a number of different configurations. Figure 5.2 depicts several range scanning geometries and their corresponding viewing frustums. An orthographic imaging frustum may arise

from a 2-axis translational scanning configuration as depicted in Figures 5.2a and 5.2b, though no such commercial system exists to our knowledge. Figure 5.2c shows a time of flight scanner with two rotating mirrors; the lines of sight for such a configuration are nearly perspective, assuming the separation between the mirrors is small. Rangefinders are in general neither precisely orthographic nor precisely perspective. Optical distortions in real range imaging systems typically lead to violations of paraxial assumptions about the imaging optics. In addition, some scanners deviate significantly from orthographic or perspective. For instance, some light stripe triangulation scanners sample an object with a perspective projection within the plane of light, but translate horizontally to fill out the range image. Such a projection is a cylindrical or “line perspective” projection; i.e., it is orthographic in the direction of scanning, and perspective within the scanning plane. This last scanning geometry corresponds to the Cyberware scanner used for this thesis (see Figures 5.2e and 5.2f). When applying traditional methods of optical triangulation, samples lie along rays that correspond to the projection of each CCD scanline onto the laser sheet. These sampling lines of sight need *not* coincide with the lines of sight of the laser (though they do happen to coincide in the Cyberware scanner). Figure 5.3 illustrates this point. When applying the spacetime analysis for triangulation, however, the sampling lines of sight follow the lines of sight of the CCD.

While their range imaging frustums are diverse, most rangefinders do have in common that the lines of sight of the sensor are well calibrated and the range uncertainty lies predominantly in determining depth along these lines of sight. For a time of flight rangefinder, for example, the primary source of uncertainty is in determining the time of arrival of a light pulse relative to its time of emission, resulting in depth errors along the direction of the emitted pulse. In optical triangulation, traditional analysis of imaged laser reflections leads to uncertainties in depth along the laser beam or within the laser sheet, as shown in Figure 2.6. Using the spacetime analysis for optical triangulation, the errors in determining the location of a peak in time, lead to range errors along the camera’s lines of sight, as shown in Figure 3.5. Other researchers have also characterized range errors for optical triangulation, and have found the error to be ellipsoidal, i.e., non-isotropic, about the range points [Hebert et al. 1993] [Rutishauser et al. 1994].

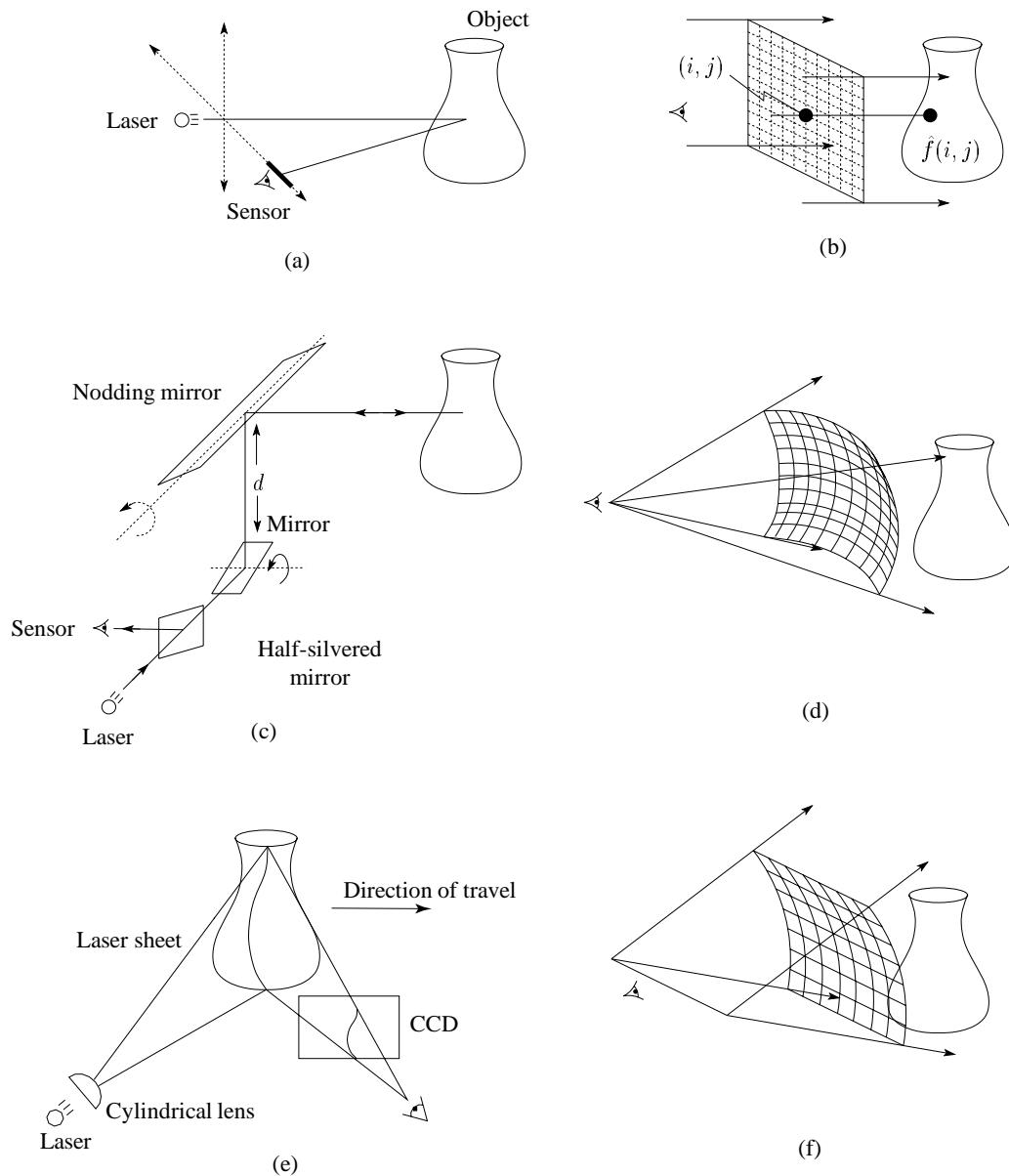


Figure 5.2: Range imaging frustums. (a) An orthographic triangulation scanner using a beam of light and a linear array sensor and (b) its orthographic viewing frustum. The sensor and light move together, stepping in fixed increments horizontally and vertically to traverse its field of view. (c) A time-of-flight scanner with rotating mirrors to scan the beam and sensor line of sight over the object and (d) its approximately perspective viewing frustum (for small mirror separation, d). (e) A translating laser stripe triangulation scanner with an area sensor and (f) its cylindrical projection viewing frustum when using traditional (*not* spacetime) triangulation analysis.

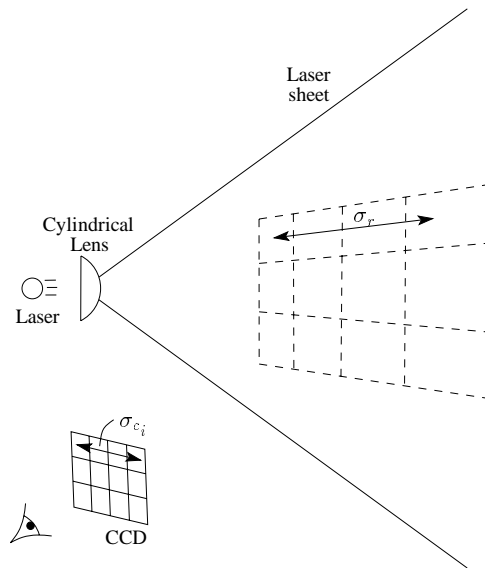


Figure 5.3: Range errors for traditional triangulation with two-dimensional imaging. A typical optical triangulation system uses a laser beam spread into a diverging sheet of light with a cylindrical lens and a CCD that images reflections from within this sheet. Range is usually determined by computing the centers of the imaged laser reflections on each scanline. Thus, the errors in determining the centers correspond to errors in range that vary along the projections of the scanlines onto the laser sheet. Notice that the divergence of the laser sheet need not coincide with the divergence of the projected scanlines.

5.3 A probabilistic model

Before applying a statistical method to estimate the best manifold corresponding to a set of range images, we first need to define a probabilistic model that describes the likelihood of any possible manifold. To this end, we seek the probability distribution function (pdf):

$$\text{pdf}(f \mid \hat{f}_1, \dots, \hat{f}_p)$$

where f is a possible manifold approximating the range images $\{\hat{f}_i\}$. In order to make the analysis feasible, we make some assumptions about the nature of this pdf. At the end of this chapter, we will discuss the validity of these assumptions. First, we assume that the uncertainties in the range images are independent of one another, giving us:

$$\text{pdf}(f \mid \hat{f}_1, \dots, \hat{f}_p) = \prod_{i=1}^p \text{pdf}(f \mid \hat{f}_i) \quad (5.1)$$

Next, we assume that sample errors within a range image are independently distributed:

$$\text{pdf}(f \mid \hat{f}_i) = \prod_{j=1}^m \prod_{k=1}^m \text{pdf}(f \mid \hat{f}_i(j, k))$$

where the range images are of dimension $m \times m$. This independence assumption also requires that the registration of the range images is very accurate. Further, if we consider the sampling errors to be distributed along the lines of sight of the sensor, then:

$$\text{pdf}(f \mid \hat{f}_i) = \prod_{j=1}^m \prod_{k=1}^m \text{pdf}(f_i(j, k) \mid \hat{f}_i(j, k)) \quad (5.2)$$

where $f_i(j, k)$ is the reparameterization of f over the domain of the i 'th range image, re-sampled along the sensor direction at (j, k) . Combining Equations 5.1 and 5.2, we have:

$$\text{pdf}(f \mid \hat{f}_1, \dots, \hat{f}_p) = \prod_{i=1}^p \prod_{j=1}^m \prod_{k=1}^m \text{pdf}(f_i(j, k) \mid \hat{f}_i(j, k)) \quad (5.3)$$

Choosing a single function that “best” approximates the range surfaces takes us from the realm of probability into the realm of statistics.

5.4 Maximum likelihood estimation

One of the most common statistical methods for estimating parameters is the method of Maximum Likelihood (ML), which chooses the parameter values that maximize a pdf [Papoulis 1991]. In our case, we seek the surface function, f , that maximizes the pdf described in Equation 5.3. Note that maximizing the pdf is equivalent to minimizing $-\log(\text{pdf})$, due to the strictly monotonic nature of the logarithm function. Thus, we can transform our problem to solving for the f that minimizes:

$$E(f) = - \sum_{i=1}^p \sum_{j=1}^m \sum_{k=1}^m \log [\text{pdf}(f_i(j, k) \mid \hat{f}_i(j, k))]$$

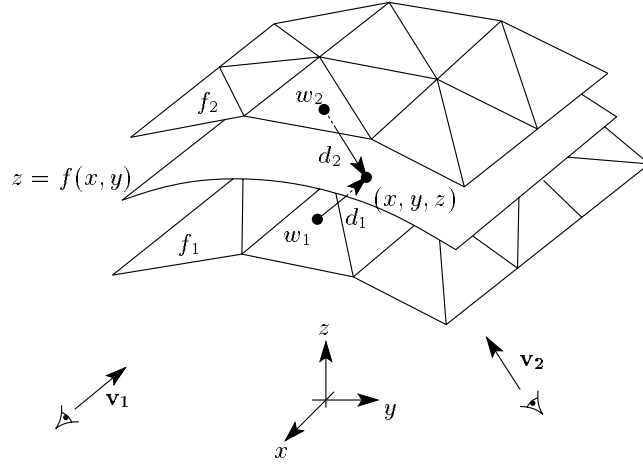


Figure 5.4: Two range surfaces, f_1 and f_2 , are tessellated range images acquired from directions v_1 and v_2 . In the case of Gaussian statistics, the possible range surface, $z = f(x, y)$, is evaluated in terms of the weighted squared distances to points on the range surfaces taken along the lines of sight to the sensor. A point, (x, y, z) , is shown here being evaluated to find its corresponding signed distances, d_1 and d_2 , and weights, w_1 and w_2 .

A difficulty with this formulation, however, is the fact that the function f need only minimize the function $E(f)$ for the points that project onto the surface for each sampled range image. In between these points, the surface need not even be continuous. In fact, the ML estimate of f would simply be the original points in the range images. Even if we required continuity, the function f could simply interpolate the points in the range images and be almost arbitrarily ill-behaved between points. To remedy this problem, we could impose some continuity and smoothness constraints on the function f . Alternatively, we can interpret the range images as range surfaces; i.e., by suitable interpolation of the range images, we can generate projected *surface* estimates of f . Figure 5.4 illustrates this principle. In this case, the function to minimize becomes:

$$E(f) = \sum_{i=1}^p \iint_{A_i} g(f_i(u, v), \tilde{f}_i(u, v)) du dv \quad (5.4)$$

where \tilde{f}_i is the interpolated range surface corresponding to \hat{f}_i , we have replaced $-\log[\text{pdf}(\cdot)]$ with $g(\cdot)$, and we have taken the limit of the summation to be an integral. Further, the (u, v) notation is a parameterization of the sensor's sampling rays. This parameterization could

pertain to, for example, an (x, y) parameterization in the orthographic case or a (θ, ϕ) parameterization in the perspective case.

One familiar pdf to choose is the Gaussian (normal) distribution:

$$\text{pdf}(f_i(u, v) | \tilde{f}_i(u, v)) = c_i(u, v) \exp \left[-\frac{1}{2} \left(\frac{\tilde{f}_i(u, v) - f_i(u, v)}{\sigma_i(u, v)} \right)^2 \right]$$

where c_i is the normalization factor and σ_i is the standard deviation. The numerator in the squared term is simply the distance between reconstructed range surface points and points on the candidate surface, where the distance is taken along the sensing direction:

$$d_i(u, v, f_i) = \tilde{f}_i(u, v) - f_i(u, v)$$

Substituting and evaluating $-\log(\text{pdf})$, we obtain:

$$g(f_i(u, v), \tilde{f}_i(u, v)) = \frac{1}{2} w_i(u, v) d_i(u, v, f_i)^2 - \log(c_i(u, v))$$

where we have set $w_i(u, v) = 1/\sigma_i(u, v)^2$. Neglecting the additive term that does not depend on f (and thus has no bearing on the minimization of $E(f)$ with respect to f), the error equation becomes:

$$E(f) = \frac{1}{2} \sum_{i=1}^p \iint_{A_i} w_i(u, v) d_i(u, v, f_i)^2 dudv$$

Thus, the assumption of Gaussian statistics leads to a weighted least squares minimization, where distances are taken between range surfaces and the minimizing function along range image viewing directions.

Note that the domain of integration in the previous equations depends on the viewpoint and ray distribution of the sensor. By choosing a common domain of integration, we can bring the summation under the integral and attempt to minimize $E(f)$ by applying the calculus of variations.

5.5 Unifying the domain of integration

In order to solve for the optimal surface, we would like to put the total error (Equation 5.4) in a form that resembles:

$$E(f) = \iint_A \sum_{i=1}^p e_i(x, y, f) dx dy$$

where we have chosen the domain of integration to be the $x - y$ plane over which our candidate surface, $f(x, y)$, is a function. The function $e_i(x, y, f)$ is the error associated with the point, (x, y, f) , on the surface as measured with respect to the i 'th range image.

To help see the connections we need to make, we can rewrite Equation 5.4 as:

$$E(f) = \sum_{i=1}^p \iint_{A_i} g_i(u, v, f_i) du dv$$

where we define g_i to be:

$$g_i(u, v, f_i) \equiv g(f_i(u, v), \tilde{f}_i(u, v))$$

Our goal then is to find a relationship between e_i and g_i through their respective domains:

$$e_i(x, y, f) dx dy \overset{?}{\longleftrightarrow} g_i(u, v, f_i) du dv$$

In fact, part of the connection is already made, because e_i and g_i are simply reparameterizations of one another; e_i is the error at a point, (x, y, f) , on the surface, and g_i is the error at the same point, expressed in the coordinates of the sensor, (u, v, f_i) .

The differentials $dx dy$ and $du dv$ are generally related to one another through the Jacobian. However, rather than compute the Jacobian directly, we prefer to derive the relationship between the differentials explicitly using geometric arguments. The intuitions gained help in generalizing from the simplest case, orthographic projection, to more arbitrary viewing frustums such as line perspective. Thus, we will first consider the case of an orthographic sensor.

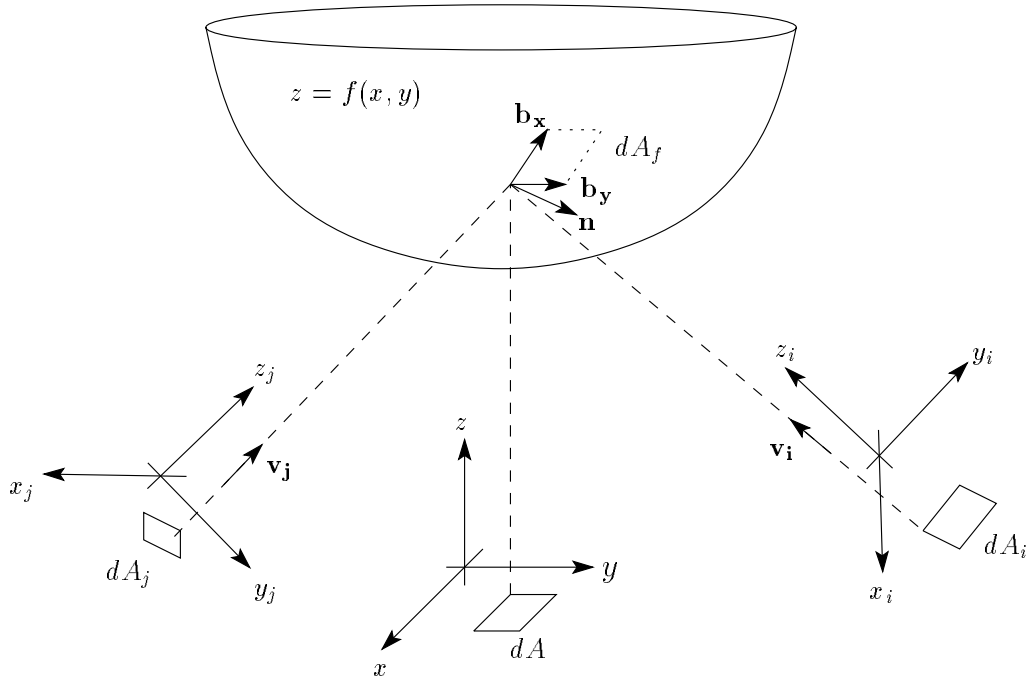


Figure 5.5: Differential area relations for reparameterization. Orthographic range images are acquired from different viewpoints, yielding surface parameterizations over domains such as (x_i, y_i) and (x_j, y_j) . Instead, we want to estimate a surface over a canonical domain (x, y) . When integrating over this canonical domain, we must relate differential areas in this domain to areas in the domains of the original range images.

For an orthographic sensor, we must project the area $dA = dx dy$ onto the function $f(x, y)$, and then re-project it onto the i 'th range image's viewing plane, as indicated in Figure 5.5. We use Cartesian (x_i, y_i, z_i) coordinates to represent (u, v, f_i) . First, we note that moving a unit distance in the x -direction in the (x, y) domain corresponds to moving along the vector \mathbf{b}_x on the surface f , where:

$$\mathbf{b}_x = \left(1, 0, \frac{\partial z}{\partial x} \right)$$

Similarly, moving in the y -direction corresponds to moving along \mathbf{b}_y on the surface:

$$\mathbf{b}_y = \left(0, 1, \frac{\partial z}{\partial y} \right)$$

If we define the vector, \mathbf{a} , as:

$$\begin{aligned}\mathbf{a} &= \mathbf{b}_y \times \mathbf{b}_x \\ &= \left(\frac{\partial z}{\partial x}, \frac{\partial z}{\partial y}, -1 \right)\end{aligned}$$

then the projected area, dA_f , on the surface is:

$$dA_f = |\mathbf{a}|dA$$

and the normal, \mathbf{n} to the surface¹ is:

$$\mathbf{n} = \frac{\mathbf{a}}{|\mathbf{a}|}$$

The projected area, $dA_i = dx_i dy_i$ on the i 'th range image plane is then:

$$\begin{aligned}dA_i &= (-\mathbf{n} \cdot \mathbf{v}_i)dA_f \\ &= -\left(\frac{\mathbf{a}}{|\mathbf{a}|} \cdot \mathbf{v}_i \right) |\mathbf{a}|dA \\ &= -(\mathbf{a} \cdot \mathbf{v}_i)dA\end{aligned}$$

This leads us to a reformulation of the equation to be minimized:

$$E(f) = \iint_A \sum_{i=1}^p e_i(x, y, z) \left[\left(-\frac{\partial z}{\partial x}, -\frac{\partial z}{\partial y}, 1 \right) \cdot \mathbf{v}_i \right] dx dy \quad (5.5)$$

where we have replaced $f(x, y)$ with z on the right hand side. This equation is now ready for minimization under the calculus of variations, but it applies only to orthographic equations in this form.

How does this equation change when we handle more complex projections, such as perspective or line perspective? In these cases, we would find that the direction of projection is

¹See [Horn 1986] for a similar derivation of the normal to a surface.

not constant as in the orthographic case, but varies over space. Further, the contribution of a surface element varies not only with the orientation of the element, but also with distance from the center of projection. For example, as an element moves away from the center of projection for the perspective case, its apparent size falls off with $1/r^2$, where r is the distance from the center.

One approach to the problem might be to define a suitable projection surface that captures the variation in orientation of projection rays and onto which we can project a surface element to compute its contribution to the error integral. For example, we could define a unit sphere about the center of projection for the perspective case. The directions of projection would run radially, normal to the surface of the sphere, and we could project a surface element dA_f onto the sphere and use this area as the measure of the contribution of the element. This definition leads to the measurement dA_f in terms of the solid angle it subtends. This is exactly what we would expect, and it will yield the desired $1/r^2$ fall-off. For the line perspective, the projection surface would be a cylinder of unit radius, yielding projection rays that emanate radially from the center line, and the contribution of a surface element would fall off as $1/r$, where r is the distance from the center line.

While the use of these projection surfaces will work in a number of cases, it is too restrictive a definition and will not work in all cases. Instead, we propose an alternative and more general way of looking at these projections. Consider the two-dimensional case of a perspective projection as shown in Figure 5.6. The projection rays radiate from the center of projection. For every point in space (except the center of projection), a single ray passes through that point in a particular direction. The directions evaluated throughout space define a vector field as shown in Figure 5.6b. We could then compute the projected length of a unit line element by dotting the normal of the element with the projection direction at the center of the element.

The direction field alone, however, does not tell us the contribution the element would have to an integral over all directions in the projection. This contribution should be a measure of how many rays cross the a unit line segment in the direction of projection. In our example, this “ray density” should fall of with the inverse distance from the center of projection. By weighting our direction field by the “ray density” measure, we arrive at a new

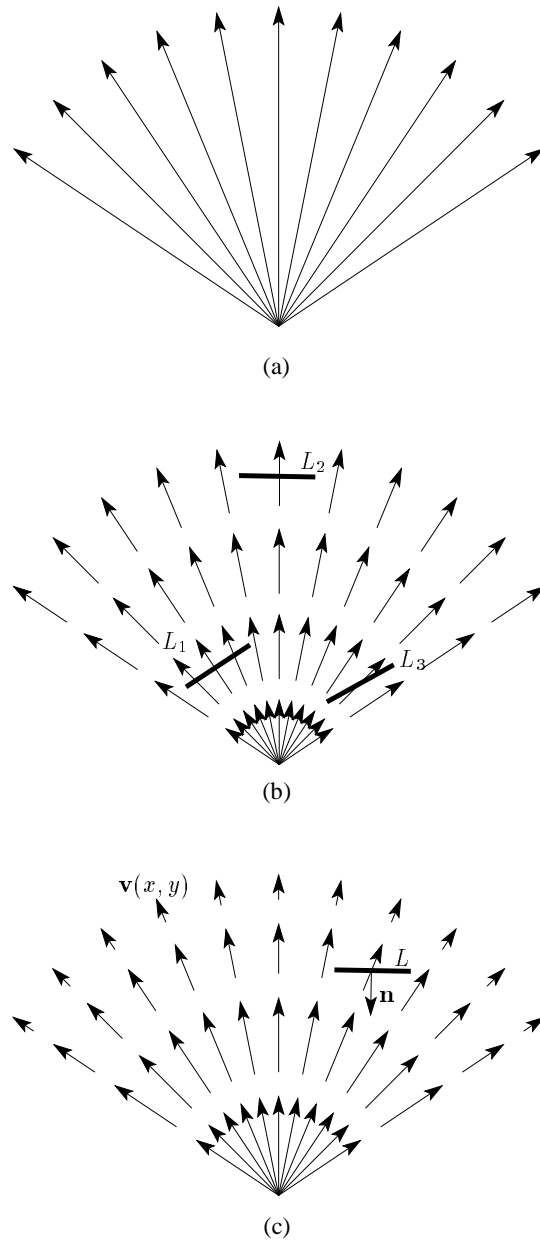


Figure 5.6: Ray density and vector fields in 2D. (a) For a perspective projection in 2D, the sensor is effectively a point source casting rays to sample space. (b) We can view this set of rays as defining a vector field, where each point in space has an associated ray direction. The contribution of elements in the field for the purposes of integration is defined by how many rays pass through the elements; element L_1 receives more rays than element L_2 , because it is closer to the sensor. It also receives more rays than L_3 , because it is more normal to the ray direction. (c) To encode the variations in ray density, we multiply the direction field in (b) by the ray density. Now the contribution of an element is $|L|\mathbf{n} \cdot \mathbf{v}(x, y)$.

vector field, depicted in Figure 5.6c. For a unit line segment, dotting the normal of the segment with the strength of this vector field will yield the total contribution of the element.

This “ray density” field has a familiar physical interpretation. If we think of the center of projection as being a point source sending equal amounts of particles in all directions, then the “ray density” field is the vector flow field describing the direction and rate of particle flow across unit projected lengths. If we think of these particles as photons, we arrive at a description of the light field about the point source, and we can measure the contribution of a surface as the amount of light that flows through the element. We assume the projections are one-to-one, so the light fields will have a single flow direction at every point.

One of the most important elements of this physical analogy, is the fact that the projection rays emanate from the sensor, but they flow forever without being extinguished or created anew in space. In other words, this flow field is *conservative* at all points outside of the regions where the rays originate. Further, the projection rays are fixed for each range scan; i.e., the flow field is *static*. These conservative and static properties will prove very useful in the next section.

In general, any range imaging frustum will define a vector field whose directions are consistent with the projection rays and whose magnitude is equal to the flux of rays crossing a unit projected area. For the case of an orthographic projection, this vector field is simply a unit vector in the direction of projection:

$$\mathbf{v}(x, y, z) = \hat{\mathbf{v}}$$

A perspective projection yields a radial field with $1/r^2$ fall-off:

$$\mathbf{v}(r, \theta, \phi) = \frac{\hat{\mathbf{r}}}{r^2}$$

where $\hat{\mathbf{r}} = \mathbf{r}/|\mathbf{r}|$.

The line perspective results in a cylindrically radial field with $1/r$ fall-off:

$$\mathbf{v}(r, \theta, x) = \frac{\hat{\mathbf{r}}}{r}$$

In the latter two cases, we have expressed the vector fields in spherical and cylindrical coordinates, but they are all equivalently expressible in Cartesian coordinates.

With this new vector flow field analogy, we can now express the relation between $dA = dx dy$ and the ray differential $dA_i = du_i dv_i$ as:

$$dA_i = \left(-\frac{\partial z}{\partial x}, -\frac{\partial z}{\partial y}, 1 \right) \cdot \mathbf{v}_i(x, y, z) dA$$

Similarly, the error equation becomes:

$$E(f) = \iint_A \sum_{i=1}^p e_i(x, y, z) \left[\left(-\frac{\partial z}{\partial x}, -\frac{\partial z}{\partial y}, 1 \right) \cdot \mathbf{v}_i(x, y, z) \right] dx dy \quad (5.6)$$

This equation is almost identical to Equation 5.5, except that the constant vector \mathbf{v}_i has been replaced with a vector field $\mathbf{v}_i(x, y, z)$. For the special case of Gaussian statistics, this integral becomes:

$$E(f) = \iint_A \sum_{i=1}^p w_i(x, y, z) d_i(x, y, z)^2 \left[\left(-\frac{\partial z}{\partial x}, -\frac{\partial z}{\partial y}, 1 \right) \cdot \mathbf{v}_i(x, y, z) \right] dx dy \quad (5.7)$$

Note how the integration over a common domain brings the summation under the integral. This new formulation allows us to apply the calculus of variations to find the $z = f(x, y)$ that minimizes the integral.

5.6 Calculus of variations

One of the primary objectives of the calculus of variations is to take an integral of the form:

$$I = \iiint h \left(x, y, z, \frac{\partial z}{\partial x}, \frac{\partial z}{\partial y} \right) dx dy dz$$

and compute the function:

$$z = f(x, y)$$

that minimizes the integral. A central result of the calculus of variations states that the minimizing function must obey a partial differential equation known as the Euler-Lagrange equation [Weinstock 1974]:

$$\frac{\partial h}{\partial z} - \frac{\partial}{\partial x} \frac{\partial h}{\partial(\partial z/\partial x)} - \frac{\partial}{\partial y} \frac{\partial h}{\partial(\partial z/\partial y)} = 0$$

We can easily extend this result to the case of minimizing integrals of sums of functions:

$$I = \iiint \sum_{i=1}^p h_i \left(x, y, z, \frac{\partial z}{\partial x}, \frac{\partial z}{\partial y} \right) dx dy dz$$

Substituting into the Euler-Lagrange equation, we get:

$$\frac{\partial \sum_{i=1}^p h_i}{\partial z} - \frac{\partial}{\partial x} \frac{\partial \sum_{i=1}^p h_i}{\partial(\partial z/\partial x)} - \frac{\partial}{\partial y} \frac{\partial \sum_{i=1}^p h_i}{\partial(\partial z/\partial y)} = 0$$

and from the linearity of partial differentiation, we arrive at the result:

$$\sum_{i=1}^p \left[\frac{\partial h_i}{\partial z} - \frac{\partial}{\partial x} \frac{\partial h_i}{\partial(\partial z/\partial x)} - \frac{\partial}{\partial y} \frac{\partial h_i}{\partial(\partial z/\partial y)} \right] = 0$$

In order to solve an equation such as Equation 5.6 described in the previous section, we must first propose the following theorem.

Theorem 5.1 *Given the integral:*

$$I = \iiint h \left(x, y, z, \frac{\partial z}{\partial x}, \frac{\partial z}{\partial y} \right) dx dy dz$$

where:

$$z = f(x, y)$$

and the function h is of the form:

$$h \left(x, y, z, \frac{\partial z}{\partial x}, \frac{\partial z}{\partial y} \right) = e(x, y, z) \left[\left(-\frac{\partial z}{\partial x}, -\frac{\partial z}{\partial y}, 1 \right) \cdot \mathbf{v}(x, y, z) \right]$$

the function z that minimizes the integral satisfies the relation:

$$\mathbf{v} \cdot \nabla e + e \nabla \cdot \mathbf{v} = 0 \quad (5.8)$$

See Appendix A for the proof. Under the conditions that $\mathbf{v}(x, y, z)$ corresponds to a static, conservative flow field, then the following corollary obtains:

Corollary 5.1 *Given the integral:*

$$I = \iiint h \left(x, y, z, \frac{\partial z}{\partial x}, \frac{\partial z}{\partial y} \right) dx dy dz$$

where:

$$z = f(x, y)$$

and the function h is of the form:

$$h \left(x, y, z, \frac{\partial z}{\partial x}, \frac{\partial z}{\partial y} \right) = e(x, y, z) \left[\left(-\frac{\partial z}{\partial x}, -\frac{\partial z}{\partial y}, 1 \right) \cdot \mathbf{v}(x, y, z) \right]$$

where $\mathbf{v}(x, y, z)$ corresponds to a conservative and static vector flow field, then the function z that minimizes the integral satisfies the relation:

$$\mathbf{v} \cdot \nabla e = 0 \quad (5.9)$$

The proof is straightforward: the divergence of a conservative vector flow field ($\nabla \cdot \mathbf{v}$) must be exactly zero if the field is not changing with time [Schey 1992]. Thus, the result of Theorem 5.1 is simplified by removing the divergence term.

Corollary 5.1 has an intuitive interpretation. Consider minimizing the same integral for a constant vector field (corresponding to an orthographic projection) oriented in the $+z$ direction. The integrand would become $h = e(x, y, z)$ and would not depend on any partials of z . In this case, the obvious solution would be to minimize with respect to z only; i.e., compute:

$$\frac{\partial e}{\partial z} = 0$$

The only reason h becomes dependent on partials in the theorem, is so that we can solve the problem over a new domain, rotated with respect to the original domain (for the orthographic case). The solution in this new domain is actually the same; we take the derivative along the direction in which the function can vary. We can see this by noting that the dot product in Equation 5.9 is equivalent to a directional derivative taken along the line of sight for the original domain.

In order to solve the minimization equation posed in the previous section (Equation 5.6), we need to extend Theorem 5.1 to minimization over sums of functions. This leads to the following corollary:

Corollary 5.2 *Given the integral:*

$$I = \iiint h \left(x, y, z, \frac{\partial z}{\partial x}, \frac{\partial z}{\partial y} \right) dx dy dz$$

where:

$$z = f(x, y)$$

and the function h is of the form:

$$h \left(x, y, z, \frac{\partial z}{\partial x}, \frac{\partial z}{\partial y} \right) = \sum_{i=1}^n e_i(x, y, z) \left[\left(-\frac{\partial z}{\partial x}, -\frac{\partial z}{\partial y}, 1 \right) \cdot \mathbf{v}_i(x, y, z) \right]$$

where the $\mathbf{v}_i(x, y, z)$ correspond to conservative and static vector flow fields, then the function z that minimizes the integral satisfies the relation:

$$\sum_{i=1}^p \mathbf{v}_i \cdot \nabla e_i = 0$$

The proof is a straightforward application of the linearity of the Euler-Lagrange equation

in combination with Corollary 5.1.

5.7 A minimization solution

We can now derive an equation for the function $z = f(x, y)$ that minimizes Equation 5.6. Namely, z must satisfy the relation:

$$\sum_{i=1}^p \mathbf{v}_i(x, y, z) \cdot \nabla e_i(x, y, z) = 0$$

Noting that a unit vector dotted with the gradient of a function is the same as taking the derivative in the direction of that vector, we can re-write the equation as:

$$\sum_{i=1}^p |\mathbf{v}_i| D_{\hat{\mathbf{v}}_i} [e_i] = 0$$

where $D_{\hat{\mathbf{v}}_i}$ represents the derivative in the direction of the sensor line of sight, $\hat{\mathbf{v}}_i$, and we have dropped the (x, y, z) notation.

Consider the case where e_i corresponds to the $-\log(\text{pdf})$ with Gaussian statistics. The solution equation is then:

$$\sum_{i=1}^p |\mathbf{v}_i| D_{\hat{\mathbf{v}}_i} [w_i d_i^2] = 0$$

To simplify this relation, we note that the weighting function varies across the range image, but not along the sensor lines of sight. Accordingly:

$$D_{\hat{\mathbf{v}}_i} [w_i d_i^2] = 2w_i d_i D_{\hat{\mathbf{v}}_i} [d_i]$$

Next, we note that the distance from the range surface is a linear function of constant slope along the viewing direction:

$$D_{\hat{\mathbf{v}}_i} [d_i] = 1$$

Putting these results together, we obtain:

$$\sum_{i=1}^p |\mathbf{v}_i| w_i d_i = 0 \quad (5.10)$$

Thus, we arrive at a surprisingly simple result: the weighted least squares surface is determined by the zero-isosurface of the sums of the weighted signed distance functions.

In the orthographic case, the value of $|\mathbf{v}_i|$ is unity, so the minimization equation reduces to:

$$\sum_{i=1}^p w_i d_i = 0$$

while for the perspective case, we arrive at:

$$\sum_{i=1}^p \frac{w_i d_i}{r_i^2} = 0$$

where the center of projection of the i 'th range image is at (x_i^c, y_i^c, z_i^c) , and:

$$r_i = \sqrt{(x - x_i^c)^2 + (y - y_i^c)^2 + (z - z_i^c)^2}$$

Note the distinction here between d_i and r_i : d_i is the distance from a point in 3-space to the i th range image along the sensor's line of sight, while r_i is the distance from the same point to the center of projection of the sensor.

5.8 Discussion

We have shown that, under a set of assumptions, the surface of Maximum Likelihood derived from a set of range images can be found as a zero isosurface of a function over 3-space. The function defined in this domain is a sum of functions generated by each range image, and thus may be updated one range image at a time. For the case of a weighted least squares minimization, the optimal surface is the zero isosurface of the sum of the weighted signed distances along the lines of sight of the range images. Here we review the assumptions and evaluate the validity of each.

All range image samples are statistically independent. Each range image is likely to have little dependence on the other range images, since they are taken as separate events. However, whether or not samples *within* a range image exhibit independence depends on the range scanning device. Consider a scanner that projects an illuminant on one part of the surface, records the range, and moves the illuminant to the next sample position. If the illuminant projected onto the surface does not overlap with adjacent samples, then we would expect there to be no statistical correlation among samples. On the other hand, if the illuminant does overlap at different positions, then we might expect some correlations. For a well designed scanner, the illuminant is usually quite narrow, and/or the sensor lines of sight have little overlap (held tightly in focus), so that any dependence among samples is highly local, restricted to nearby samples. In this case, we can regard the assumption of statistical independence as an approximation to the more exact solution that accounts for local sample interdependence. Still, scanners are likely to have some element of uncertainty that *is* independent among samples. Thermal noise in electronic circuitry, for example, will exist regardless of the proximity of samples, leading to some independent range errors.

Range uncertainties are purely directional and are aligned along the lines of sight of the sensor which are known to high accuracy. To some extent, this statement may seem to be a tautology; we have defined a range imaging sensor as a device that returns depth values along specified lines of sight. When the sensor errs, it returns an erroneous *depth*, which must be along the line of sight of the sensor. In the previous chapters, we discussed the errors in optical triangulation, and these errors manifested themselves along either the lines of sight of the illuminant or the imaging device, depending what kind of analysis was used in determining depth. However, a sensor may also have some uncertainty in its lines of sight. For example, when performing traditional optical triangulation, if a sweeping illuminant has some “wobble” in its path, then its lines of sight may not be consistent. This inconsistency would lead to errors in depth along the line of sight, as well as errors that vary side to side, perpendicular to the line of sight. The error might then take an elliptical form, rather than a purely directional form. Nonetheless, the devices that control motion can be very precise, and sensors such as CCD’s have been shown to exhibit excellent geometric stability. As a result, range imaging sensors can be designed to have excellent accuracy in the lines of sight, leaving depth uncertainty as the dominant error in the system.

Errors in alignment are much smaller than errors in range samples. The problem of aligning range images has received a fair amount of attention, and the results indicate that a number of algorithms can achieve accurate alignment among pairs of range images [Gagnon et al. 1994] [Turk & Levoy 1994]. Figure 5.7 shows the results of performing alignment with one of these pairwise methods. The problem of aligning a set of range images simultaneously, however, requires new alignment algorithms. Consider a set of range images taken from 8 points on the compass around an object. By aligning the range images in a pairwise fashion, we can walk around the object. But by the time we have come full circle, we find that the alignment errors have accumulated, and the first and last range images are now significantly misaligned. A better approach is to define an error function that relates all range images to one another, and then minimize this function all at once. Only recently are solutions to this total alignment problem emerging [Bergevin et al. 1996] [Stoddart & Hilton 1996]. Nonetheless, through a combination of good initial alignment and some heuristics for choosing how to perform the pairwise alignments, researchers have demonstrated that it is still possible to obtain reasonably accurate results. Our results, which we discuss in Chapter 8, show that the average distance between range samples and their projections onto the reconstructed surface are roughly the same as the uncertainty in the individual samples. This fact indicates that range errors dominate the alignment errors.

The range images yield viable range surfaces. While many range scanners generate a dense grid of depth samples, the analysis in this chapter requires the use of (piecewise) continuous surfaces. As described earlier, we can use the depth samples to reconstruct the desired range surfaces. In the case of the spacetime analysis described in the previous chapters, continuous reconstruction of the spacetime volume can indeed lead directly to range surfaces². If the surface being sampled is smooth relative to the sampling rate, then the resulting range surface will be a reasonable estimate of the object's shape. However, the apparent smoothness of a surface, changes with viewing direction. A surface viewed at a grazing angle will be sampled far less than a surface that is facing the sensor. The grazing angle surface may even be undersampled, yielding a questionable, possibly aliased reconstruction. To ameliorate this problem, researchers avoid reconstructing the range surface

²In practice, we perform the reconstruction at a fixed resolution, leading to range images that still must be converted to range surfaces.

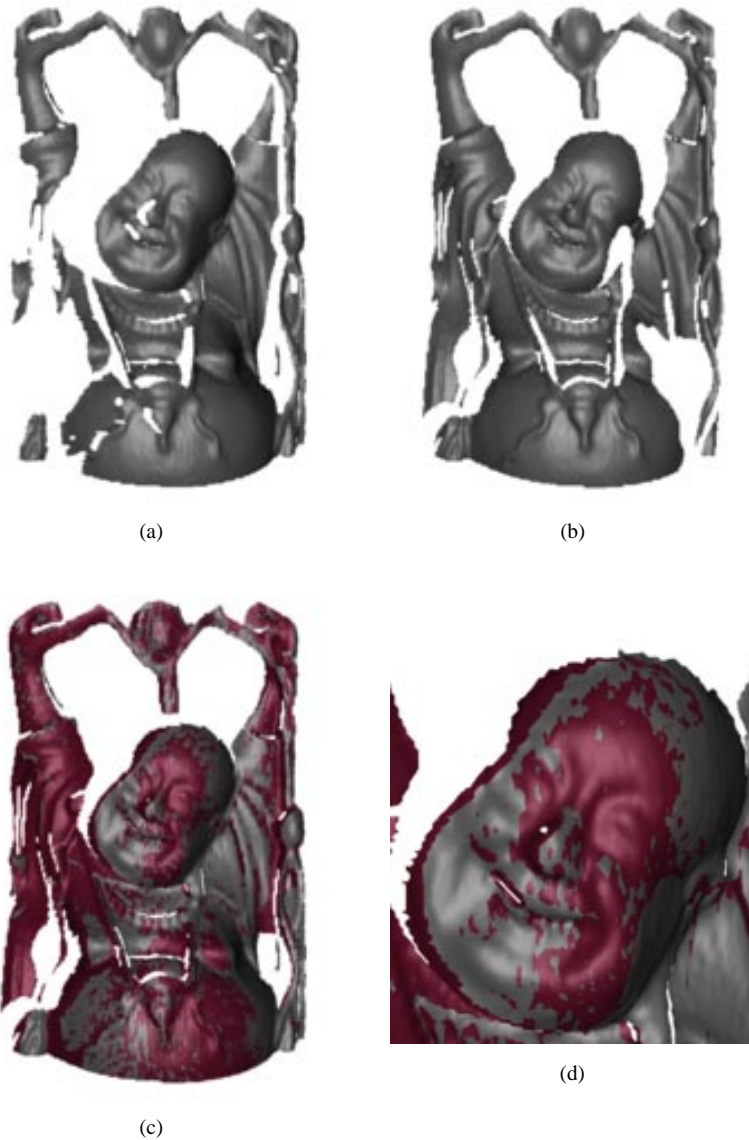


Figure 5.7: Aligned range images. Two range images were taken 30 degrees apart with an optical triangulation scanner. (a) and (b) show the corresponding range surfaces. (c) shows a rendering of the two range surfaces after alignment; the surface from (b) is rendered with a darker (red) color. (d) shows a “blow-up” of the head of the model. Note that the range surfaces are so close as to be inter-penetrating across the surface. The RMS error in distances between nearest points on the two surfaces is on the order of the error in individual range samples, indicating that the majority of the uncertainty remains in sampling error rather than alignment. Note that in some areas of overlap in (c) and (d), one surface is in front of the other in large regions, suggesting correlated range errors. However, these regions are significantly larger than the neighborhoods spanned by the illumination of the range scanner, making it unlikely that correlation in range errors is the cause. We suspect these coherent overlap areas result from small miscalibrations in the range scanner.

in areas that are known to be at sufficiently grazing angles and downweight contributions from surfaces that are at moderately grazing angles. For example, when using the Gaussian model with weighted signed distances, we can lower the weights in accordance with the orientation of the surface with respect to the sensor. While this is not strictly consistent with the notion of variance in Gaussian statistics, it yields excellent results in practice, as we will show in the following chapters.

In addition, points on the range surface that do not coincide with range samples will not appear to be statistically independent, even if the range samples are. Consider a 2D world where our sensor has acquired two neighboring range samples. We can reconstruct the range surface by linearly interpolating between the two samples, i.e., by connecting them with a line segment. We may regard the two samples as statistically independent, but the points on the line segment adjoining them clearly depends on the original samples. While this is not consistent with the assumption that points on the range surfaces are statistically independent, the results do indicate that regarding them as independent is a reasonable approximation.

The range images are functions over the domain where a surface is sought. When computing the ML optimal surface, we assume that each range image is sampling the same surface from different points of view. However, an object is generally not a single-valued function with respect to any single point of view. If we trace a ray from the sensor and intersect it with the object, we will see the nearest point on the “front” side of the object, but if we imagine continuing the ray beyond the first intersection, it will eventually intersect the “back” side of the object. Two different range images will sample the front and back sides of the object, and clearly they are not seeing the same points. Care must be taken so that when determining the optimal surface, we do not presume that these two range images are measuring the same surface. In the next chapter, we discuss efforts to make sure that opposing surfaces are not treated as the same surface.

In the case of the least squares formulation, the range uncertainties obey Gaussian statistics. The development in the previous sections is suited to any statistical model for directional range uncertainty. Nonetheless, Gaussian statistics are appealing because of their simplicity; in our case, they lead to signed distance functionals. When might this apply? In some scanners, individual samples are too noisy, so the sampling is repeated along a single

line of sight, and the results are averaged. Almost regardless of the statistics of the errors in the individual samples, averaging them together tends to make the statistics take on a Gaussian character. Indeed, the central limit theorem tells us that the distribution does indeed become “more Gaussian” with each additional sample included in the average. In addition, our studies of errors due to laser speckle in optical triangulation indicate that the error distributions actually do have a Gaussian appearance, as indicated by Figure 4.13.

Chapter 6

A New Volumetric Approach

The discussion in the previous chapter provides a mathematical framework for merging range images. In this chapter, we begin with a description of how we can implement this framework on a volumetric grid (Section 6.1). Then, we extend the framework to represent knowledge about the emptiness of space around an object (Section 6.2). This additional knowledge leads to a simple algorithm for filling gaps in the reconstruction where no surfaces have been observed. In Section 6.3, we analyze sampling and filtering issues that arise from working with a sampled representation. Finally, we discuss the limitations of the volumetric method described in this chapter and offer some possible solutions (Section 6.4).

6.1 Merging observed surfaces

Our algorithm employs a continuous implicit function, $D(\mathbf{x})$, represented by samples. The function we represent is the weighted signed distance of each point \mathbf{x} to the nearest range surface along the line of sight to the sensor. We construct this function by combining signed distance functions $d_1(\mathbf{x}), d_2(\mathbf{x}), \dots, d_p(\mathbf{x})$ and weight functions $w_1(\mathbf{x}), w_2(\mathbf{x}), \dots, w_p(\mathbf{x})$ obtained from range images 1 ... n . Our combining rules give us for each voxel a cumulative signed distance function, $D(\mathbf{x})$, and a cumulative weight $W(\mathbf{x})$. We represent these functions on a discrete voxel grid and extract an isosurface corresponding to $D(\mathbf{x}) = 0$. As shown in the previous chapter, this isosurface is optimal in the least squares sense.

Figure 6.1 illustrates the principle of combining unweighted signed distances for the

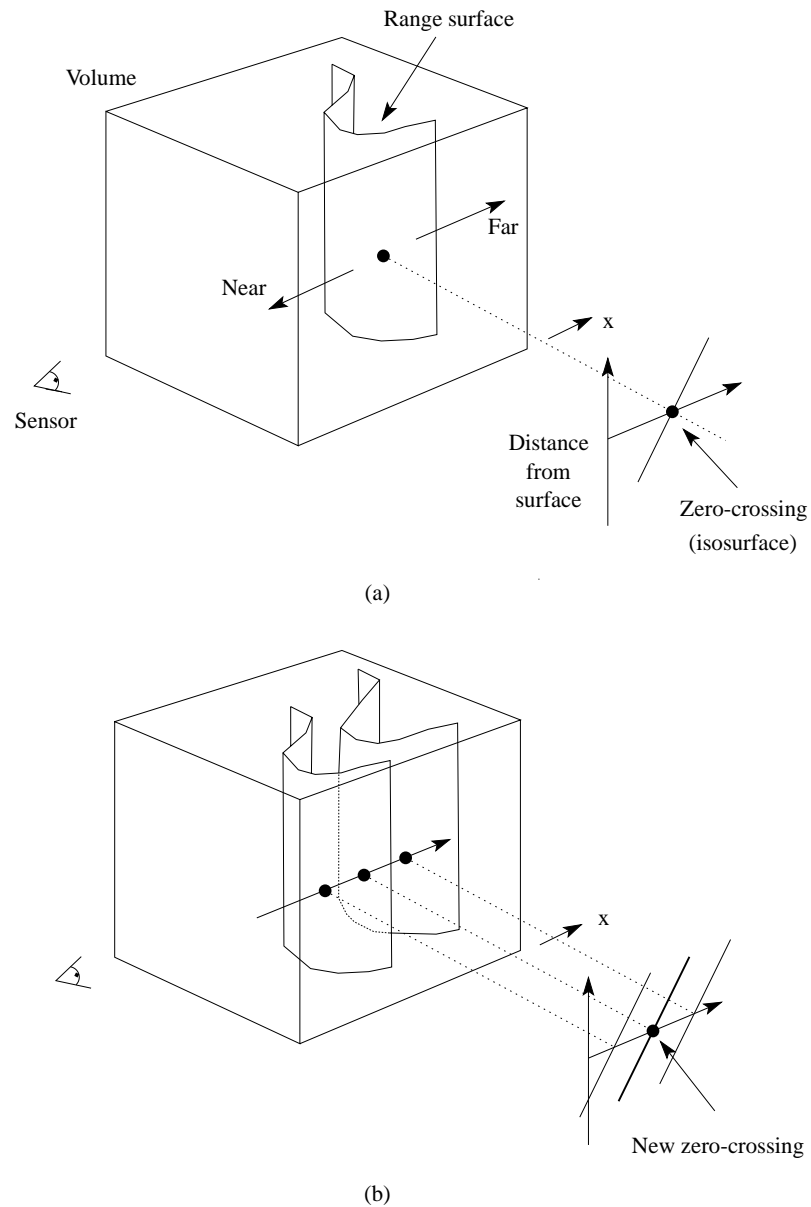


Figure 6.1: Unweighted signed distance functions in 3D. (a) A range sensor looking down the x -axis observes a range image, shown here as a reconstructed range surface. Following one line of sight down the x -axis, we can generate a signed distance function as shown. The zero crossing of this function is a point on the range surface. (b) The range sensor repeats the measurement, but noise in the range sensing process results in a slightly different range surface. In general, the second surface would interpenetrate the first, but we have shown it as an offset from the first surface for purposes of illustration. Following the same line of sight as before, we obtain another signed distance function. By summing these functions, we arrive at a cumulative function with a new zero crossing positioned midway between the original range measurements.

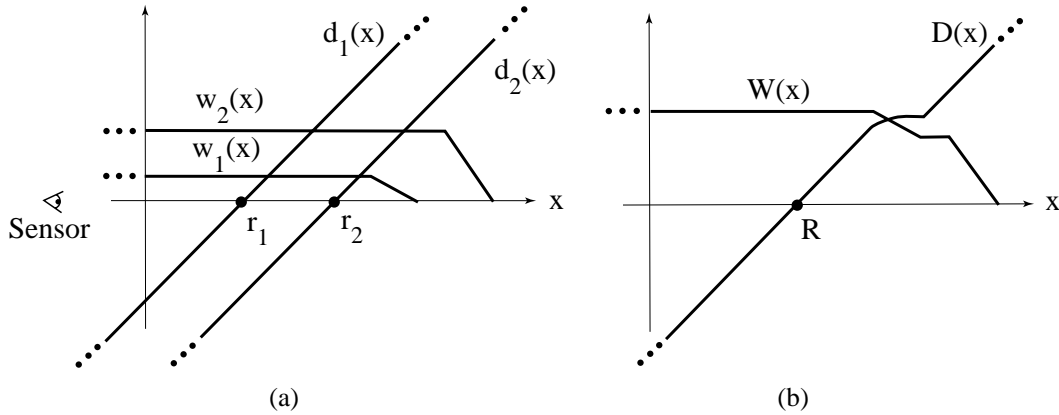


Figure 6.2: Signed distance and weight functions in one dimension. (a) The sensor looks down the x -axis and takes two measurements, r_1 and r_2 . $d_1(x)$ and $d_2(x)$ are the signed distance profiles, and $w_1(x)$ and $w_2(x)$ are the weight functions. In 1D, we might expect two sensor measurements to have the same weight magnitudes, but we have shown them to be of different magnitude here to illustrate how the profiles combine in the general case. (b) $D(x)$ is a weighted combination of $d_1(x)$ and $d_2(x)$, and $W(x)$ is the sum of the weight functions. Given this formulation, the zero-crossing, R , becomes the weighted combination of r_1 and r_2 and represents our best guess of the location of the surface. In practice, we truncate the distance ramps and weights to the vicinity of the range points.

simple case of two range surfaces sampled from the same direction. Note that the resulting isosurface would be the surface created by averaging the two range surfaces along the sensor's lines of sight. In general, however, weights will vary across the range surfaces.

6.1.1 A one-dimensional Example

Figure 6.2 illustrates the construction and usage of the signed distance and weight functions in one dimension. In Figure 6.2a, the sensor is positioned at the origin looking down the $+x$ axis and has taken two measurements, r_1 and r_2 . The signed distance profiles, $d_1(x)$ and $d_2(x)$ may extend indefinitely in either direction, but the weight functions, $w_1(x)$ and $w_2(x)$, taper off behind the range points for reasons discussed below.

Figure 6.2b is the weighted combination of the two profiles. The combination rules are straightforward:

$$D(\mathbf{x}) = \frac{\sum w_i(\mathbf{x})d_i(\mathbf{x})}{\sum w_i(\mathbf{x})} \quad (6.1)$$

$$W(\mathbf{x}) = \Sigma w_i(\mathbf{x}) \quad (6.2)$$

where, $d_i(\mathbf{x})$ and $w_i(\mathbf{x})$ are the signed distance and weight functions from the i th range image. Note that setting $D(\mathbf{x}) = 0$ and solving for \mathbf{x} is equivalent to the least squares solution described in the previous chapter. Equation 6.1 differs from Equation 5.10 in that the former is normalized by the sum of the weights. Since the sum of the weights is always positive, the equations yield the same isosurface. In practice, we have observed that the normalization serves to equalize the gradient of the sampled field, $D(\mathbf{x})$, and thereby reduces artifacts in the isosurface algorithms, which are sensitive to sudden changes in the gradient. We discuss the benefits of using weighted averages in greater detail in Section 6.3.2.

Expressed as an incremental calculation, the signed distance and weight combination rules are:

$$D_{i+1}(\mathbf{x}) = \frac{W_i(\mathbf{x})D_i(\mathbf{x}) + w_{i+1}(\mathbf{x})d_{i+1}(\mathbf{x})}{W_i(\mathbf{x}) + w_{i+1}(\mathbf{x})} \quad (6.3)$$

$$W_{i+1}(\mathbf{x}) = W_i(\mathbf{x}) + w_{i+1}(\mathbf{x}) \quad (6.4)$$

where $D_i(\mathbf{x})$ and $W_i(\mathbf{x})$ are the cumulative signed distance and weight functions after integrating the i th range image.

In the special case of one dimension, the zero-crossing of the cumulative function is at a range, R given by:

$$R = \frac{\Sigma w_i r_i}{\Sigma w_i} \quad (6.5)$$

i.e., a weighted combination of the acquired range values, which is what one would expect for a least squares minimization.

6.1.2 Restriction to vicinity of surface

In principle, the distance and weighting functions should extend indefinitely in either direction. However, to prevent surfaces on opposite sides of the object from interfering with each other, we force the weighting function to taper off behind the surface. There is a trade-off involved in choosing where the weight function tapers off. It should persist far enough behind the surface to ensure that all distance ramps will contribute in the vicinity of the final zero crossing, but, it should also be as narrow as possible to avoid influencing surfaces on the other side. To meet these requirements, we force the weights to fall off at a distance equal to half the maximum uncertainty interval of the range measurements. Similarly, the signed distance and weight functions need not extend far in front of the surface. Restricting the functions to the vicinity of the surface also yields a more compact representation and reduces the computational expense of updating the volume. In Section 6.4.1, we discuss problems of interfering signed distance ramps in greater detail.

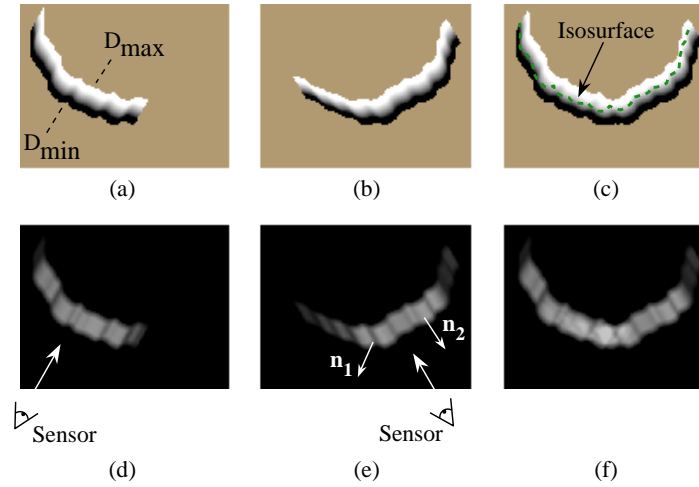


Figure 6.3: Combination of signed distance and weight functions in two dimensions. (a) and (d) are the signed distance and weight functions, respectively, generated for a range image viewed from the sensor line of sight shown in (d). The signed distance functions are chosen to vary between D_{min} and D_{max} , as shown in (a). The weighting falls off with increasing obliquity to the sensor and at the boundaries of the meshes as indicated by the darker regions in (e). The normals, \mathbf{n}_1 and \mathbf{n}_2 shown in (e), are oriented at a grazing angle and facing the sensor, respectively. Note how the weighting is lower (darker) for the grazing normal. (b) and (e) are the signed distance and weight functions for a range image of the same object taken at a 60 degree rotation. (c) is the signed distance function $D(\mathbf{x})$ corresponding to the per voxel weighted combination of (a) and (b) constructed using Equations 6.3 and 6.4. (f) is the sum of the weights at each voxel, $W(\mathbf{x})$. The dotted green curve in (c) is the isosurface that represents our current estimate of the shape of the object.

6.1.3 Two and three dimensions

In two and three dimensions, the range measurements correspond to curves or surfaces with weight functions, and the signed distance ramps have directions that are consistent with the primary directions of sensor uncertainty. Figure 6.3 illustrates the two-dimensional case for a range curve derived from a single scan containing a row of range samples. In practice, we use a fixed point representation for the signed distance function, which bounds the values to lie between D_{min} and D_{max} as shown in the figure. The values of D_{min} and D_{max} must be negative and positive, respectively, as they are on opposite sides of a signed distance zero-crossing.

For three dimensions, we can summarize the whole algorithm as shown in Figure 6.4. First, we set all voxel weights to zero, so that new data will overwrite the initial grid values.

```

/* Initialization */
For each voxel {
  Set weight = 0
}

/* Merging range images */
For each range image {

  /* Prepare range image */
  Tessellate range image
  Compute vertex weights

  /* Update voxels */
  For each voxel near the range surface {
    Find point on range surface
    Compute signed distance to point
    Interpolate weight from neighboring vertices
    Update the voxel's signed distance and weight
  }
}

/* Surface extraction */
Extract an isosurface at the zero crossing

```

Figure 6.4: Pseudocode for the method of volumetric integration.

Next, we tessellate each range image by constructing triangles from nearest neighbors on the sampled lattice. We avoid tessellating over step discontinuities (cliffs in the range map) by discarding triangles with edge lengths that exceed a threshold. We must also compute a weight at each vertex as described below.

Once a range image has been converted to a triangle mesh with a weight at each vertex, we can update the voxel grid. The signed distance contribution is computed by casting a ray from the sensor through each voxel near the range surface and then intersecting it with the triangle mesh, as shown in figure 6.5. The weight is computed by linearly interpolating the weights stored at the intersection triangle's vertices. Having determined the signed distance and weight we can apply the update formulae described in Equations 6.3 and 6.4.

At any point during the merging of the range images, we can extract the zero-crossing isosurface from the volumetric grid. Isosurface extraction algorithms have been well-explored, and a number of approaches have been demonstrated to produce tessellations without consistency artifacts [Ning & Bloomenthal 1993]. These algorithms typically decompose the volume into cubes or tetrahedra with sample values stored at the vertices, followed by interpolation of these samples to estimate locations of zero-crossings, as shown in

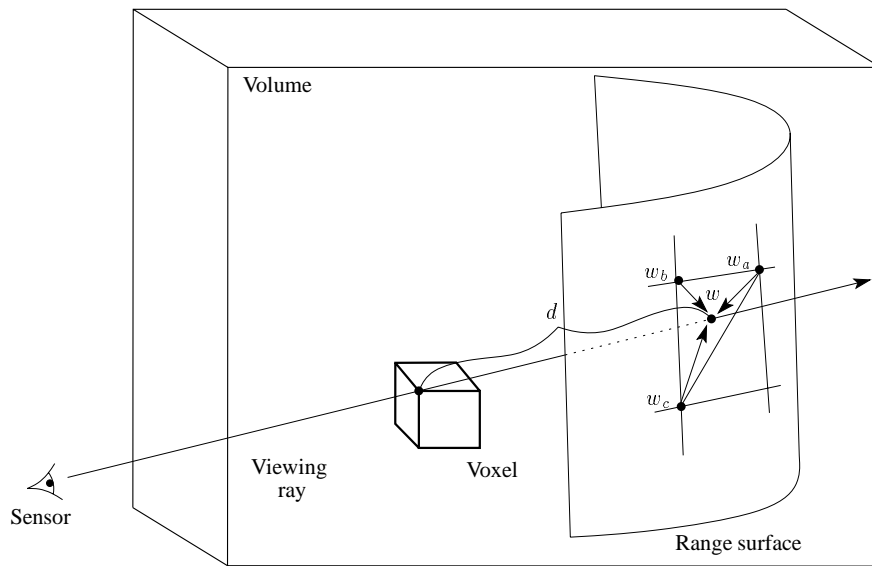


Figure 6.5: Sampling the range surface to update the volume. We compute the weight, w , and signed distance, d , needed to update the voxel by casting a ray from the sensor, through the voxel onto the range surface. We obtain the weight, w , by linearly interpolating the weights (w_a , w_b , and w_c) stored at neighboring range vertices. Note that for a translating sensor (like our Cyberware scanner), the sensor point is different for each column of range points.

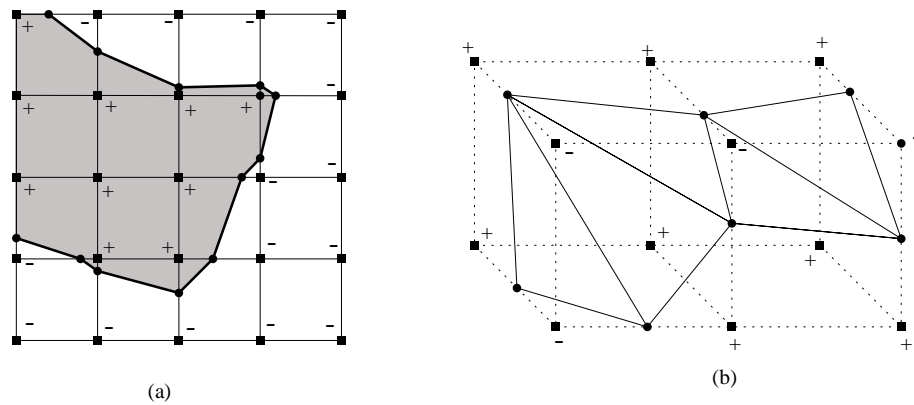


Figure 6.6: Discrete isosurface extraction. (a) In two dimensions, a typical isocontour extraction algorithm interpolates grid values to estimate isocontour crossings along lattice lines. By connecting the crossings with line segments, an isocontour is obtained. (b) In three dimensions, the crossings are connected with triangles. This method corresponds to the marching cubes algorithm described in [Lorenson & Cline 1987] with corrections in [Montani et al. 1994].

Figure 6.6. The gradients at the extracted zero-crossings provide an estimate of the surface normals¹. We restrict the extraction procedure to skip samples with zero weight, generating triangles only in the regions of observed data. We will relax this restriction in the next section.

6.1.4 Choosing surface weights

The choice of weights is theoretically a function of the uncertainties in the range data, but they can also serve the purpose of manipulating the way range surfaces are merged. As described in the previous chapter, the use of weighted signed distances corresponds to the assumption of independent Gaussian statistics along the sensor’s lines of sight. The weight then is the inverse of the squared variance of the pdf at each point on the surface. In this sense, the weight represents the degree of confidence in the data; a larger weight means that the data is more likely to be accurate.

The manner in which weights vary over a surface depend on the scanning technology. For example, in an optical triangulation system, low intensity images of the laser reflection imply a lower signal to noise ratio at the sensor, and thus lower confidence in shape estimates. [Soucy & Laurendeau 1995] and [Turk & Levoy 1994] have used this argument to justify forcing weights to depend on the dot product between the range surface normal and the laser direction, because the reflected radiance from a diffuse Lambertian surface varies with this dot product. When applying the spacetime analysis, the “goodness of fit” to the ideal spacetime Gaussian is also a confidence indicator. If the width of the Gaussian fit to the data deviates from the ideal width, then the data is accordingly downweighted, or even discarded. Additionally, at a step discontinuity, range data may be less reliable. The false edge extensions associated with traditional triangulation illustrate this point. Even in the case of spacetime analysis, the quality of edges is suspect due to filtering and resolution limitations.

¹If the points \mathbf{x}_s comprise the implicit surface defined by $F(\mathbf{x}) = \text{const}$, then the gradient of $F(\mathbf{x})$ at the surface, $\nabla F(\mathbf{x}_s)$, corresponds exactly to the normals over the surface [Edwards & Penney 1982].

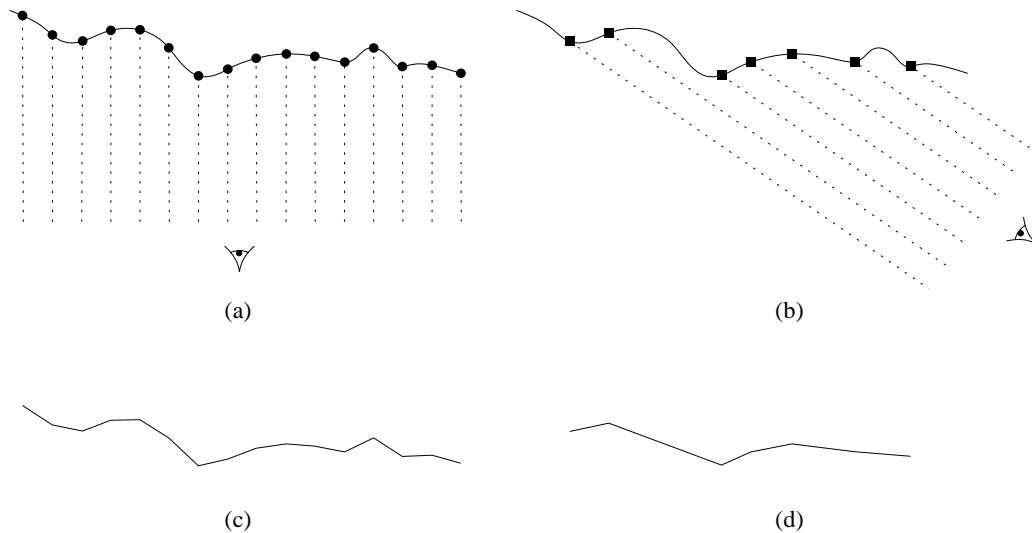


Figure 6.7: Dependence of surface sampling rate on view direction. When a surface is viewed “head on” as in (a), the sampling rate is on average significantly higher than when the surface is viewed from a grazing angle, as in (b). Note the greater detail in the estimated range surfaces, (c) versus (d).

The variations in weights can also be chosen for very practical considerations. If a surface is roughly planar with some moderate surface detail, then we would expect that a direct view of this surface in line with the predominant surface normal would give a higher quality range surface than a grazing angle view of the same surface. Figure 6.7 illustrates this idea. In general, separation between samples on the surface gives an indication of the comparative sampling rates among different range images. This sample separation is well approximated by $1/\cos \gamma$ where γ is the angle between the surface normal and the viewing direction. Thus, by setting the weights to be proportional to $\cos \gamma$ or even a higher power (e.g., $\cos^2 \gamma$), the contributions from the range surfaces can be biased in favor of range views with higher surface sampling rates.

Reducing weights near surface boundaries serves a practical purpose as well: smooth blending of range surfaces. Consider the example in Figure 6.8. If the vertex weights are not tapered near the boundary of a range surface, then when it is merged with another range surface, there will be an abrupt jump from the average of two surfaces to a single surface. By tapering the vertex weights to zero in the vicinity of the boundary of a range surface, this surface will blend smoothly with other range surfaces.

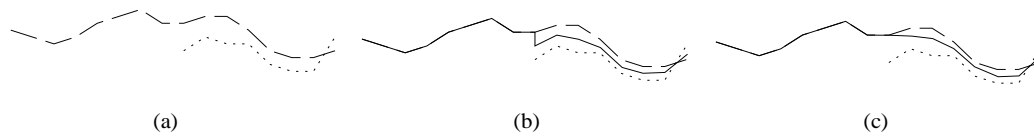


Figure 6.8: Tapering vertex weights for surface blending. (a) Two surfaces overlap, but one surface (shown dotted) has a boundary. (b) If the surface weights are not tapered near the boundary, then an abrupt transition appears when merging the surfaces, as indicated by the merged surface (solid line). (c) By tapering the surface weights near the boundary, the surfaces blend smoothly together.

6.2 Hole filling

The algorithm described in the previous section is designed to reconstruct the observed portions of the surface. Unseen portions of the surface will appear as holes in the reconstruction. While this result is an accurate representation of the known surface, the holes are esthetically unsatisfying and can present a stumbling block to follow-on algorithms that expect continuous meshes. In [Krishnamurthy & Levoy 1996], for example, the authors describe a method for parameterizing patches that entails generating evenly spaced grid lines by walking across the edges of a mesh. Gaps in the mesh prevent the algorithm from creating a fair parameterization. As another example, rapid prototyping technologies such as stereolithography typically require a “watertight” model in order to construct a solid replica [Dolenc 1993].

One option for filling holes is to operate on the reconstructed mesh. If the regions of the mesh near each hole are very nearly planar, then this approach works well. However, holes in the meshes can be (and frequently are) highly non-planar and may even require connections between unconnected components. Instead, we offer a hole filling approach that operates on our volume, which contains more information than the reconstructed mesh.

6.2.1 A hole-filling algorithm

The key to our algorithm lies in classifying all points in the volume as being in one of three states: unseen, empty, or near the surface. Holes in the surface are indicated by frontiers between unseen regions and empty regions (see Figure 6.9). Surfaces placed at these frontiers offer a plausible way to plug these holes (dotted in Figure 6.9). Obtaining this classification and generating these hole fillers leads to a straightforward extension of the algorithm

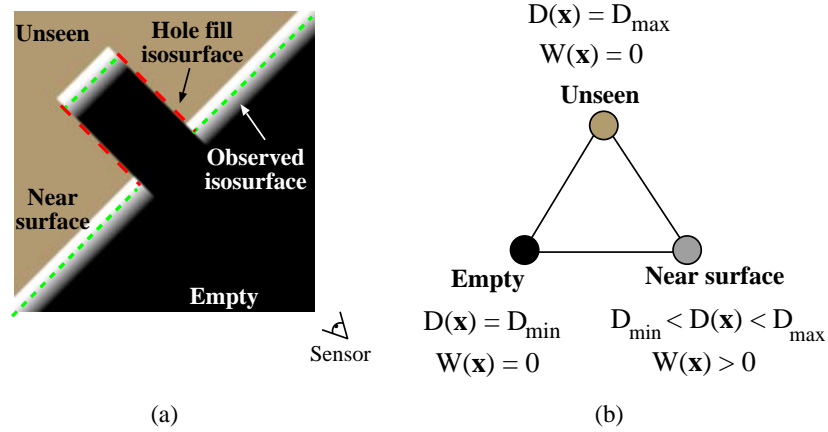


Figure 6.9: Volumetric grid with space carving and hole filling. (a) The regions in front of the surface are seen as empty, regions in the vicinity of the surface ramp through the zero-crossing, while regions behind remain unseen. The green (dashed) segments are the isosurfaces generated near the observed surface, while the red (dotted) segments are hole fillers, generated by tessellating over the transition from empty to unseen. In (b), we identify the three extremal voxel states with their corresponding function values.

described in the previous section:

1. Initialize the voxel space to the “unseen” state.
2. Update the voxels near the surface as described in the previous section. As before, these voxels take on continuous signed distance and weight values.
3. Follow the lines of sight back from the observed surface and mark the corresponding voxels as “empty”. We refer to this step as *space carving*.
4. Perform an isosurface extraction at the zero-crossing of the signed distance function. Additionally, extract a surface between regions seen to be empty and regions that remain unseen.

In practice, we represent the unseen and empty states using the function and weight fields stored on the voxel lattice. We represent the unseen state with the function values $D(\mathbf{x}) = D_{max}$, $W(\mathbf{x}) = 0$ and the empty state with the function values $D(\mathbf{x}) = D_{min}$, $W(\mathbf{x}) = 0$, as shown in Figure 6.9b. The key advantage of this representation is that we can use the same isosurface extraction algorithm we used in the previous section this time lifting the prohibition on interpolating voxels of zero weight. This extraction finds both the signed

distance and hole fill isosurfaces and connects them naturally where they meet, i.e., at the corners in Figure 6.9a where the dotted red line meets the dashed green line. Note that the triangles that arise from interpolations across voxels of zero weight are distinct from the others: they are hole fillers. We take advantage of this distinction when smoothing surfaces as described below.

Figure 6.9 illustrates the method for a single range image, and provides a diagram for the three-state classification scheme. Figure 6.10 illustrates how the hole filler surfaces connect to the observed surfaces. The hole filler isosurfaces are “false” in that they are not representative of the observed surface, but they do derive from observed data. In particular, they correspond to a boundary that confines where the surface could plausibly exist. Thus, the combination of the observed surfaces and the hole fill surfaces represents the object of maximum volume which is consistent with all of the observations. In practice, we find that many of the hole fill surfaces are generated in crevices that are hard for the sensor to reach.

6.2.2 Carving from backdrops

We have just seen how “space carving” is a useful operation: it tells us much about the structure of free space, allowing us to fill holes in an intelligent way. However, our algorithm only carves back from observed surfaces. There are numerous situations where more carving would be useful. For example, the interior walls of a hollow cylinder may elude digitization, but by seeing through the hollow portion of the cylinder to a surface placed behind it, we can better approximate its geometry. We can extend the carving paradigm to cover these situations by placing such a backdrop behind the surfaces being scanned. By placing the backdrop outside of the voxel grid, we utilize it purely for carving space without introducing its geometry into the model. Figure 6.11 illustrates the utility of space-carving with backdrops.

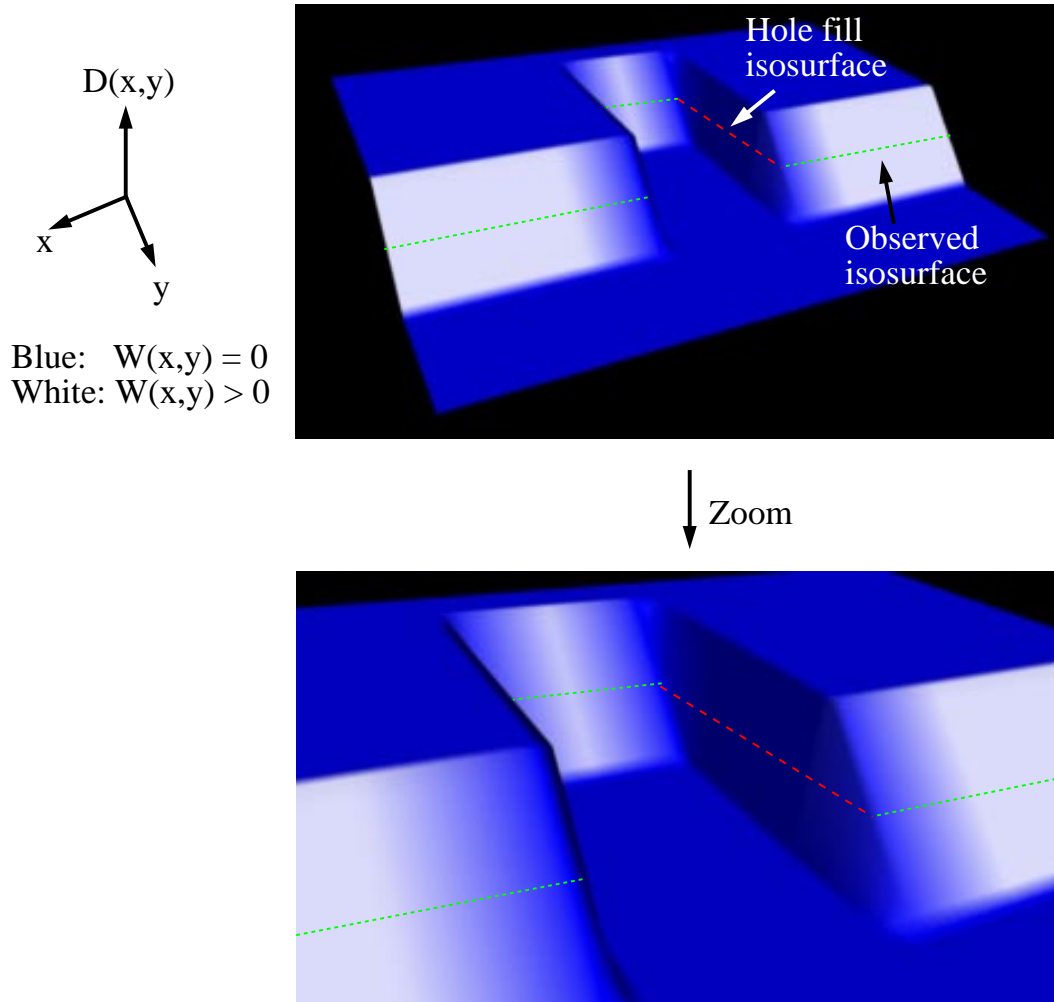


Figure 6.10: A hole-filling visualization. The images represent a slice through the volumetric grid depicted in Figure 6.9. The height of the ramps correspond to the signed distance field, $D(x, y)$, and the shading corresponds to the weight, $W(x, y)$. The isosurface is extracted at the level shown, where the dotted green lines correspond to observed surfaces and the dashed red lines correspond to hole-fill surfaces. Note how the observed and hole-fill surfaces connect seamlessly, with only a change in weights (going to zero at the hole-fill regions) to indicate the transitions.

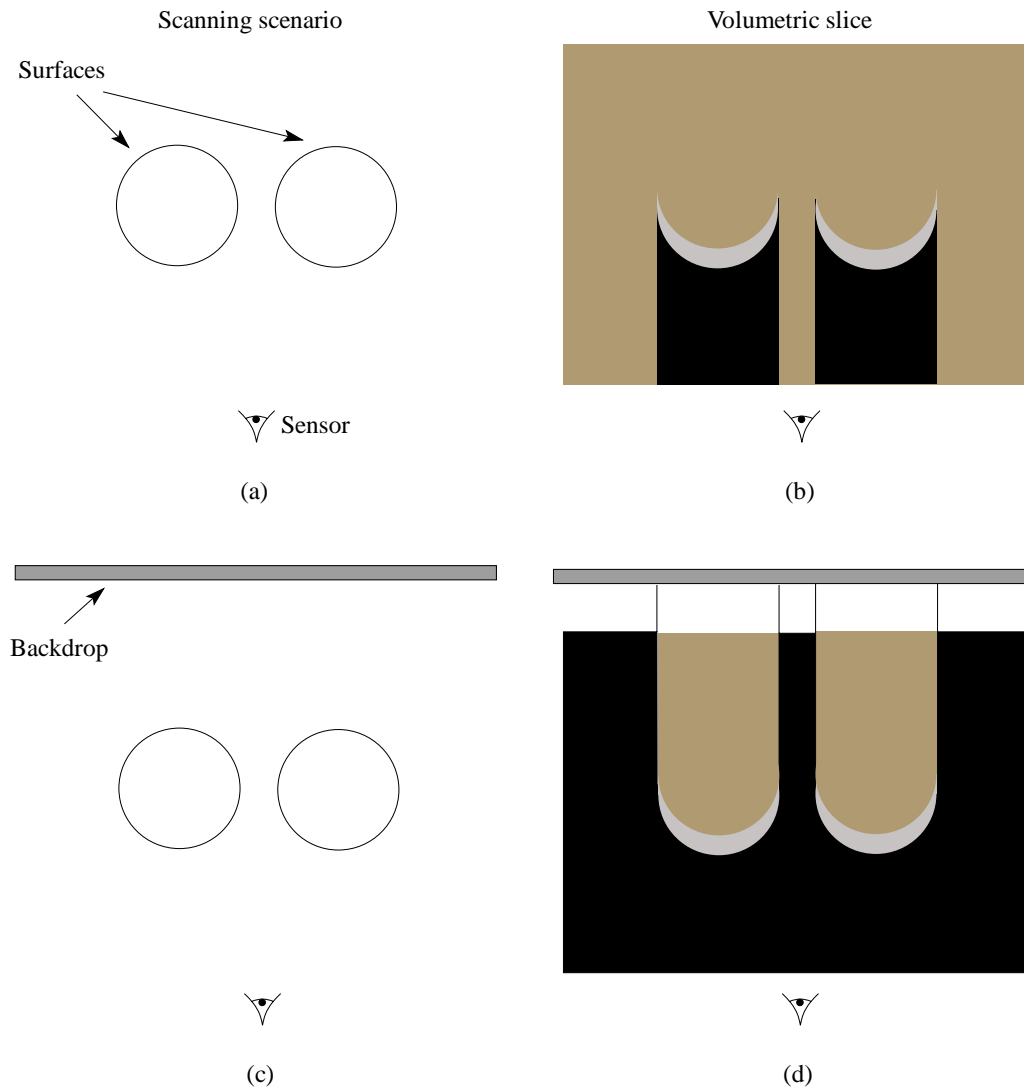


Figure 6.11: Carving from backdrops. (a) An orthographic sensor captures a range image of two cylinders. (b) A slice through the volumetric grid after laying down signed distance ramps near the observed surface and carving out the empty regions in front of the surfaces. It will be difficult to scan the portions of the cylinders that are close together. (c) The same scene as in (a) with the addition of a backdrop. (b) The volumetric slice after scanning the cylinders with a backdrop placed behind them. Much more of the space is carved as empty, and the cylinders are clearly segregated by the empty region between them.

6.3 Sampling, conditioning, and filtering

Operating in a sampled domain requires attention to several details. In this section, we begin by developing criteria for choosing the voxel resolution. Next, we show how the gradient variations can introduce artifacts when extracting an isosurface from a sampled volume, and we develop the notion of a conditioning function to address the problem. Finally, we describe methods for coping with the aliasing artifacts that arise when extracting hole fill surfaces.

6.3.1 Voxel resolution and tessellation criteria

Choosing the appropriate voxel resolution is crucial to avoiding aliasing artifacts in the surface reconstruction. Intuitively, the voxel resolution should be sufficient to sample the distance ramp and should be chosen to match the level of detail of the range surface.

To derive a criterion for the voxel resolution, we examine the problem from a signal processing point of view. Combining multiple range surfaces with weighted averages leads to a complicated analysis that does not offer many insights. Accordingly, we restrict the analysis to the case of determining the volumetric sampling rate required to represent a single range surface as a signed distance function. We will consider the role of weights in the context of isosurfaces in the next section.

In order to estimate the required voxel resolution, we must determine the bandwidth of the signed distance representation for a range surface. We define the symbols s_x , s_y , and s_z to correspond to the spatial frequencies in x , y , and z . The radial spatial frequency is then:

$$\rho_{s_x s_y s_z} = \sqrt{s_x^2 + s_y^2 + s_z^2}$$

and we hope to derive an expression for:

$$\rho_{s_x s_y s_z}^{max} \leq \sqrt{(s_x^{max})^2 + (s_y^{max})^2 + (s_z^{max})^2}$$

where $\rho_{s_x s_y s_z}^{max}$ is the radial bandlimit.

Consider the case of an orthographic sensor looking down the z -axis having acquired a

range surface, $f(x, y)$. For this single scan, the volume will store:

$$D(x, y, z) = d(z - f(x, y))$$

where $d(z)$ is the signed distance function centered at $z = 0$. Taking the Fourier transform:

$$\mathcal{F}\{D\} = \iiint d(z - f(x, y)) \exp[-i2\pi(s_x x + s_y y + s_z z)] dx dy dz$$

Regrouping the terms, we obtain:

$$\begin{aligned} \mathcal{F}\{D\} &= \iint \exp[-i2\pi(s_x x + s_y y)] \left\{ \int d(z - f(x, y)) \exp[-i2\pi s_z z] dz \right\} dx dy \\ &= \iint \exp[-i2\pi(s_x x + s_y y)] \mathcal{F}_z\{d(z)\} \exp[-i2\pi s_z f(x, y)] dx dy \\ &= \mathcal{F}_z\{d(z)\} \mathcal{F}_{xy}\{\exp[-i2\pi s_z f(x, y)]\} \end{aligned}$$

This equation reveals that the Fourier transform of the signed distance is partially separable; i.e., a product of the Fourier transform in z and the transform in xy . The z transform pertains to a known function, the signed distance ramp, and is thus easily computed. The xy transform has a significantly more complicated argument that includes the z component of frequency, s_z . Ultimately, we would like to derive the bandwidth of $\mathcal{F}\{D\}$ to help decide the necessary sampling rate for accurate shape capture without aliasing. To do so, we need to relate some property of the function $f(x, y)$ to the frequency content of the the xy transform.

One revealing measure that corresponds to bandwidth is the 2D variance of the squared magnitude of the $s_x s_y$ spectrum of a function $p(x, y)$ [Bracewell 1986],

$$(\Delta \rho_{s_x s_y})^2 \equiv \frac{\iint (s_x^2 + s_y^2) |P(s_x, s_y)|^2 ds_x ds_y}{\iint |P(s_x, s_y)|^2 ds_x ds_y} \quad (6.6)$$

where $P(s_x, s_y)$ is the Fourier transform of $p(x, y)$, and we have assumed the first central

moment to be zero. A more convenient definition of this variance arises after the application of several relations. The first is Rayleigh's theorem:

$$\iint |G(s_x, s_y)|^2 ds_x ds_y = \iint |g(x, y)|^2 dx dy \quad (6.7)$$

where $G(s_x, s_y)$ is the Fourier transform of a function $g(x, y)$. The second two relations are the rules of Fourier transforms and partial differentiation:

$$s_x G(s_x, s_y) = \frac{-i}{2\pi} \frac{\partial}{\partial x} g(x, y) \quad (6.8)$$

$$s_y G(s_x, s_y) = \frac{-i}{2\pi} \frac{\partial}{\partial y} g(x, y) \quad (6.9)$$

$$(6.10)$$

After re-writing Equation 6.6 as

$$(\Delta \rho_{s_x s_y})^2 = \frac{\iint |s_x P(s_x, s_y)|^2 ds_x ds_y + \iint |s_y P(s_x, s_y)|^2 ds_x ds_y}{\iint |P(s_x, s_y)|^2 ds_x ds_y} \quad (6.11)$$

then we can combine Equations 6.7-6.11 to obtain the following relation:

$$(\Delta \rho_{s_x s_y})^2 = \frac{1}{4\pi^2} \frac{\iint \left| \frac{\partial}{\partial x} p(x, y) \right|^2 + \left| \frac{\partial}{\partial y} p(x, y) \right|^2 dx dy}{\iint |p(x, y)|^2 dx dy}$$

Now we can make the substitution:

$$p(x, y) = \exp[-i2\pi s_z f(x, y)]$$

which leads to the following expression:

$$(\Delta\rho_{s_x s_y})^2 = \frac{s_z^2 \iint_A \left\{ \left| \frac{\partial}{\partial x} f(x, y) \right|^2 + \left| \frac{\partial}{\partial y} f(x, y) \right|^2 \right\} dx dy}{\iint_A dx dy} \quad (6.12)$$

where A is the area over which the range surface is defined. At the bandlimit, s_z obtains its maximum value s_z^{max} as set by the signed distance function. We can approximate the square of the overall bandwidth to be:

$$(\rho_{s_x s_y s_z}^{max})^2 \approx (s_z^{max})^2 + (\Delta\rho_{s_x s_y})^2 \quad (6.13)$$

After noting that $\iint_A dx dy = A$, we substitute Equation 6.12 into Equation 6.13 to obtain:

$$(\rho_{s_x s_y s_z}^{max})^2 \approx \frac{(s_z^{max})^2}{A} \iint_A \left\{ 1 + \left| \frac{\partial}{\partial x} f(x, y) \right|^2 + \left| \frac{\partial}{\partial y} f(x, y) \right|^2 \right\} dx dy \quad (6.14)$$

We can make this relation easier to understand if we define:

$$\langle g(x, y) \rangle \equiv \frac{1}{A} \iint_A g(x, y) dx dy \quad (6.15)$$

to be the area average of $g(x, y)$, and we observe that the normal to the surface in the z direction is (see Section 5.5):

$$n_z(x, y) = \frac{-1}{\sqrt{1 + \left| \frac{\partial}{\partial x} f(x, y) \right|^2 + \left| \frac{\partial}{\partial y} f(x, y) \right|^2}} \quad (6.16)$$

Combining Equations 6.14-6.16, we arrive at the following relation for the bandwidth of the surface convolved with the signed distance function:

$$\rho_{s_x s_y s_z}^{max} = s_z^{max} \sqrt{\left\langle \frac{1}{|n_z(x, y)|^2} \right\rangle}$$

In other words, the bandwidth is set by the average square value of the reciprocal of the component of the surface normal along the viewing direction. It is therefore very sensitive to

surfaces at grazing angles to the sensor; i.e., as n_z approaches zero, the bandwidth becomes very large, requiring high sampling rates.

We can derive a simple rule of thumb for the sampling rate if we consider a single planar surface. In this case, the bandwidth expression simplifies to:

$$\rho_{s_x s_y s_z}^{max} \approx \frac{s_z^{max}}{n_z}$$

To make this relation useful, we need to know the value of s_z^{max} . We can model the signed distance function, clipped to have a width of twice the maximum uncertainty interval with the function:

$$d(z) = z \cdot \text{rect}\left(\frac{z}{b}\right)$$

where b is width of the distance ramp. The Fourier transform of this function is:

$$\mathcal{F}\{d\} = \frac{ib}{2\pi} \frac{d(\text{sinc}(bs_z))}{ds_z}$$

where $\text{sinc}(x) = \sin(\pi x)/\pi x$. We can define the first zero crossing of this function to be the bandwidth of the signed distance function. This zero crossing occurs at $s_z^{max} = 1/b$, leading to the relation:

$$\rho_{s_x s_y s_z}^{max} \approx \frac{1}{bn_z}$$

Thus, the spacing between voxels (Δ) should be small enough that the sampling frequency ($1/\Delta$) exceeds the Nyquist sampling rate:

$$\Delta \leq \frac{bn_z}{2} \tag{6.17}$$

This relationship provides several insights. First, the voxel spacing must be small enough to sample the distance ramp adequately, as indicated by the proportionality to the ramp width b . Less noisy range data requires a narrower distance ramp and a smaller voxel spacing. In addition, the dependence on n_z is closely related to range image tessellation. When a range

image is converted to a range surface, a tessellation criterion determines whether neighboring range samples should be connected. This criterion typically takes the form of a minimum threshold normal component in the direction of the sensor or a maximum permissible edge length. The edge length criterion is very similar to the normal component criterion. Thus, the range surface tessellation criterion enforces a bound on the maximum voxel spacing.

Equation 6.17 can also be seen as a guideline for modifying the distance ramps and tessellation criteria to satisfy a desired sampling rate. In other words, the distance ramp can be seen as a bandlimiting filter; widening the ramp decreases the required sampling rate. Applying a more restrictive tessellation criterion has a similar effect.

While Equation 6.17 is based on the unweighted signed distance for a single range image, our experience has shown that it serves as an excellent guide for avoiding aliasing artifacts even when using weighted averages of signed distances for multiple range images.

6.3.2 Conditioning the implicit function

The algorithm described in this chapter uses a weighted *average* of the signed distances, yet in the previous chapter we showed that a simple weighted *sum* would suffice. In this section, we show why dividing by the sum of the weights is advantageous.

As shown in the previous chapter, the governing equation for finding a least squares solution is:

$$\sum_{i=1}^p |\mathbf{v}_i(x, y, z)| w_i(x, y, z) d_i(x, y, z) = 0$$

Without altering the position of the least squares isosurface, we can multiply this equation by a strictly positive conditioning function, $\kappa(x, y, z)$:

$$\kappa(x, y, z) \sum_{i=1}^p |\mathbf{v}_i(x, y, z)| w_i(x, y, z) d_i(x, y, z) = 0$$

One such conditioning function is the reciprocal of the sum of the weights:

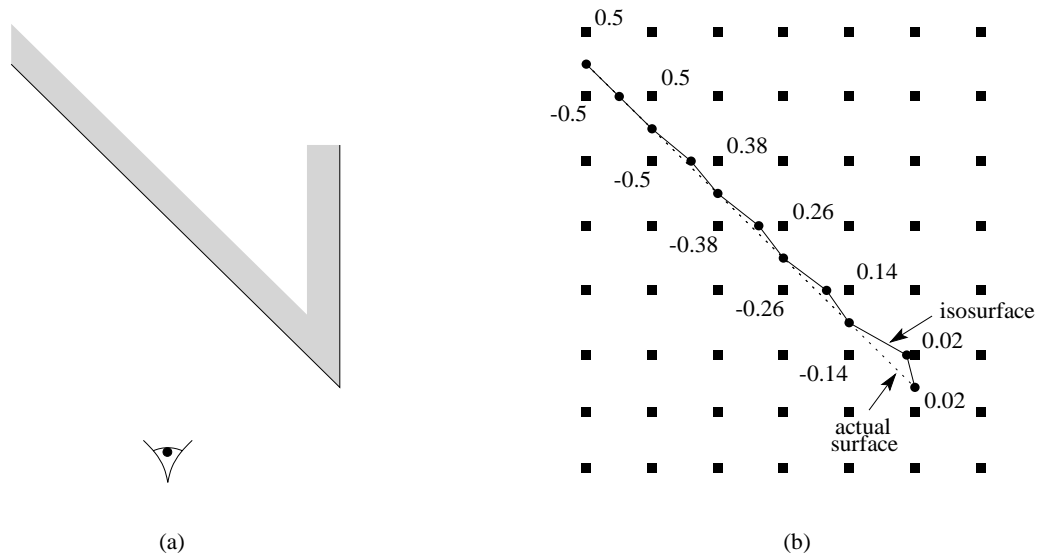


Figure 6.12: Tessellation artifacts near a planar edge. (a) A range sensor scans a planar surface up to an edge. (b) The product of the signed distance and the weights are laid down into the volume. The weights taper near an edge causing the value-weight product to shrink. The square markers are voxels, the dotted line is the actual surface, and the solid line is the extracted isosurface. Note the tessellation artifacts that result from the variations in weight.

$$\kappa(x, y, z) = \frac{1}{\sum w_i(x, y, z)} \quad (6.18)$$

which corresponds to computing a weighted average of the signed distances at each voxel.

But what is the utility of a conditioning function? To answer this question, we consider the impact of tapering weights near mesh boundaries. Figure 6.12 depicts a planar surface with a boundary edge after being merged into the volumetric grid. Tapering the weights near the boundary is intended to make for a smoother blend when merging overlapping surfaces, but the decreasing weights, when multiplied by the signed distance, alter the gradient of the implicit function. Isosurface extraction methods such as the Marching Cubes algorithm are very sensitive to variations in the gradient, and the resulting isosurface has artifacts as depicted in the figure. On the other hand, after dividing by the sum of the weights (for a single scan, this amounts to unweighted signed distance), the gradient is constant and no artifacts appear.

Figure 6.13 shows the effect of using sums of weighted distances versus the use of

weighted averages of signed distances when merging range images. Clearly, the weighted average conditioning smooths the gradient and avoids artifacts associated with the unconditioned isosurface.

The examples in Figure 6.13 show how the sum of weights conditioning function (Equation 6.18) can help reduce variations in the gradient to produce better isosurfaces. To see how we might design different conditioning functions, we can derive an expression for the gradient magnitude of the conditioned signed distance function:

$$\begin{aligned} |\nabla D| &= \left| \nabla \left[\kappa \sum_{i=1}^p |\mathbf{v}_i| w_i d_i \right] \right| \\ &= \left| \nabla \kappa \sum_{i=1}^n |\mathbf{v}_i| w_i d_i + \kappa \nabla \sum_{i=1}^p |\mathbf{v}_i| w_i d_i \right| \end{aligned}$$

Since we are only interested in the gradient in the immediate vicinity of the isosurface, the first term on the right hand side of the last equation vanishes to give:

$$\begin{aligned} |\nabla D|_{iso} &= \left| \kappa \nabla \sum_{i=1}^p |\mathbf{v}_i| w_i d_i \right| \\ &= \kappa \left| \sum_{i=1}^p \nabla (|\mathbf{v}_i| w_i d_i) \right| \end{aligned}$$

where $|\nabla D|_{iso}$ is the gradient magnitude at the isosurface. Thus, we can ensure a uniform gradient magnitude in the vicinity of the isosurface by setting the conditioning function to be:

$$\kappa = \frac{1}{\left| \sum_{i=1}^p \nabla (|\mathbf{v}_i| w_i d_i) \right|}$$

This observation leads to a uniform gradient algorithm. At each voxel we would store a scalar and a *vector*. The scalar would be the cumulative weighted signed distance, and the

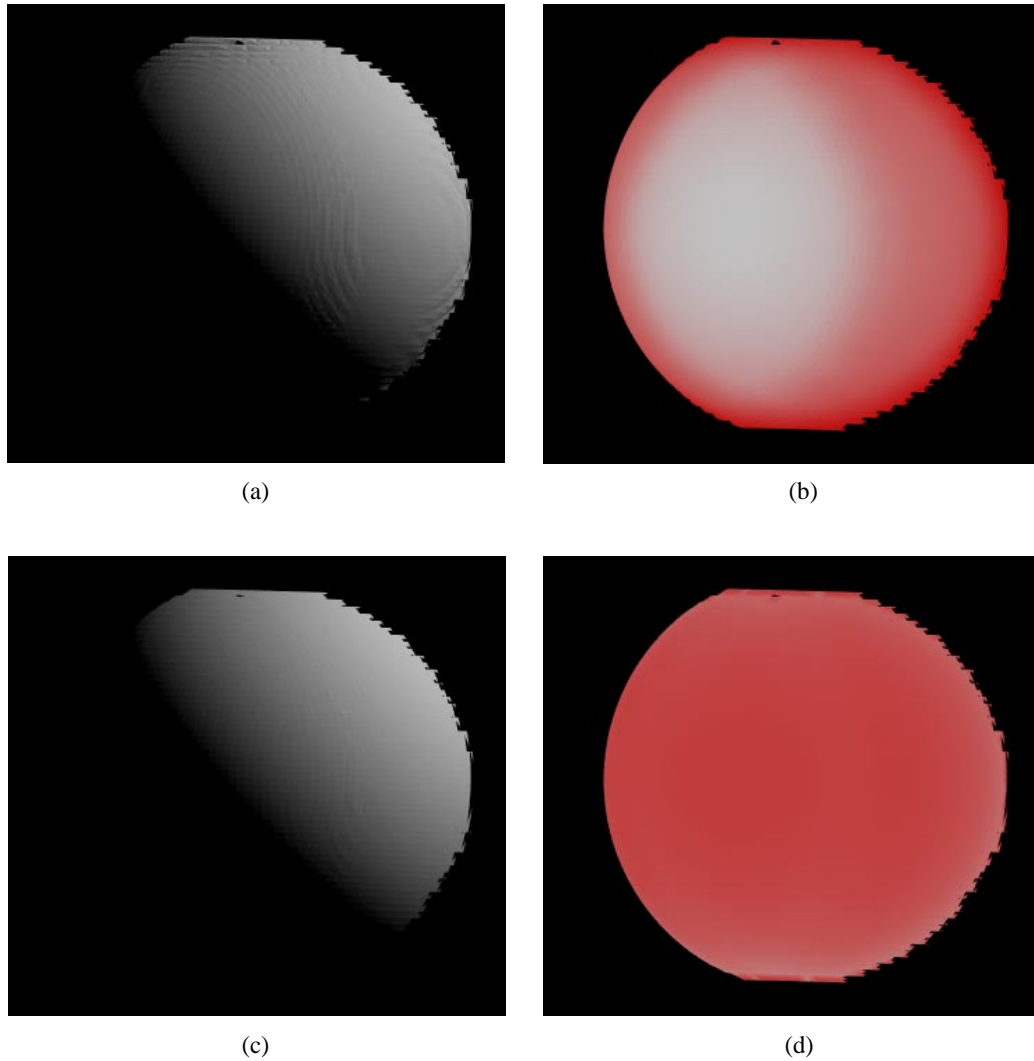


Figure 6.13: Isosurface artifacts and conditioning functions. Noiseless synthetic range images were constructed from a perfect sphere scanned orthographically from two directions spaced 45 degrees apart. The scans were merged using two techniques, one with and one without a conditioning function. (a) and (c) are faceted renderings of the resulting isosurfaces, lit to emphasize artifacts. (b) and (d) are the gradient magnitudes across the isosurface. Red areas have small gradients while white areas have large gradients. In (a) and (b), no conditioning function is used, and “ripples” appear in the rendering (a) due to variations in the gradient evident in (b). In (c) and (d), a weighted average conditioning function is used, and the result is a smooth surface (c) with little variation in the gradient (b). The hole at the tops and the jagged boundaries of the reconstructions are artifacts of the marching cubes algorithm operating on the discrete voxel grid used in this illustration.

vector would be the sum of the gradients computed at each voxel for each scan. After merging a set of scans, we would divide the scalar by the magnitude of the vector at each voxel to yield a volume with gradients normalized in the vicinity of the isosurface. While we have yet to implement such an algorithm, it holds promise for minimizing isosurface artifacts due to gradient magnitude variations.

6.3.3 Mesh filtering vs. anti-aliasing in hole fill regions

Artifacts in the isosurface also arise when applying the method of hole filling by carving space. Because the transition between unseen and empty is discontinuous and hole fill triangles are generated as an isosurface between these binary states, with no smooth transition, we generally observe aliasing artifacts in these areas. These artifacts can be eliminated by pre-filtering the transition region before sampling on the voxel lattice using straightforward methods such as analytic filtering or super-sampling and averaging down. In practice, we have obtained satisfactory results by applying another technique: post-filtering the mesh after reconstruction using weighted averages of nearest vertex neighbors as described in [Taubin 1995]. The effect of this filtering step is to fair the hole fill surface. Since we know which triangles correspond to hole fillers, we need only concentrate the surface filtering on these portions of the mesh. This localized filtering preserves the detail in the observed surface reconstruction. To achieve a smooth blend between filtered hole fill vertices and the neighboring “real” surface, we allow the filter weights to extend beyond and taper off into the vicinity of the hole fill boundaries.

6.4 Limitations of the volumetric method

The volumetric method described in this section has several limitations. The first two concern the ability to determine accurate shape from observed surfaces, while the third is a limitation inherent in the process of space carving.

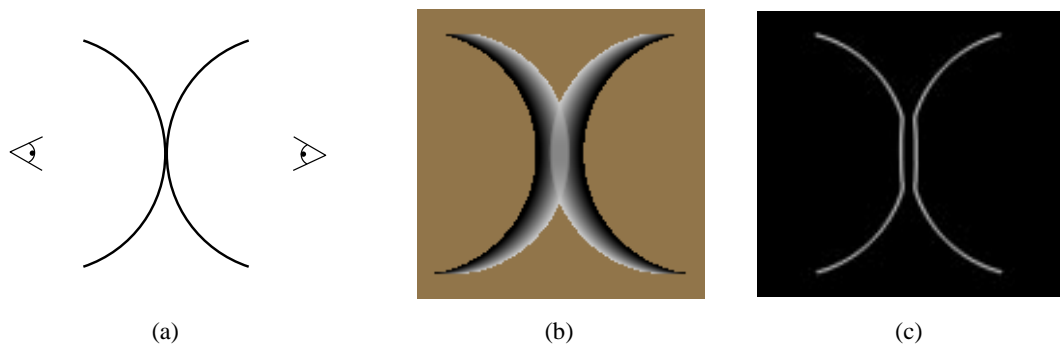


Figure 6.14: Limitation on thin surfaces. (a) A surface is scanned from two sides. (b) The volumetric grid shows that the distance ramps overlap as the opposing surfaces come close together. (c) The resulting isosurface shows that the interference of signed distance functions results in a thicker surface.

6.4.1 Thin surfaces

As described earlier in this chapter, the width of each signed distance ramp is made as small as possible while ensuring overlap with ramps taken from the same side of a surface. However, when opposing surfaces come within a ramp width of each other, then the signed distances taken from opposite sides of the surface begin to interfere. Figure 6.14 illustrates this point. In effect, this limitation imposes a minimum thickness of a feature that can be seen from two sides. This is also problematic for sharp corners. At the tip of a corner, the adjoining faces come arbitrarily close together, and opposing scans (i.e., scans that do not see both sides of the corner) will necessarily interfere with one another in the volume, as shown in Figure 6.16a-c.

The fundamental problem is the inability of the volumetric representation to distinguish opposing surfaces before combining their distance functions. We may address this problem in several ways. For instance, we could begin by storing estimated surface normals for voxels in the neighborhood of the surface. These normals might arise by blending together estimated normals from individual range scans, though the noisiness of individual normal estimates will affect results. Alternatively, the normals may be derived from the initial reconstruction following a recipe such as: (1) reconstruct the surface, (2) reinitialize the volume, (3) deposit the surface normal of the nearest point on the surface into each

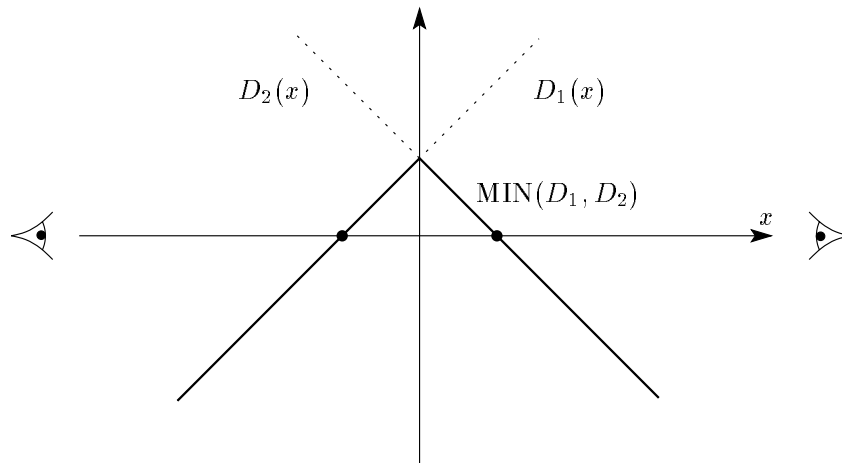


Figure 6.15: Using the $\text{MIN}()$ function to merge opposing distance ramps. Cumulative signed distance functions can be accumulated for differing orientations, as in the case of opposing surfaces. These distance functions are shown here in one dimension. Using the $\text{MIN}()$ function to merge these functions before extracting the isosurface will preserve the desired zero crossings.

voxel within the distance ramp of the surface. This second approach assumes that errors associated with thin surfaces are fairly isotropic; i.e., the erroneous thickening of the surface is roughly a simple dilation of the surface in the areas affected. Once approximate normals are established, then we can modify the method for merging range surfaces into the volume. A simple approach would restrict a range surface to influence only voxels whose normals are within some threshold of what could possibly be visible to the sensor.

These normal techniques can be extended to store more than one estimated surface normal and distance function per voxel. For example, if a voxel is between opposing surfaces, then the algorithm could store the estimated orientations for both of the opposing surfaces and update separate signed distances for range estimates coming from opposite sides. In general, storage requirements for this method would vary with the geometry of the object: in particularly complex regions, storage of multiple estimated normals may be necessary, whereas smoother regions without opposing surfaces would require only a single normal and signed distance. To reconstruct the final range surface, it might be possible to follow the contours of the two signed distances separately, and then merge the resulting geometry. Alternatively, these distances could be blended together using a $\text{MIN}()$ function before reconstruction as indicated in Figure 6.15.

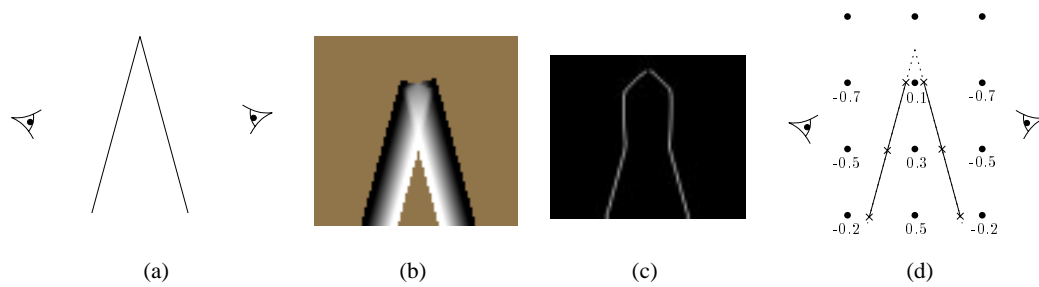


Figure 6.16: Limitations due to sharp corners. (a) A corner is scanned from two sides. (b) The volumetric grid shows the distance ramps overlapping opposite sides near the apex. (c) The isosurface shows a thickening of the corner and a gap at the apex. (d) Samples on the volumetric grid show that even ideal range data, merged into the volume in a manner avoiding surface thickening will lead to a gap in the reconstruction.

Other potential strategies include modifications to the weight functions. For example, if the weight functions begin to taper off along the sensor's line of sight for voxels behind the range surface, then the interference with the opposing surface will be reduced. However, when combining surface estimates on the same side of the surface, the tapered weights will introduce some bias into the reconstruction. Such an approach would affect the accuracy of the whole reconstruction, but selective application of this strategy might still be of use. By adjusting the weight profiles for range samples near boundaries, it is possible to reduce the surface thickening selectively in at least one of the more troublesome areas, i.e., near corners. Early experiments in this area have yielded promising results.

6.4.2 Bridging sharp corners

Another limitation of the volumetric method is the difficulty in bridging sharp corners, a problem which persists even if interference of opposing signed distances are eliminated. Consider the scenario in Figure 6.16. Two scans of a sharp corner acquire accurate descriptions of the corner up to the apex. However, when merging these scans into the volumetric grid, the restricted marching cubes tessellator cannot “turn the corner” and connect the two surfaces.

This difficulty is avoidable under two circumstances. If an additional scan observes both sides of the corner, then the corner is bridged. Alternatively, if the scans of the corner are observed to be occluding other geometry such as a backdrop, then the space carving step

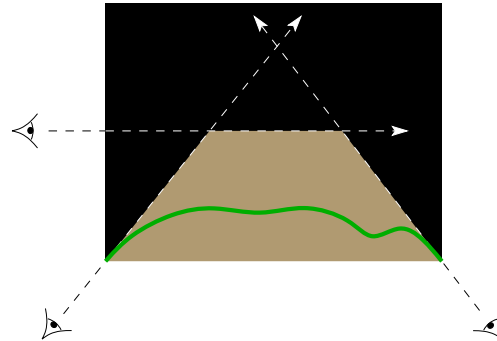


Figure 6.17: Intersections of viewing shafts for space carving. Three scans are taken from different points of view. The solid green curve is the actual surface. Due to occlusions (not shown), the bound on the object is determined primarily by space carving. Notice that in this two-dimensional example, the resulting boundary is an intersection of empty half-spaces and thus consists of large line segments with sizes that do not depend on the voxel resolution.

will declare the region near the apex to be empty. In this case, the hole filling algorithm will bridge the gap.

In the absence of an additional scan or the use of space carving, however, bridging the gap is still desirable. The range samples acquired at the apex from two viewpoints may be arbitrarily close together – even more closely spaced than the samples in individual range images – so the reconstruction algorithm ought to be able to bridge the gap. One possible solution would be a modified marching cubes algorithm that assumes regions of the volume near the surface are empty and performs a local hole-filling only to bridge small gaps. Alternatively, a different hole-filling algorithm could be applied as a post-process, directly filling small gaps in the polygonal reconstruction.

6.4.3 Space carving

In many cases, the space carving algorithm described in Section 6.2 can attain a reasonably tight bound on the object and lead to a plausible hole-free surface. In some cases, however, the hole-fill regions have undesirable properties. They represent intersections of viewing “shafts” that may in fact not achieve a tight bound on the surface and may appear as protrusions from the object, or, worse, they may change the topological genus of the reconstruction by introducing “handles”. Figures 6.17, 6.18 and 6.19 illustrate these possibilities.

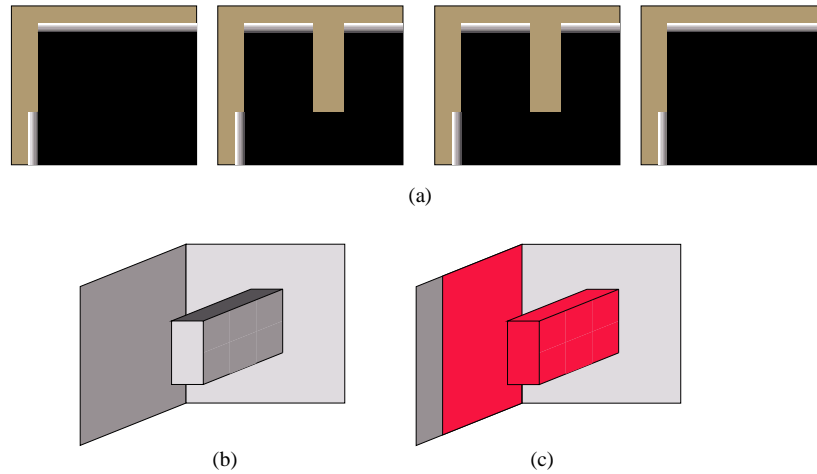


Figure 6.18: Protrusion generated during space carving. (a) Four slices through a volumetric grid show the signed distance ramps due to visible surfaces as well as the resultant space carving. (b) Taking an isosurface that includes hole-filling yields a surface with a protrusion. (c) Red surfaces indicate the hole fill regions of the isosurface.

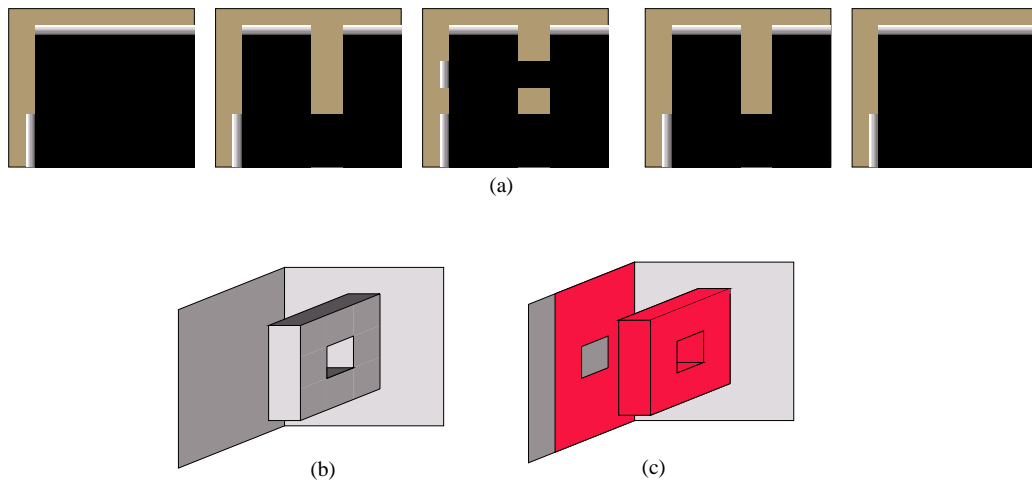


Figure 6.19: Errors in topological type due to space carving. (a) Five slices through a volumetric grid show the signed distance ramps due to visible surfaces as well as the resultant space carving. (b) The resulting isosurface has a “handle”. (c) Red surfaces indicate the hole fill regions of the isosurface.

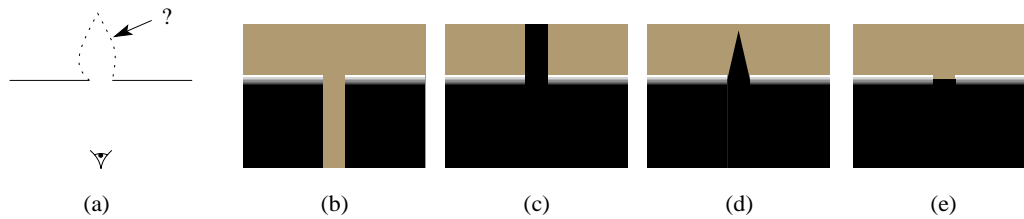


Figure 6.20: Aggressive strategies for space carving with a range sensor using a single line of sight per pixel. (a) A surface is scanned with a range sensor that has a single line of sight per sample. There is a gap in the recorded range data, which could correspond to the dotted surface. (b) A conservative strategy would carve space only from the observed surfaces. (c) A very aggressive strategy would incorporate the notion that missing data implies no surface along the sensor’s line of sight. In this case, the carving extends to the limit of the sensor’s field of view. (d) Due to sensitivity limitations, surfaces at grazing angles to the sensor may not be detected. This places a limit on how much space may be declared empty and still be consistent with a surface that just evades detection due to oblique orientation. (e) A still less aggressive strategy would simply fill the gap by bounding the emptiness at the line segment connecting the edges of the missing data. Such a strategy might lead to less objectionable hole fill regions such as would be generated by the indentation shown in (d).

These undesirable hole fillers might be removed at the volumetric level or by operating on the reconstructed surface. One volumetric approach might be to apply image processing operations such as erosions and dilations to modify the hole fill regions and possibly collapse thin unknown regions that lead to “handles” such as the one shown in Figure 6.19 [Jain 1989]. In addition, more aggressive space carving strategies could be employed to empty out more of space as illustrated in Figure 6.20. Consider a very simple range sensor with a single line of sight. If such a sensor were to return no measurement, we would normally draw no conclusions. In fact, barring a surface that is “invisible” to the sensor, one can argue that there is no surface along the sensor’s line of sight, or else it would have been detected. The space must therefore be empty in this direction. For a full range imaging sensor, we could follow all lines of sight that returned no range data and declare all these regions of the volume to be empty. In practice, this approach could not be applied indiscriminately. For instance, no data is returned from very dark regions of a surface or shiny portions that deflect the line of sight. Even if the surface were known to have a uniform diffuse reflectance, regions that are oblique to the sensor may not return enough light to be detected. In this case, there would be a limit to how far the space carving would proceed

while being consistent with the possibility that the surface is receding with steep slope. Figure 6.20 shows how this more aggressive space carving might proceed.

In the case of a triangulation scanner, space carving is complicated by the requirement that each point must have a clear line of sight to both the laser and the camera. The conservative approach consists of following the lines of sight from the surface to both the laser and the camera and declaring the voxels to be empty as shown in Figure 6.21. For the case of aggressive space carving, we refer to Figure 6.22. If we hypothesize that point A in Figure 6.22a is not empty, then there must be a surface that occludes the line of sight of the laser or the sensor, e.g., point B. But in order for point B to be an occluder, then there must be yet another surface that blocks its visibility. Following this line of reasoning, we eventually determine that a surface must exist in the region of space already conservatively declared to be empty in order to prevent the detection of point A. This contradiction leads to the conclusion that point A must be empty. By induction, we can then argue that all points that are accessible to both the laser and the sensor must be empty [Freyburger 1994]. As with the single line of sight rangefinder, less aggressive strategies are also possible (Figure 6.22e and f).

Another approach to improving the hole fill regions would be to operate directly on the polygonal reconstruction. For example, the tangent planes to the surface at the boundary between the hole fill and the observed surface could be used to coerce the hole fill to relax into a less protruding configuration. Ideally, such a relaxation procedure could be extended to modify the topology and collapse undesirable handles in the hole fill regions.

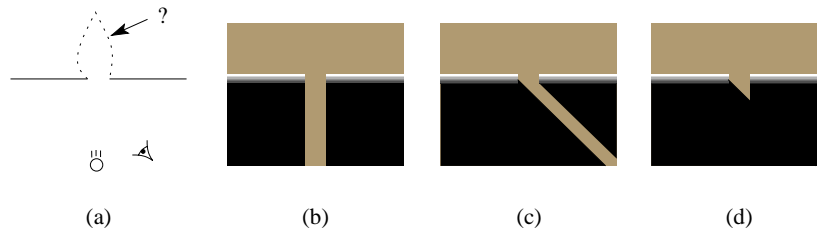


Figure 6.21: Conservative strategy for space carving with a triangulation range sensor. (a) A surface is scanned with a triangulation range sensor that has two lines of sight per sample. For the purpose of illustration, the camera is assumed orthographic and the scanning sweep to be linear. (b) The region of space that must be empty from the point of view of the laser. (c) The region of space that must be empty from the point of view of the camera. (d) The union of the empty spaces yields a conservative estimate of the emptiness of space around the observed surfaces.

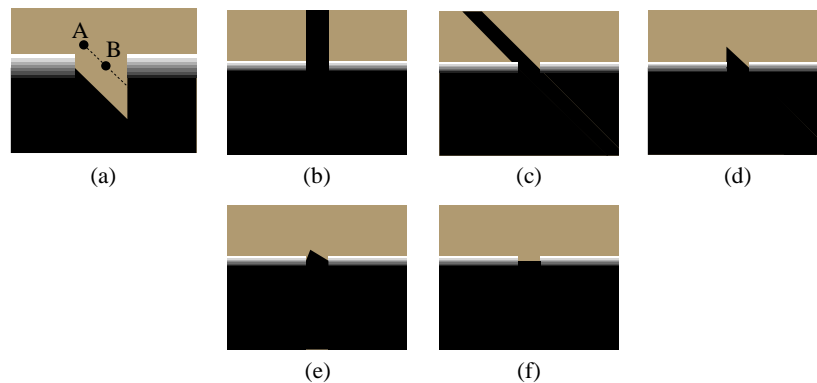


Figure 6.22: Aggressive strategies for space carving with a triangulation range sensor. The sensor geometry is assumed the same as in Figure 6.21a. (a) Magnified view of the hole fill region established by conservative space carving in Figure 6.21d. Following the arguments in the text, all points that could be visible to both the laser and the sensor must be empty. (b) The region of space that could be empty from the point of view of the laser. (c) The region of space that could be empty from the point of view of the camera. (d) The intersection of the empty regions in (b) and (c) yields an aggressive estimate about the emptiness of space around the observed surface. (e) Surfaces at grazing angle to the laser or camera might not be detected, so a less aggressive strategy would taper the boundaries of the space carving region. (f) As in Figure 6.20, a less aggressive strategy would simply fill the gap by bounding the emptiness at the line segment connecting the edges of the missing data.

Chapter 7

Fast algorithms for the volumetric method

The creation of detailed, complex models requires a large amount of input data to be merged into high resolution voxel grids. The examples in the next chapter include models generated from as many as 70 scans containing up to 12 million input vertices with volumetric grids ranging in size up to 160 million voxels. Clearly, time and space optimizations are critical for merging this data and managing these grids. In this chapter, we begin by describing a run-length encoding scheme for efficient storage of the volumetric data (Section 7.1). Next, we develop a number of optimizations designed to improve execution time when merging range data into the volume (Section 7.2). In Section 7.3, we summarize an efficient isosurface extraction method. Finally, we show that the storage and execution optimizations lead to significant improvements in asymptotic complexity (Section 7.4).

7.1 Run-length encoding

The core data structure is a run-length encoded (RLE) volume with three run types: empty, unseen, and varying. The varying fields are stored as an explicit stream data, rather than runs of constant value. Typical memory savings vary from 10:1 to 20:1. In fact, the space required to represent one of these voxel grids is usually *less* than the memory required to represent the final mesh as a list of vertices and triangle indices.

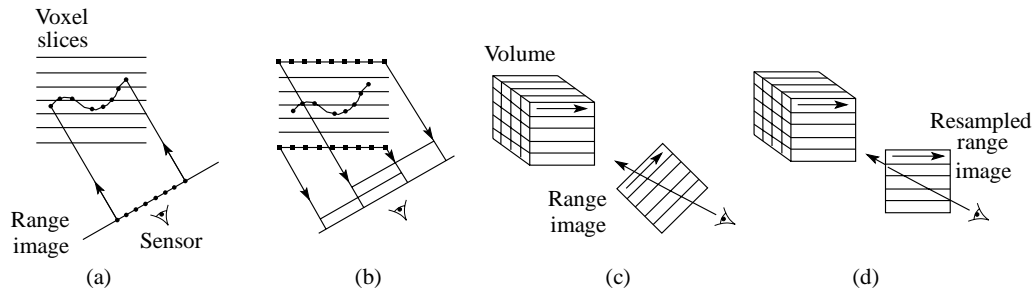


Figure 7.1: Overview of range image resampling and scanline order voxel updates. (a) Casting rays from the pixels on the range image means cutting across scanlines of the voxel grid, resulting in poor memory performance. (b) Instead, we run along scanlines of voxels, mapping them to the correct positions on the resampled range image. (c) Range image scanlines are not in general oriented to allow for coherently streaming through voxel and range scanlines. (d) By resampling the range image, we can obtain the desired range scanline orientation.

7.2 Fast volume updating

Updating the volume from a range image may be likened to inverse volume rendering: instead of reading from a volume and writing to an image, we read from a range image and write to a volume. Research in volume rendering has shown that the manner of traversing the volume and image is critical to the efficiency of the algorithm [Lacroute & Levoy 1994]. In particular, streaming through the image and following each line of sight through the volume leads to poor performance, because it requires random access to voxels that are not adjacent in memory, as shown in Figure 7.1a. We can instead step through the volume in scanline order, but this requires random access of the *image* pixels, leading to a similar memory access inefficiency, as shown in Figure 7.1c. The solution is to pre-warp the image in a manner that forces voxel and image scanlines to map onto each other.

In this section, we develop the geometric intuition for how the range image plane must be oriented to ensure ideal scanline alignment for both the orthographic and the perspective case. Next we describe methods of performing the resampling and subsequent updating of the volume. Obeying the more restrictive image plane requirement imposed by the perspective case, we show how we can develop a shear-warp method for resampling the range image and updating the volume. This shear-warp method leads to a fast algorithm using binary depth trees to update only relevant portions of the volume. Finally, we describe a fast

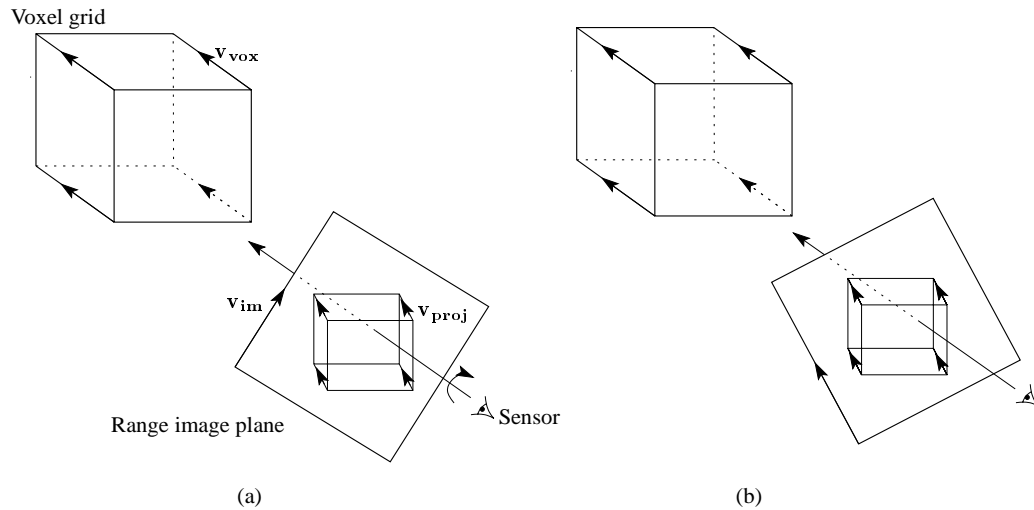


Figure 7.2: Orthographic range image resampling. As shown in (a), the voxel scanlines run in the direction v_{vox} . The projections of these scanlines onto the range image plane run along the direction v_{proj} , while the range image scanlines run in the direction v_{im} . By rotating the range image plane as shown in (b), we can align the directions of the projected voxel scanlines and the image scanlines. This affords coherent memory access when streaming through the voxel grid and the range image.

transpose method for ensuring that voxel scanlines run parallel to image scanlines.

7.2.1 Scanline alignment

The type of viewing frustum for a rangefinder imposes constraints on how to choose the range image resampling that guarantees volume and image scanline alignment. For an orthographic frustum, the desired alignment can be attained by simply rotating the image plane about the axis defined by the viewing direction. The amount of rotation can be determined by projecting the direction of the voxel scanlines onto the image plane, followed by rotating the image plane until the image scanlines align with the projected viewing directions (see Figure 7.2). Because the orthographic projection of the voxel scanlines is a set of parallel lines, it is always possible to rotate the range image about the view direction to assure mutual alignment of image and voxel scanlines.

Perspective viewing frustums impose additional constraints. The first requires that the new image plane be parallel to the voxel scanlines. Figure 7.3 shows how this constraint

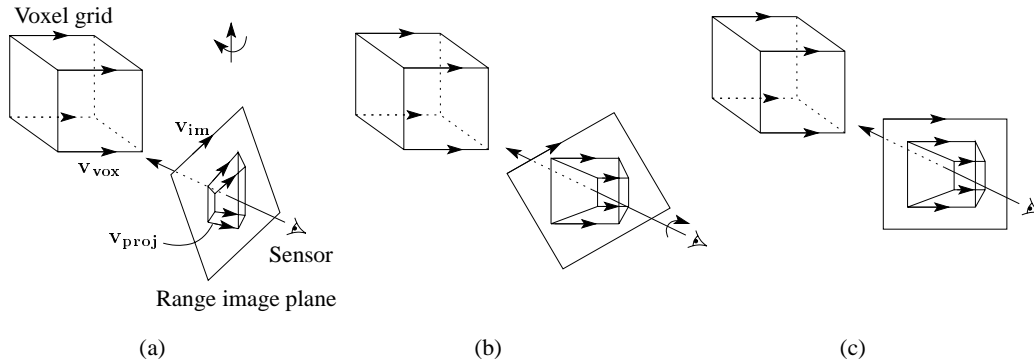


Figure 7.3: Perspective range image resampling. The notation follows that of Figure 7.2. In (a), the range image plane is at an angle to the front face of the voxel grid. As a result, the projected voxel scanlines are not parallel. By rotating the image plane so that the image plane is parallel to the voxel scanlines (b), we force the projected voxel scanlines to be parallel. As in the orthographic case, we must additionally rotate the image plane about the viewing axis to complete the mutual alignment.

applies. When coupled with rotating the image about the viewing axis, the resulting image scanlines, viewed as lines segments in three dimensions, now run exactly parallel to the voxel scanlines. An additional restriction applies to the direction of the *voxel* scanlines. Consider the case shown in Figure 7.4. As we follow the voxel scanlines away from the viewpoint, the projections of these scanlines progress toward the center of the image. Thus, no rotation of the image plane is suitable to align voxel and image scanlines. On the other hand, by reorganizing the voxel scanlines so that they run parallel to the image plane (i.e., by transposing the data structure), we obtain the desired alignment.

More complex viewing frustums can make it impossible to assure precise alignment of voxel and image scanlines, as is the case with the line perspective of the Cyberware scanner for traditional triangulation. In this case, we can choose an image orientation that is aligned with scanlines for one voxel slice, but the scanlines at different slices will project to curves that cross image scanlines. Nevertheless, if the projection is nearly orthographic, i.e., the rays are not severely divergent, then an image orientation can be chosen to minimize the amount that projected scanlines cross range image scanlines. If rays are highly divergent, then other methods, such as partitioning the range image resamplings into manageable sections may be applicable.

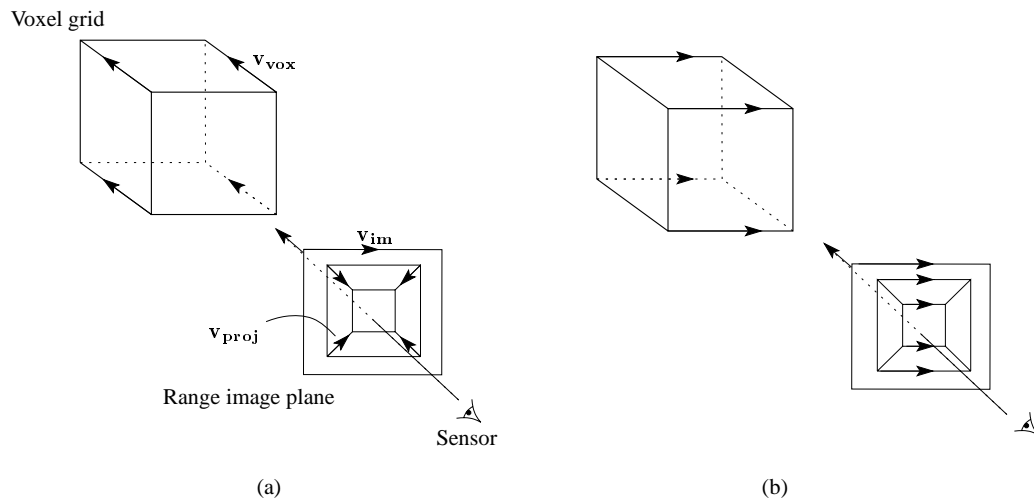


Figure 7.4: Transposing the volume for scanline alignment. The notation follows that of Figure 7.2. The projected voxel scanlines in (a) converge to the perspective vanishing point on the image plane. In this case, it is not possible to rotate the image plane to align with projected voxel scanlines. By transposing the volume (b), we see that the projected scanlines are now parallel.

7.2.2 Resampling the range image

To resample the range image using the newly oriented image plane, we first reconstruct the range surface. Next, we can cast a set of rays from the sensor through the image pixels and intersect them with the range surface. The distances along these rays are the range values to be stored in the new range image. By interpolating the weights at the vertices on the range surface, we can associate a new weight with each sample.

Alternatively, we can resample the range image using an incremental scan-conversion algorithm, a method known to be very efficient. In this case, we first transform the vertices of the range surface using the viewing transformation specific to the lines of sight of the range sensor and the image plane. The weights are then assigned as vertex “colors” to be linearly interpolated during the rendering step, an approach equivalent to Gouraud shading of triangle colors [Foley et al. 1992]. This resampling can be performed with a traditional z-buffered rendering algorithm, though no depth comparisons are necessary when entering values into the z-buffer (i.e., there must be exactly one depth per line of sight if the viewing rays are properly calibrated).

7.2.3 Updating the volume

To merge the range data into the voxel grid, we stream through the voxel scanlines in order while stepping through the corresponding scanlines in the resampled range image. We map each voxel scanline to the correct portion of the range scanline as depicted in Figure 7.1b, and we resample the range data to yield a distance from the range surface. Using the combination rules given by Equations 6.3 and 6.4, we update the run-length encoded structure. To preserve the linear memory structure of the RLE volume (and thus avoid using linked lists of runs scattered through the memory space), we read the voxel scanlines from the current volume and write the updated scanlines to a second RLE volume; i.e., we double-buffer the voxel grid.

7.2.4 A shear-warp factorization

In Section 7.2.1, we showed that forcing the range image scanlines to run parallel to the voxel scanlines is necessary for achieving good memory performance for perspective projections. If we require that this restriction holds in all cases (including orthography), then we can develop a shear-warp factorization of the viewing transformation, similar to the one described for volume rendering in [Lacroute & Levoy 1994]. The resulting algorithm utilizes a z-buffered scan-conversion algorithm and allows for computation of signed distances by comparing a scanline's constant z value against the resampled z values from the range image. This method of establishing signed distance will be exploited for more efficient voxel traversal using the binary depth trees described in the next section.

Figure 7.5 illustrates the shear warp procedure for an orthographic projection in two dimensions. We first transpose the voxel data structure so that the scanlines run as close to perpendicular to the viewing direction as possible. Then we shear both the range surface and voxel grid so that the viewing rays run perpendicular to the voxel slices. Note that shearing the voxel grid simply amounts to changing the origins of the voxel slices; no resampling of the voxels is ever performed. Next, we resample the range surface with respect to an image plane parallel to the voxel slices. As before, we stream through voxel scanlines and resample depths stored in the resampled range image. The difference between the z -depth of each voxel (constant within a scanline) and the resampled range depth corresponds to the signed

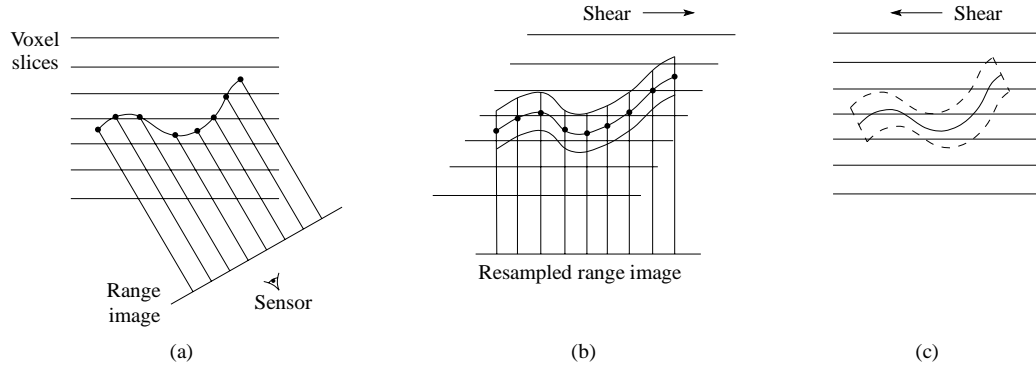


Figure 7.5: A shear warp method for parallel projection. (a) The range image and sensor lines of sight are not initially aligned with the voxel grid. (b) By shearing the grid and range image, we “straighten” the sensor rays with respect to the voxel grid. This shear performs the same function as the rotation in Figure 7.3. By resampling the range image, we align its pixels with voxels on the sheared grid. We then lay down the signed distance and weight functions. (c) After updating the grid, we shear it back to the original space. Note that shearing the voxel grid is simply a matter of offsetting the origin of each slice; *no voxel resampling* is performed.

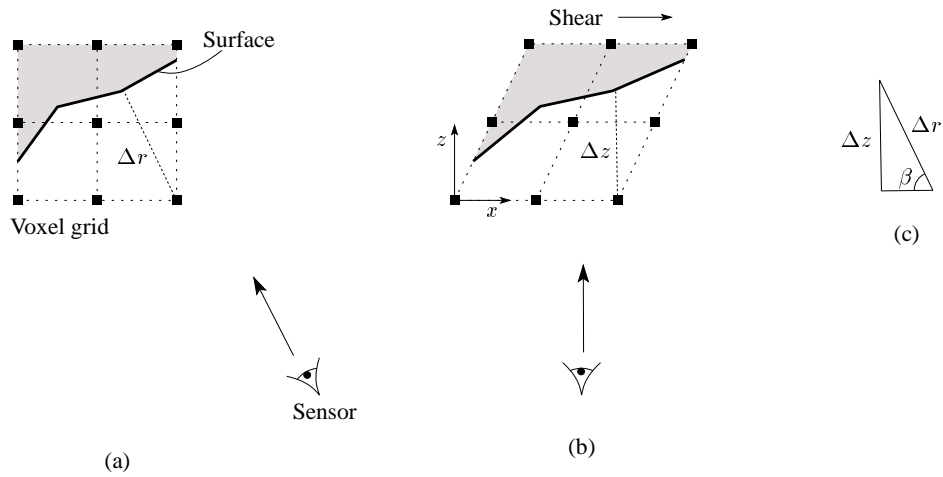


Figure 7.6: Correction factor for sheared distances. The signed distance ($d = \Delta r$) to a voxel should be taken along the line of sight from the sensor as shown in (a). After shearing the voxel grid and range image, the signed distance corresponds to the differences in z-depth for the voxel and range sample as shown in (b). The error may be corrected by a constant factor. In two dimensions, (c) indicates the correction factor would be $\Delta r = \Delta z / \sin \beta$, where β is the angle between the original view direction and the sheared view direction.

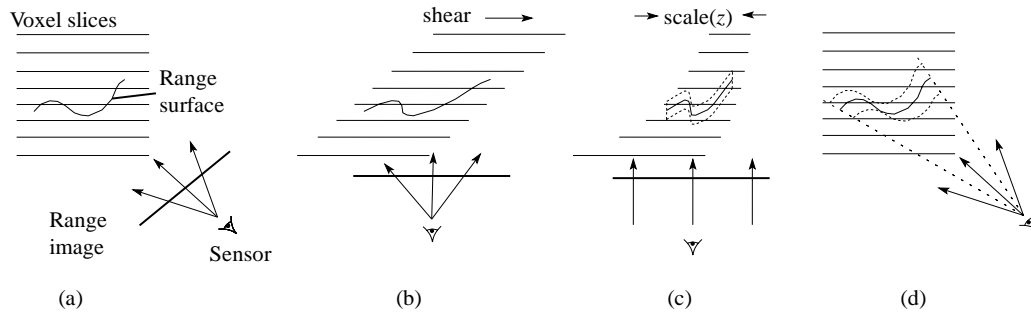


Figure 7.7: Shear-warp for perspective projection. (a) The range surface and sensor lines of sight are not initially aligned with the voxel grid. By shearing the voxel grid and range surface (b), followed by a depth dependent scale (c), we “straighten” the sensor rays with respect to the voxel grid. (d) After updating the grid, we “unscale” and “unshear” it back to the original space.

distance between the voxel and the range surface. Due to the shear, this distance must be corrected by a multiplicative factor as depicted in Figure 7.6.

Shear warp factorizations may be adapted to other range imaging frustums as well. Figure 7.7 shows how a perspective transformation can be decomposed into a shear and a scale. Again, the voxel lattice is never resampled; the shear and scale only serves to indicate how voxels map onto the resampled range image plane. The differences between voxel depths and resampled range depths again correspond to signed distances between the voxel and the range surface. As with the orthographic case, a correction factor is necessary due to the differences between the projection direction and viewing rays. This correction factor is not constant over all viewing rays, but it is constant along each viewing ray. Thus, the correction factor may be stored at each resampled range image pixel.

More complex imaging frustums such as the line perspective of Figure 5.2f will require more complex transformations, but the principle of doing modified z comparisons is still valid and leads to an efficient algorithm with the help of the binary depth tree described in the next section.

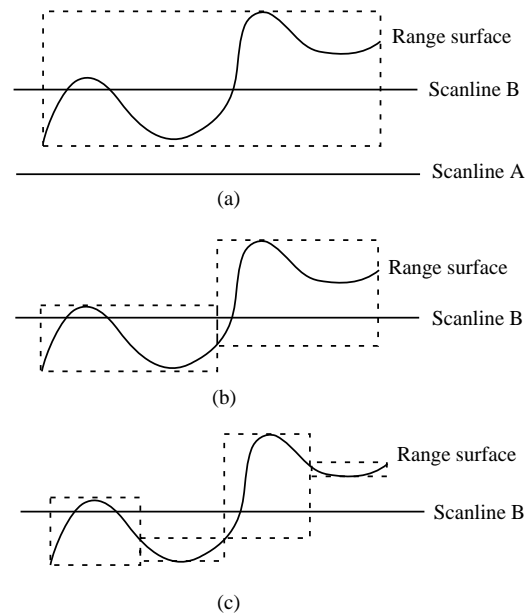


Figure 7.8: Binary depth tree. Each pair of resampled range image scanlines is entered into a binary depth tree. (a) Level 0: a bound is set on the whole range surface. Scanline A is well in front of the bounds and is not processed. Scanline B intersects and forces further traversal of the tree. (b) Level 1: the surface is split in two and yields tighter bounds. Still, both sides must be traversed further. (c) Level 2: the surface is quartered and scanline B is found to intersect the first and third quarters.

7.2.5 Binary depth trees

We can take advantage of the fact that z values are constant at each voxel scanline in order to process the voxels efficiently. In the case of merging range data only in the vicinity of the surface, we try to avoid processing voxels distant from the surface. To that end, we construct a binary tree of minimum and maximum depths for every adjacent pair of resampled range image scanlines. The trees must span pairs of range scanlines, because voxel scanlines may fall between range scanlines, and linear interpolation requires simultaneously processing two neighboring scanlines. Figure 7.8 illustrates the binary tree for three levels in two dimensions. Before processing each voxel scanline, we query the binary tree to decide which voxels, if any, are near the range surface. In figure 7.8a, scanline A lies completely outside of the range tree and thus requires no processing. Scanline B on the other hand does intersect the tree, so we proceed down the levels of the tree until we establish which portions of the scanline need to be updated. In a similar fashion, the depth tree can be traversed in a

manner that rapidly indicates what sections of a scanline are likely to be empty. The resulting speed-ups from the binary tree are typically a factor of 15 without carving, and a factor of 5 with carving.

When using the more complex viewing frustums such as line perspective, the voxel scanlines may map onto more than two range image scanlines. In this case, the domain of the binary tree is widened to span as many scanlines as necessary.

7.2.6 Efficient RLE transposes

As described in Figure 7.4, if the scanlines of the volume are badly aligned with the range image scanlines, it may be necessary to transpose the direction of the scanlines. Without optimizations, this transpose would require $O(n^3)$ operations for a volume n voxels on a side. To avoid this $O(n^3)$ cost, the solution is to work primarily on the varying voxels and to create the transposed volume directly in RLE form without ever expanding it in an intermediate step. This objective is very similar to the one for rotation of the RLE spacetime images described in Chapter 4. Indeed, the transpose is very much like a rotation by 90 degrees. The key differences are: (1) no reconstruction and resampling is required, and (2) there are two values for constant runs (unseen and empty) instead of one (zeroes). The first difference simplifies the task, while the second complicates it. In the RLE rotation algorithm, when a run of varying type began where there had been none before on a target scanline, then the prior run on the target scanline was deduced to be a constant run of zeroes, and could be updated accordingly. As a result, we could stream through only the varying runs in the source image, and ignore the constant runs. However, when more than one constant run type is possible, then the constant runs require further attention.

Fortunately, by tracking two source scanlines simultaneously, we can overcome this difficulty. As before, we construct the target scanlines as we stream through the source scanlines. This time, however, each target scanline must keep track of values (empty or unseen) when building constant runs. As long as the runs in the source scanline are the same as the current runs in the target scanlines, we would like to skip to the interesting voxels. When the type of run in the source scanline does differ from the type in the target scanline, then the target needs to be updated and a new run begun. By simultaneously streaming through

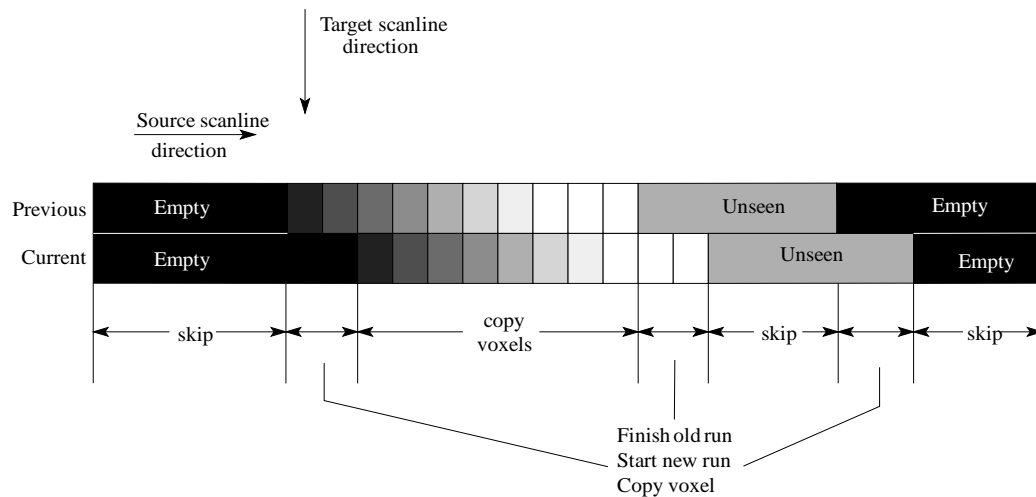


Figure 7.9: Fast transpose of a multi-valued RLE image. The source scanline direction runs horizontally and the target direction runs vertically. We stream through the current and previous source scanlines simultaneously. We can skip over intervals where scanlines have constant runs of the same value, as indicated with the first “empty” run. When the runs differ, then the target scanline must be finished with its run, so we compute the length of the concluded run, and begin a new one. When the runs are both of varying type, then the varying voxels are simply copied into the target runs.

the current and the *previous* source scanline, we can deduce when the source is different from the target, requiring some work to be done. Figure 7.9 illustrates the fast transpose algorithm.

7.3 Fast surface extraction

To generate our final surfaces, we employ a Marching Cubes algorithm [Lorenson & Cline 1987] with a lookup table that resolves ambiguous cases [Montani et al. 1994]. To reduce computational costs, we only process voxels that have varying data or are at the boundary between empty and unseen. A practical consequence of using the hole filling approach is the generation of spurious components where the lines of sight carved around unknown regions that are not connected to the observed surface. It is a straightforward matter to remove these components. In practice, we typically work with models that consist of a single, large connected component. In this case, it suffices to extract the largest connected component.

m	Number of samples on a side for a range image (m^2 samples)
p	Number of range images
n	Number of voxels on a side for a cube shaped volume (n^3 voxels)
Δ	Voxel resolution in meters
b	Width of the signed distance ramp in meters
\hat{b}	Width of the signed distance ramp in voxels (b/Δ voxels)
A	Surface area of the visible portions of the object in square meters

Table 7.1: Symbol definitions for complexity analysis.

7.4 Asymptotic Complexity

The optimizations described in this chapter serve the purpose of improving memory performance, but they also significantly reduce the asymptotic complexity of both storage and computation. Before studying the algorithm's complexity, we need to define a few symbols as shown in Table 7.1. In the remainder of this section, we assume that the voxel resolution, Δ , and ramp widths, b and \hat{b} , are fixed, and that n grows only in proportion to the size of the object being reconstructed.

For comparison purposes, we first consider a non-incremental algorithm without optimizations. The non-incremental aspect means that all of the range images need to be processed at the same time. Since each range image contains m^2 samples and yields no more than $2m^2$ triangles after tessellation to create the range surface, the overall storage is $O(pm^2)$ for the range data. Without compression, another $O(n^3)$ storage is required to represent the volume, giving an overall storage cost of $O(pm^2 + n^3)$. As for computational complexity, a brute force algorithm without any spatial data structure for visiting relevant voxels would execute in time proportional to the number of voxels for each range image plus the number of samples in each range image, i.e., $O(m^2 + n^3)$, leading to a total time complexity of $O(pm^2 + pn^3)$.

In the remainder of this section, we show that the fast algorithm does significantly better than the brute force approach. We begin with the storage complexity of the algorithm followed by an analysis of the computational complexity.

7.4.1 Storage

To analyze storage complexity, we first consider the costs of storing the original range images as well the resampled range images and their depth tree data structures. Next we examine the storage requirements for the RLE volume with and without space carving. Finally, we compute the storage costs of the reconstructed surface and compare it to the volumetric storage costs.

As described above, each range image contains m^2 samples resulting in no more than $2m^2$ triangles after tessellation. Because the volumetric algorithm is incremental, we need not hold all range images in memory at once, so the storage cost for manipulating the range images is $O(m^2)$. Before merging the range surface into the volume, it is resampled at voxel resolution. This resampled range image requires $O(n^2)$ storage. In addition, a binary tree is associated with each scanline of the resampled range image. After summing over the nodes of one tree, we find that it holds no more than $2n$ nodes, leading to a total of $2n^2$ nodes over the whole resampled range image. Thus, the storage cost for the resampled range image and its binary trees is $O(n^2)$.

When reconstructing the observed portions of the surface without space carving, the surface is effectively “blurred” into the volume by the signed distance ramps. This blurred surface occupies a volume of roughly $V = bA$, which translates to bA/Δ^3 or $\hat{b}A/\Delta^2$ voxels that must be stored. The RLE representation requires additional storage for the run lengths. If the average number of intersections of the surface with each voxel scanline is c_{\cap}^{surf} , then $(1 + 2c_{\cap}^{surf})n^2$ run lengths are necessary. The overall storage cost for the volumetric data structure is then $O(\hat{b}A/\Delta^2 + (1 + 2c_{\cap}^{surf})n^2)$. For objects that do not have an unusually high surface area to volume ratio (i.e., objects without many folds or spiny projections), then $A/\Delta^2 \sim n^2$ and the number of voxels required is proportional to $\hat{b}n^2$. Thus, for non-pathological surfaces, the storage cost for regions near the observed surface is $O(n^2)$.

The addition of space carving to the algorithm has the potential of greatly increased storage costs. When a sequence of voxels are all labeled empty, they are compactly stored as a single run of empty voxels; however, the examples in Figure 7.10 illustrate some pathological cases that defy efficient storage. The objects in this figure have highly complex geometry (7.10a) or extreme variations in surface reflectance (7.10b) that can lead to the creation of

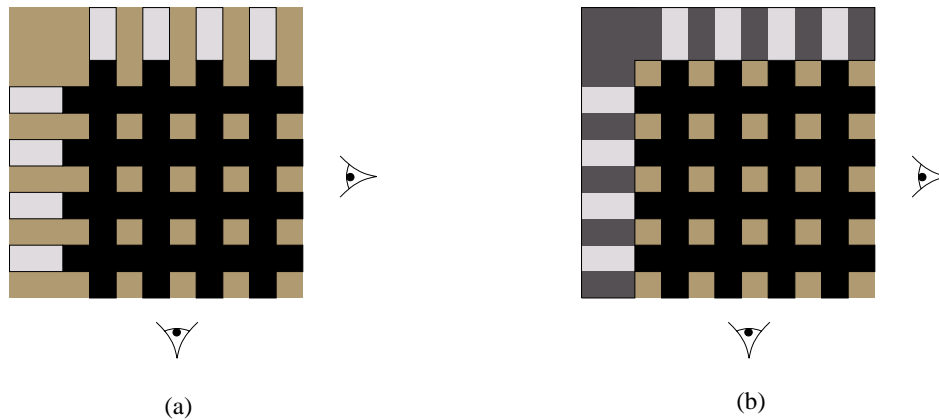


Figure 7.10: Carving from “difficult” surfaces. (a) The scene contains multiple objects shown in gray. Black regions are seen to be empty. After scanning from two viewpoints, many unseen “islands” form. (b) The same as (a), but now there is a single object with regions of negligible reflectance, shown in dark gray. The sensor cannot digitize these dark portions of the surface, and space carving from observed surfaces again leads to a fragmented volume.

many thin shafts of emptiness when carving away from the observed surface. The intersections of these shafts can lead to many separate unknown regions. This high degree of inhomogeneity leads to a worst case storage requirement of $O(n^3)$.

Nevertheless, many objects of interest do not exhibit such complexity in geometry or variations in surface reflectance. More “accessible” objects, i.e., objects having large connected visible portions, lead to a much more efficient representation. In practice, experiments with several objects of moderate complexity show that the storage requirements do not rise appreciably when including the space carving.

Note that the use of a backdrop can have an appreciable effect on the storage complexity. Consider the example in Figure 7.11a. Even though the scene being scanned is fairly simple, the number of unseen “islands” can increase rapidly with the number of scans. However, by performing only two scans with a backdrop, as shown in Figure 7.11b, these islands do not appear.

In the last step of the algorithm, we perform an isosurface extraction using an efficient Marching Cubes algorithm. By processing the run length encoded data structure without expanding it into the full volume, the cost of storing the volume remains the same as above. The resulting isosurface will have roughly A/Δ^2 vertices and $2A/\Delta^2$ faces. In practice,

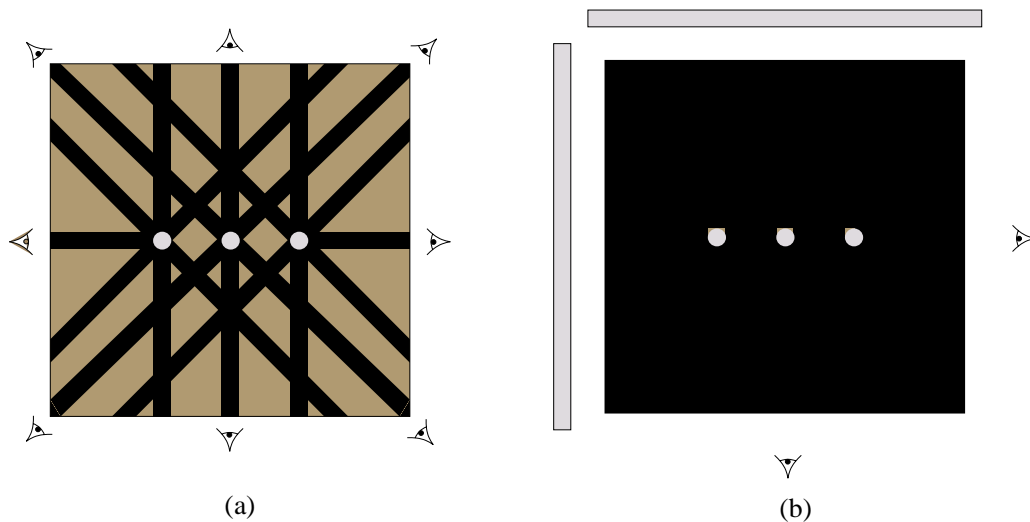


Figure 7.11: Storage complexity with and without backdrops in 2D. Three circles are being scanned indicated as the gray regions. (a) After taking 8 scans without a backdrop, a large number of unseen islands appear. These will result in high storage costs. In fact, more scans can actually increase the fragmentation. (b) Using a backdrop, only two scans are necessary to declare most of the space around the object to be empty.

we have found that the storage required for the RLE volume is comparable to the storage required for the extracted isosurface.

In summary, for non-pathological cases, the storage requirements for the fast volumetric algorithm are $O(m^2 + n^2)$. This complexity is clearly superior to the storage requirement of $O(pm^2 + n^3)$ for a non-incremental, uncompressed algorithm.

7.4.2 Computation

The key operations that influence the computational complexity of the volumetric method are:

- tessellating and resampling the range images
- building the binary depth trees
- performing volume transposes
- finding relevant voxels to update

- merging runs of voxels
- extracting the isosurface.

We address each of these in order.

In converting from a range image to a range surface, each sample is considered for creating triangles with its nearest neighbors. Thus, the tessellation requires time proportional to the number of samples, $O(m^2)$. Each range surface is resampled at the resolution of the voxel grid before merging into the volume. This step requires $O(m^2 + n^2)$ time to prepare the triangles for rasterization and $O(m^2 + n^2)$ to resample and the range image. Overall, the computational complexity is $O(m^2 + n^2)$ to tessellate and resample the range image.

After resampling the range image, we construct binary depth trees at each scanline. Constructing each depth tree requires work proportional to the number of nodes in the tree, i.e., $O(n)$. For n scanlines, the time complexity is $O(n^2)$.

When the voxel scanlines are not oriented in a direction that is desirable for efficient memory traversal, it is necessary to transpose the volume. The fast transpose algorithm performs work in traversing the RLE data structures in both the current and the transposed directions, in addition to the work of copying over voxels. Managing the data structures takes $O(2(1 + c_{\hat{n}}^{surf})n^2)$ time, while copying over the voxels requires $O(\hat{b}A/\Delta^2)$ time. The overall transpose time complexity is then $O(2(1 + c_{\hat{n}}^{surf})n^2 + \hat{b}A/\Delta^2)$. For non-pathological cases, the complexity of the transpose operation is $O(n^2)$.

Once the volume is transposed for optimal scanline traversal, we query the binary depth trees to decide which voxels require updating. In the case of reconstructing the observed portions of the surface, this amounts to deciding which voxels are near the range surface being merged. We can think of the surface as being sampled at voxel resolution and “blurred” along the sensor lines of sight by the signed distance ramps. Thus, as many as $\hat{b}n^2$ voxels may require updating. The cost of finding that a single voxel requires updating is $\log n$, i.e., the cost of traversing the binary tree down to a single leaf node. For a run of voxels spanning an interval of leaf nodes in the tree, the cost of finding the consecutive leaf nodes is amortized over the interval, since the tree is not re-traversed for each new voxel. Still, in the worst case, each voxel near the range surface requires $\log n$ time to be found, yielding an overall complexity of $O(n^2 \log n)$.

When performing space carving, the cost of locating which voxels should be marked as empty is a function of the complexity of the emptiness shafts. We define c_{\cap}^{shaft} to be the average number of shaft intersections per scanline per range image. The cost of finding the interval of emptiness per scanline is then $O(c_{\cap}^{shaft} \log n)$, leading to an overall complexity of $O(c_{\cap}^{shaft} n^2 \log n)$. The constant, c_{\cap}^{shaft} , can actually be quite large as shown in Figure 7.10, but as indicated in the previous section, the shafts are usually small in number leading to small values of c_{\cap}^{shaft} for non-pathological objects and an effective complexity of $O(n^2 \log n)$.

Once the relevant voxels have been identified with the binary depth tree, the runs of signed distances and emptiness must be merged with the existing runs in the volume. The work required for this step is proportional to the number of runs and the number of non-constant voxels that are already in the volume plus the number that require updating. If the average number of intersections of a range surface with each scanline is c_{\cap}^{range} , then the amount of work required to merge runs near the observed surface is $O(\hat{b}A/\Delta^2 + (2 + 2c_{\cap}^{shaft} + 2c_{\cap}^{range})n^2 + \hat{b}n^2)$. Note that because we are using a double-buffered volume, i.e., we copy over all untouched voxels to maintain memory locality, the merge step always requires at least $O(\hat{b}A/\Delta^2)$ time to execute. For a non-pathological surface, the overall time complexity for merging runs near the observed surface is $O(n^2)$.

When merging the runs of emptiness into the volume, the argument still holds that the work required is proportional to the number of runs and the number of non-constant voxels already in the volume and about to be merged. We define $c_{\cap}^{unseen}(i)$ to be the average number of intersections of unseen regions with each scanline after merging i scans. Merging the runs of emptiness derived from the i th range scan will then require $O((2c_{\cap}^{unseen}(i) + 2c_{\cap}^{shaft}(i) + 1)n^2 + \hat{b}A/\Delta^2)$ for each range image. If we let $c_{carve} = \text{MAX}(2c_{\cap}^{unseen}(i) + 2c_{\cap}^{shaft}(i) + 1)$, then the total complexity of merging the empty regions is no worse than $O(c_{carve} n^2 + \hat{b}A/\Delta^2)$. As indicated in the previous section, c_{carve} can be very large, but for non-pathological objects and suitable use of backdrops, c_{carve} is typically small, leading to an overall time complexity of $O(n^2)$ for non-pathological objects when merging runs during the carving step.

All of the discussion of time complexity up to this point has been based on merging a single range image into the volume. For p range images, each of the complexities should be

multiplied by p , except for the number of transposes which depends on the order of merging scans. If the object is scanned from all sides, then by selecting the order of merging the scans, the number of transposes need not exceed two: one transpose from the first scanline direction to the second plus one transpose from the second direction to the third. In the worst case, a transpose is required for every range image, which is still no more than p . Thus, the overall complexity for merging range images into the volume is $O(pm^2 + pn^2 \log n + pA/\Delta^2)$. For non-pathological objects, this becomes $O(pm^2 + pn^2 \log n)$.

The final step of the surface reconstruction algorithm is to extract an isosurface from the volume. By visiting only the voxels that are near the surface, this algorithm operates in $O(\hat{b}A/\Delta^2)$ time or $O(n^2)$ for the non-pathological case.

In summary, for non-pathological objects the overall time complexity for merging the observed portions of the surface is $O(pm^2 + pn^2 \log n)$. In practice, we have determined that the logarithmic term is typically overwhelmed by other factors, leading to an observed complexity of $O(pm^2 + pn^2)$. This complexity is a significant improvement over the worst case complexity of $O(pm^2 + pn^3)$ for the brute force algorithm. At the time of publication of this thesis, the computational optimizations for the space carving algorithm have not yet been implemented. However, as long as the volume does not become heavily fragmented, the optimized approach is expected to behave asymptotically as well as the algorithm that does not employ space carving.

Chapter 8

Results of the volumetric method

In this chapter, we describe the hardware used to acquire the range data and how we treat the range scanner's lines of sight (Section 8.1). In Section 8.2, we explain our method for addressing the problem of aligning range images. Finally, we demonstrate the effectiveness of the volumetric method on several models (Section 8.3).

8.1 Hardware Implementation

The data used in this chapter was acquired using the Cyberware 3030 MS laser stripe optical triangulation scanner, as described in Chapter 4. We collected data both using the Cyberware's traditional triangulation method and using the spacetime analysis (by way of the JPEG compressor board as shown in Figure 4.1).

When using traditional triangulation analysis implemented in hardware in our Cyberware scanner, the uncertainty in triangulation for our system follows the lines of sight of the expanding laser beam as described in Section 5.2. When using the spacetime analysis, however, the uncertainty roughly follows the lines of sight of the CCD camera. For each method of triangulation analysis, we adhere to the appropriate lines of sight when laying down signed distance and weight functions. The space carving, however, only follows the lines of sight of the laser. Owing to the geometry of the Cyberware scanner, the lines of sight of the laser are significantly simpler to follow than those of the CCD camera. The decision to carve from the point of view of the laser is not a fundamental limitation of the algorithm,

merely a matter a convenience for the implementation. To maximize the amount of possible space carving, it remains an area for future work to follow the lines of sight of the CCD camera.

8.2 Aligning range images

As described in Chapter 5, proceeding with pairwise alignment while walking around an object may yield good results at each stage, but the errors will accumulate. The general solution is to minimize the alignment errors among all of the range images simultaneously. Only recently are solutions to this total alignment problem emerging [Bergevin et al. 1996] [Stoddart & Hilton 1996].

For the results obtained in this chapter, we devised and implemented a practical solution that utilizes information from the scanner's motion control system. The Cyberware scanner described in the previous section has a rotational degree of freedom about the vertical axis. By calibrating the position and orientation of this rotational axis, we can perform a set of scans, with a specified rotation between each scan, and begin with good alignment information for this set of scans. After merging these scans, the resulting isosurface will usually have good coverage of the object so that it may be used as an anchor for future alignments (using the method of [Turk & Levoy 1994]). As scans are aligned and merged, new isosurfaces can be extracted to serve as better anchors - better in the sense of more surface coverage and in the sense of improved surface estimation. Usually, two or more additional scans are immediately required after the initial set of rotations to capture the top and bottom of the object. If these scans are well chosen, they will overlap the existing isosurface well enough to perform pairwise alignment while providing enough new data to offer an anchor for future alignments against the top and bottom of the object.

We do not claim that this practical procedure is optimal. In fact, the alignment results will depend on the order in which scans are merged. Nevertheless, the measurable quality of the results indicate that the procedure is viable and accurate for our scanning system.

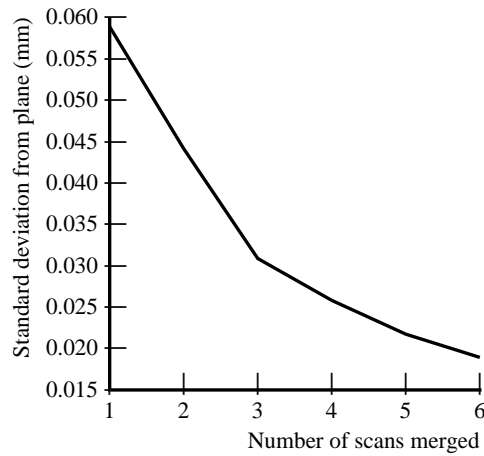


Figure 8.1: Noise reduction by merging multiple scans. A planar target was scanned 6 times with a 15° rotation of the viewpoint after each scan. Standard deviation from planarity for the reconstruction was determined after merging each scan volumetrically. Note how each scan improves the estimate of the shape of the target.

8.3 Results

We show results for a number of objects designed to explore noise reduction, robustness of our algorithm, its ability to fill gaps in the reconstruction, and its attainable level of detail.

To explore the noise reduction properties of our algorithm, we scanned a planar target from 6 different viewpoints. After merging each scan into the volume, we extracted an iso-surface, fit a plane through this surface, and computed the standard deviation of the reconstructed vertices from the planar fit. Figure 8.1 shows the results of this procedure. Clearly, after each scan is merged, the planar fit improves, indicating a reduction in noise.

To explore robustness, we scanned a thin drill bit (about the thickness of the laser sheet) from 12 orientations at 30 degree spacings using the traditional method of optical triangulation. Due to the false edge extensions inherent in data from triangulation scanners using traditional analysis (see Figure 4.11b), this particular object poses a formidable challenge. The rendering of the drill bit reconstructed by zippering range images [Turk & Levoy 1994] shows the catastrophic outcome typical of using a polygon-based approach. The model generated by the volumetric method, on the other hand, is without holes and preserves some of the helical structure of the original object, even though this structure is near the resolution

limit of the scanner.

To demonstrate the effectiveness of carving space for hole filling, we show the stages of our algorithm when reconstructing the dragon model in Figures 8.3 and 8.4. In the first stage, we confine the signed distance ramps and weight functions to the vicinity of the observed surface. The result is a reconstruction with holes where we failed to see the surface. In the second stage, we follow the laser lines of sight away from the observed surface and “empty out” much of the space around the dragon. The resulting isosurface indicates some success in filling holes, but a number of undesirable protrusions have been generated. These excess surfaces are the result of insufficient carving of space. In the third stage, we follow up with some additional scans using a backdrop to carve through sections of the model. This results in the removal of the extraneous regions, but the hole fill regions are still jagged due to aliasing in the transitions between unseen and empty. In the final stage, we filter the mesh to smooth the hole fill regions. This filtering applies only to the hole fill regions while preserving the detail in the observed portions of the surface.

The “Happy Buddha” in Figures 8.5 and 8.6 shows that our method can be used to generate very detailed, hole-free models. From a set of 48 range images, we generated the model shown in Figure 8.6a. This model has gaps which we were able to fill with space carving and an additional 10 scans against a backdrop. The final model contains over 2.5 million triangles, which we decimate to 800,000 triangles without appreciable loss of detail using the method of [Schroeder & Lorensen 1992]. The rendering in Figure 8.6b, made using RenderMan and the decimated mesh, incorporates a number of rendering algorithms including accessibility shading and simple simulation of layered surface scattering. Because the computer model is free of holes and self-intersecting surfaces, we successfully manufactured a hardcopy using stereolithography (Figure 8.6c). For a more detailed description of the stereolithography process, refer to Appendix B. Figure 8.7 shows both wireframe and shaded renderings of a single range surface, the reconstructed surface, and the decimated mesh. The reconstruction from multiple range surfaces is less noisy and more detailed than a single range surface. The number of triangles generated, however, is more than necessary. In the figure, a 3:1 decimation approximates the reconstruction without appreciable loss of detail.

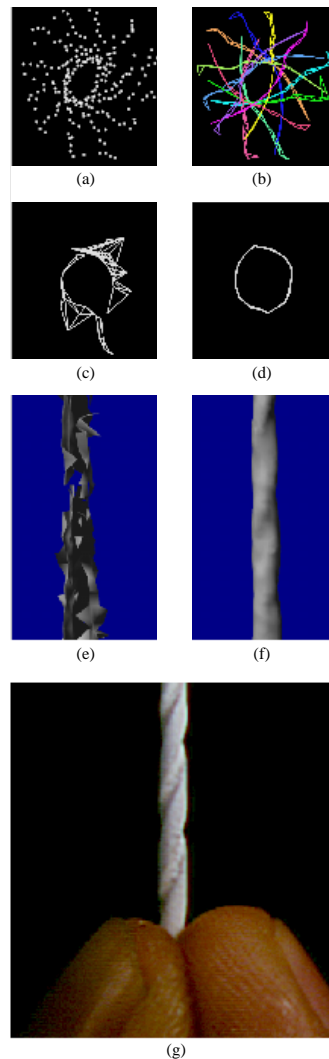


Figure 8.2: Merging range images of a drill bit. We scanned a 1.6 mm drill bit from 12 orientations at a 30 degree spacing using traditional optical triangulation methods. Illustrations (a) - (d) each show a plan (top) view of a slice taken through the range data and two reconstructions. (a) The range data shown as unorganized points: algorithms that operate on this form of data would likely have difficulty deriving the correct surface. (b) The range data shown as a set of wire frame tessellations of the range data: the false edge extensions pose a challenge to both polygon and volumetric methods. (c) A slice through the reconstructed surface generated by a polygon method: the zippering algorithm of [Turk & Levoy 1994]. (d) A slice through the reconstructed surface generated by the volumetric method described in this thesis. (e) A rendering of the zippered surface. (f) A rendering of the volumetrically generated surface. Note the catastrophic failure of the zippering algorithm. The volumetric method, however, produces a watertight model. (g) A photograph of the original drill bit. The drill bit was painted white for scanning.

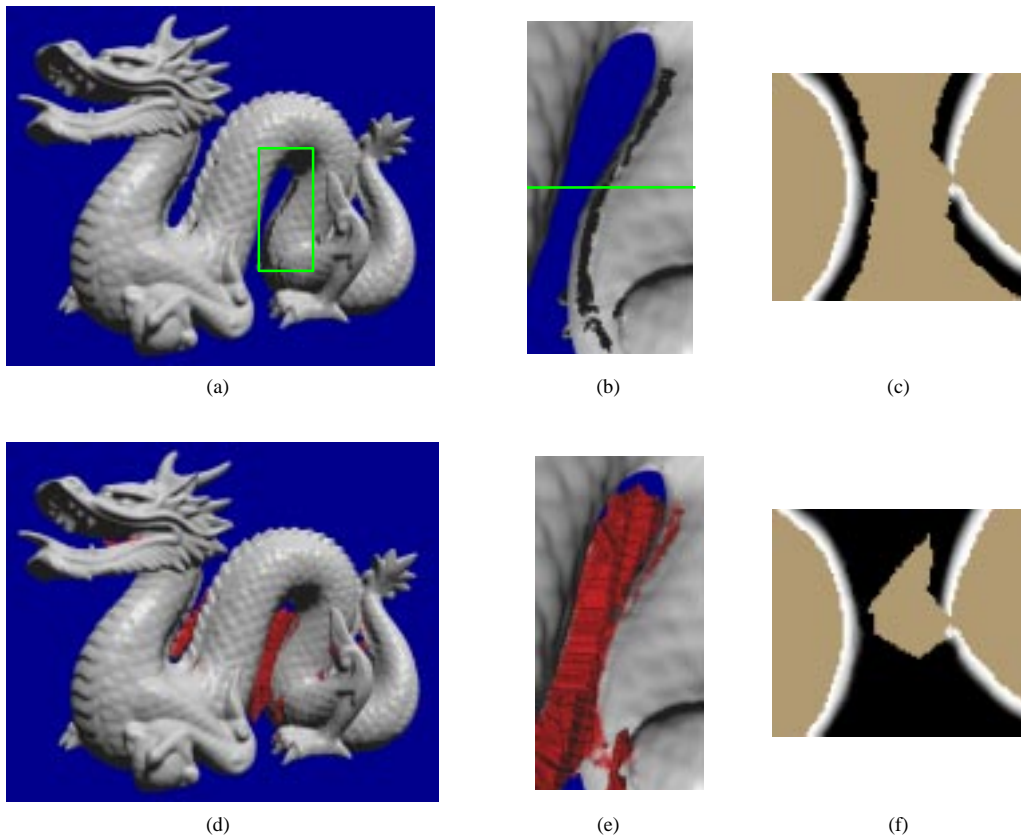


Figure 8.3: Reconstruction of a dragon – Part I of II. Illustrations (a) and (d) are full views of the dragon. Illustrations (b) and (e) are magnified views of the section highlighted by the green box in (a). Regions shown in red correspond to hole fill triangles. Illustrations (c) and (f) are slices through the corresponding volumetric grids at the level indicated by the green line in (b). (a)-(c) Reconstruction from 61 range images without space carving and hole filling. The magnified rendering highlights the holes in the belly. The slice through the volumetric grid shows how the signed distance ramps are maintained close to the surface. The gap in the ramps leads to a hole in the reconstruction. (d)-(f) Reconstruction with space carving and hole filling using the same data as in (a). While some holes are filled in a reasonable manner, some large regions of space are left untouched and create extraneous tessellations. The slice through the volumetric grid reveals that the isosurface between the unseen (brown) and empty (black) regions will be connected to the isosurface extracted from the distance ramps, making it part of the connected component of the dragon body and leaving us with a substantial number of false surfaces.

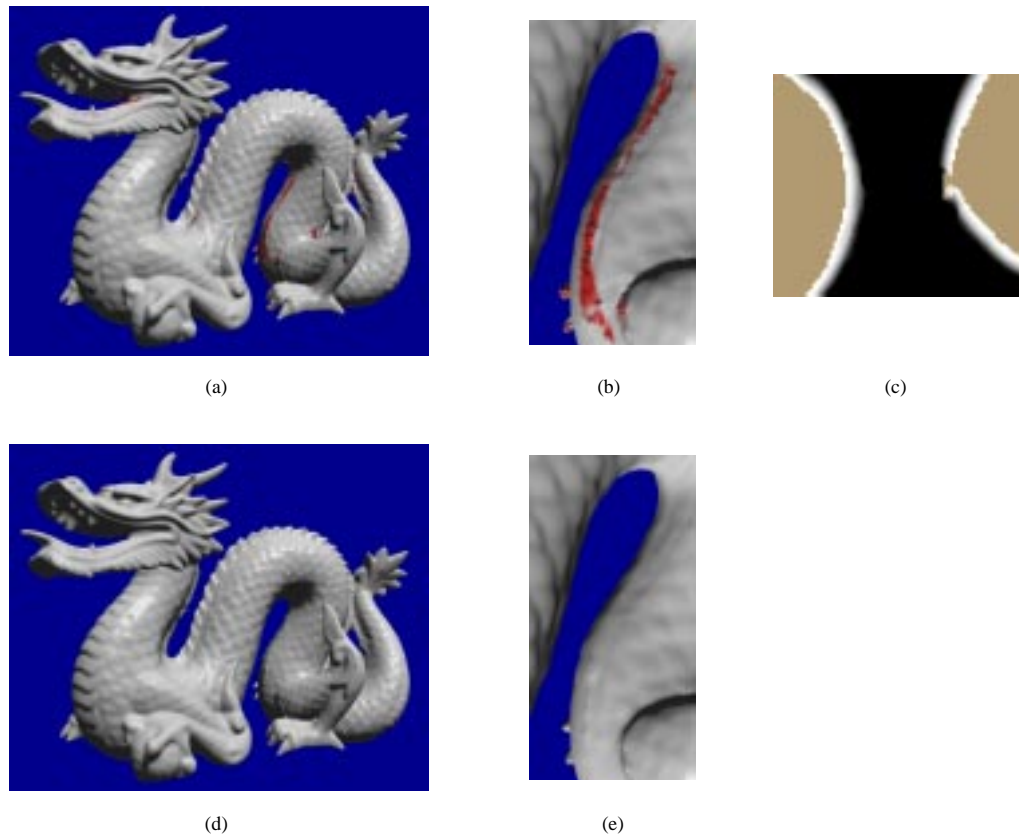


Figure 8.4: Reconstruction of a dragon – Part II of II. Following Figure 8.3, (a) and (d) are full views of the dragon, (b) and (e) are magnified views of the belly, and (c) is a slice through the volumetric grid. (a)-(c) Reconstruction with 10 additional range images using “backdrop” surfaces to effect more carving. Notice how the extraneous hole fill triangles nearly vanish. The volumetric slice shows how we have managed to empty out the space near the belly. The bumpiness along the hole fill regions of the belly in (b) corresponds to aliasing artifacts from tessellating over the discontinuous transition between unseen and empty regions. (d) and (e) Reconstruction as in (a) and (b) with filtering of the hole fill portions of the mesh. The filtering operation blurs out the aliasing artifacts in the hole fill regions while preserving the detail in the rest of the model. Careful examination of (e) reveals a faint ridge in the vicinity of the smoothed hole fill. This ridge is actual geometry present in all of the shaded renderings, in this and the previous. The final model contains 1.8 million polygons and is watertight.



Figure 8.5: From the original to a 3D hardcopy of the “Happy Buddha” – Part I of II. (a) The original is a plastic and rosewood statuette that stands 20 cm tall. (b) Photograph of the original after spray painting it matte gray to simplify scanning. (c) Gouraud-shaded rendering of one range image of the statuette. Scans were acquired using a Cyberware scanner, modified to permit spacetime triangulation. This figure illustrates the limited and fragmentary nature of the information available from a single range image.



Figure 8.6: From the original to a 3D hardcopy of the “Happy Buddha” – Part II of II. (a) Gouraud-shaded rendering of the 2.4 million polygon mesh after merging 48 scans, but before hole-filling. Notice that the reconstructed mesh has at least as much detail as the single range image, but is less noisy; this is most apparent around the belly. The hole in the base of the model corresponds to regions that were not observed directly by the range sensor. (b) RenderMan rendering of an 800,000 polygon decimated version of the hole-filled and filtered mesh built from 58 scans. By placing a backdrop behind the model and taking 10 additional scans, we were able to see through the space between the base and the Buddha’s garments, allowing us to carve space and fill the holes in the base. (c) Photograph of a hardcopy of the 3D model, manufactured by 3D Systems, Inc., using stereolithography. The computer model was sliced into 500 layers, 150 microns apart, and the hardcopy was built up layer by layer by selectively hardening a liquid resin. The process took about 10 hours. Afterwards, the model was sanded and bead-blasted to remove the stair-step artifacts that arise during layered manufacturing.

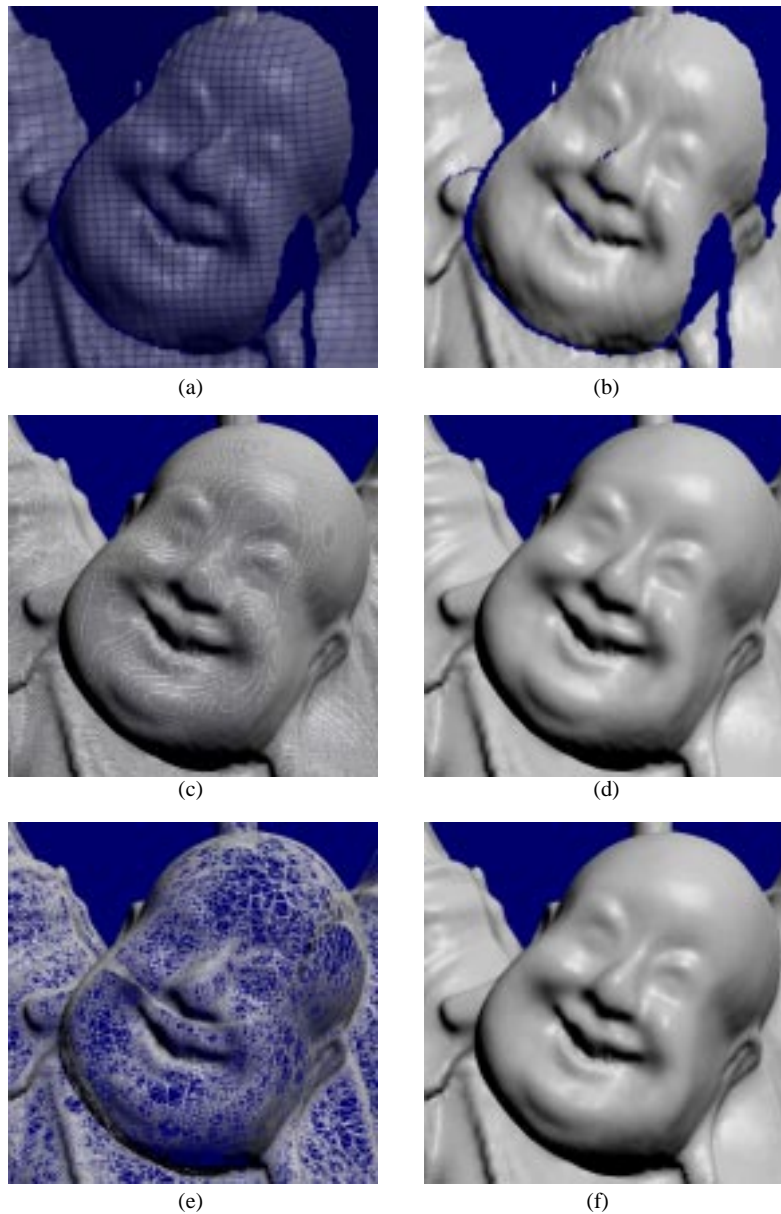


Figure 8.7: Wireframe and shaded renderings of the Happy Buddha model. (a) and (b) Wireframe and shaded rendering of a single range surface. (c) and (d) Wireframe and shaded rendering of the 2.6 million triangle reconstruction. The contours in the wireframe correspond to small triangles created when the isosurface clips the edges and corners of voxel cubes. The shaded rendering demonstrates noise reduction and increased detail after multiple scans are combined. (e) and (f) Wireframe and shaded rendering of the 800,000 triangle decimated mesh. The decimation process effectively collapses nearly coplanar triangles into larger triangles following the method of [Schroeder & Lorensen 1992].

Model	Scans	Input triangles	Voxel size (mm)	Volume dimensions	Exec. time (min.)	Output triangles	Holes
Dragon	61	15 M	0.35	712x501x322	56	1.7 M	324
Dragon + fill	71	24 M	0.35	712x501x322	257	1.8 M	0
Buddha	48	5 M	0.25	407x957x407	47	2.4 M	670
Buddha + fill	58	9 M	0.25	407x957x407	197	2.6 M	0

Table 8.1: Statistics for the reconstruction of the dragon and Buddha models, with and without space carving.

Statistics for the reconstruction of the dragon and Buddha models appear in Table 8.1. With the optimizations described in the previous section, we were able to reconstruct the observed portions of the surfaces in under an hour on a 250 MHz MIPS R4400 processor. The space carving and hole filling algorithm is not completely optimized, but the execution times are still in the range of 3-5 hours, less than the time spent acquiring and registering the range images. For both models, the RMS distance between points in the original range images and points on the reconstructed surfaces is approximately 0.1 mm. This figure is roughly the same as the accuracy of the scanning technology, indicating excellent alignment and a nearly optimal surface reconstruction.

Chapter 9

Conclusion

In this thesis, we have worked from the most basic issues of a prevalent range scanning technology and progressed to a method that reconstructs complex models from vast amounts of range data. We review these contributions in Sections 9.1 and 9.2. In Section 9.3, we describe several areas for future work.

9.1 Improved triangulation

Optical triangulation has been used for decades, yet the traditional methods are fundamentally limited in the amount of accuracy they can deliver. Variations in reflectance and shape induce errors on the order of the width of the illuminant, regardless of sensor resolution. In addition, when using coherent illumination, laser speckle corrupts the imaged light reflections and contribute range error, again independent of sensor resolution. Except for very simple surfaces, the errors due to reflectance and shape variations typically dominate; at a minimum, these errors are objectionable because they are coherent.

Many optical triangulation systems sweep the illuminant across an object, leading to consecutive sensor images that record light reflecting from individual points on the object. We have shown that by analyzing the time evolution of these imaged reflections, distortions induced by shape and reflectance changes can be corrected. In theory, for an ideal orthographic sensor with infinite resolution, these errors can be eliminated completely. In

practice, we have demonstrated that we can significantly reduce range distortions with existing hardware that uses a perspective sensor of finite resolution. Although our implementation of the spacetime method does not completely eliminate range artifacts, it has proven to reduce the artifacts in all shape and reflectance experiments we have conducted. Further, increases in sensor resolution and reduction of filtering artifacts will undoubtedly improve the accuracy for spacetime analysis, while the same cannot be said for traditional optical triangulation methods. The influence of laser speckle, however, continues to limit triangulation accuracy.

9.2 Volumetrically combining range images

Optical triangulation scanning is one of a variety of rangefinder technologies that acquire sets of dense samplings known as range images. Numerous researchers have attacked the problem of reconstructing a single surface from these range images. In this thesis, we have developed a new algorithm for volumetric integration of range images, leading to a surface reconstruction without holes. The algorithm has a number of desirable properties, including the representation of directional sensor uncertainty, incremental and order independent updating, robustness in the presence of sensor errors, and the ability to fill gaps in the reconstruction by carving space. Our use of a run-length encoded representation of the voxel grid and a shear-warp factorization for the scan-conversion of range images makes the algorithm efficient. This in turn allows us to acquire and integrate a large number of range images. In particular, we demonstrate the ability to integrate up to 70 scans into a high resolution voxel grid to generate million polygon models in a few hours. These models are free of holes, making them suitable for surface fitting, rapid prototyping, and rendering.

9.3 Future work

In this section, we describe some directions for improving both optical through spacetime analysis and the volumetric method for surface reconstruction. We conclude with a discussion of some open problems in the acquisition of the shape and appearance of objects.

9.3.1 Optimal triangulation

The accuracy of the spacetime analysis hinges on reliably capturing the spacetime images. Accordingly, all efforts to enhance the quality of these images are of benefit. In terms of the sensor, higher pixel densities mean more samples in z in the spacetime images (as well as more y samples for the spacetime volume). These improved pixel densities should be accompanied by either slower scanning or higher frame rates for increased resolution in x . In addition, greater dynamic range at the sensor will allow for acquisition of surfaces with widely varying reflectances even when oriented at grazing angles to the illumination. Video digitizers with more bits per pixel will also lead to more precise representations of the spacetime images. Experimenting with different illuminants can also lead to greater accuracy. In Chapter 3, we argue that widening the laser sheet may improve results, because the spacetime impulse response acts as a bandlimiting filter. Further, the limitations due to laser speckle can be reduced with partially coherent, perhaps even incoherent illumination. In the presence of spatiotemporal aliasing, methods for registering and deblurring multiple spacetime images should also lead to improved resolution.

When a surface is very bright or shiny, surface interreflections will corrupt the spacetime image. Under these circumstances, recovering accurate range is likely to be very challenging. Research in shape from shading which accounts for surface interreflections may offer some promising avenues toward a solution [Nayar et al. 1990] [Wada et al. 1995]. In the case of shiny surfaces, the errors will depend heavily on the orientation of the surface with respect to the illumination. Acquiring multiple range images can help identify some of these errors as outliers, because they will not be corroborated by the other range images. In addition, the interreflections will tend to distort the shape of the spacetime Gaussians so that they will not behave ideally; this deviation from ideal will be detected, and the samples will be discarded or downweighted in favor of data taken from a different orientation that yields better spacetime Gaussians.

The method of acquiring and analyzing the spacetime images in Chapter 4 requires all frames to be captured and then post-processed. Ideally, we would like to perform the spacetime analysis in hardware, in realtime. Such a system could be implemented as a ring of frame buffers that store the most recent N frames, where N is determined by the time it takes

for the illuminant to traverse a point on the surface. To reduce storage costs and improve performance, the frames could be run-length encoded, and the spacetime rotation could be implemented as a shear. In the case of a scanning laser beam with a linear array sensor, the frame buffer would be small – a single array of pixels – and a hardware implementation using a high speed digital signal processing chip could be quite practical.

9.3.2 Improvements for volumetric surface reconstruction

The volumetric method described in Chapters 5-8 leads to a variety of directions for future work. Some of the issues that deserve attention are discussed in Sections 6.3 and 6.4. These include choosing better conditioning functions to minimize isosurface artifacts, modifying the algorithm to cope with thin surfaces and sharp corners, and exploring strategies for more aggressive space carving.

Space carving can also be improved to help remove outliers. Currently, the space carving algorithm is conservative in that only unseen regions may be reclassified as empty; any voxels containing a signed distance remain untouched. However, if a voxel is observed to be empty from several points of view, then it is highly unlikely to contain a surface. Recognizing such a circumstance could lead to an algorithm that is more capable of removing false range data, i.e., outliers.

We can also hope to improve the space carving method through the more traditional methods of carving from image silhouettes [Szeliski 1993]. Using geometric backdrops achieves the effect of using image silhouettes, but it has drawbacks. A range scanner can usually digitize large objects that do not fit into the field of view by moving the scanner or the object as needed. Requiring that the scanner always see a backdrop at the back of the field of view, however, makes it more difficult to scan these larger objects. In the case of optical triangulation, the backdrop must be visible to both the laser and the sensor. This means that the backdrop typically has to be positioned far enough away so that the triangulation scanner can see *around* the object. But requiring that the backdrop be far away, yet still visible to the sensor, means wasting valuable resolution, as the pixels must map to a larger field of view. The use of a separate color camera with colored or light-emitting backdrops solves these problems. As long as the backdrop is clearly distinguishable from the

object being scanned, then the distance to the backdrop is immaterial, and it can be placed conveniently outside of the working volume of the range scanner.

The hole filling algorithm can be improved by making the surface properties of filler polygons more consistent with the remainder of the surface. When scanning a surface that has a discernable texture (such as the scales of a lizard), there will be a distinct difference between the smoothed hole fill regions and the remainder of the surface. Ideally, we would like these hole fill regions to adapt to the surrounding texture, either automatically or with some user guidance. Recent work on analyzing and synthesizing image textures suggests one approach for propagating surface properties [Heeger & Bergen 1995]. If color information were also available in regions around the hole fillers, then color texture could be grafted as well.

As range scanners become faster, some approaching realtime, a reconstruction algorithm that is fast enough to keep pace also becomes very attractive. One can imagine a motorized acquisition gantry or a hand-held scanner with orientation and position sensors delivering registered range images to a system that could create a detailed model in a very short period of time. Though we have developed a number of optimizations for the volumetric algorithm to ensure good performance, we have yet to explore an increasingly important direction: parallelization. [Lacroute 1996] has parallelized the shear warp volume rendering algorithm and obtained excellent results on a shared memory multiprocessor architecture. We would expect to attain similar improvements with the fast volumetric method described in Chapter 7. One factor that should make implementation easier is the lack of front to back ordering that volume rendering requires. In the case of volumetric surface reconstruction, the voxels are updated in a manner that is completely independent of order.

9.3.3 Open problems in surface digitization

A number of important problems remain on the way to automated and hi-fidelity acquisition of the shape and appearance of the surface of an object. Among the most challenging are solving for the next best view and capturing surface reflectance properties.

The “next best view” problem may be stated as follows: given a set of range views of an object, determine the next position and orientation of the object or sensor that is likely to

maximize the knowledge about the object and the space around it. Of course, without knowing the shape of the object a priori, it is impossible to determine the next best view in terms of maximizing the visible surface area of the object. Alternative measures are necessary, and one promising measure is the surface area of the boundary surrounding the unknown regions of the space in and around the object. This area is in fact defined by the hole fill polygons computed in the volumetric algorithm described in this thesis. Initial results in solving for next best view are promising [Pito 1996], but more research is warranted.

For faithful reproduction of the appearance of objects, the surface reflectance properties must be acquired. A simple strategy would be to reconstruct the shape of an object, take a few color images, and then “paste” the color onto the object by following the lines of sight from the color camera. For overlapping views, the colors could simply be averaged together. This strategy is flawed, however, because the results are dependent on the lighting and the viewpoint. What we really want are the underlying reflectance properties over the surface of the object so that we can render the computer model under arbitrary lighting and viewing conditions. These reflectance properties can be very complex. For general anisotropic surfaces, the bi-directional reflectance distribution function (BRDF) at a point is five dimensional: 2 dimensions for each of the incoming and outgoing light directions, and one dimension for wavelength (two dimensions for wavelength if fluorescence is possible). Accounting for variations over the surface of the object, the space is seven (possibly eight) dimensional. With controlled lighting and many color images of the object, we can begin to fill this large space with data. The problem is further complicated, however, by the fact that light reflecting from the surface toward the sensor arrives at the surface not only from the light source, but from other points on the surface. Accounting for the effects of these interreflections is crucial to accurately measuring surface BRDF, which in turn requires a very accurate description of the shape of the object. Some results have been obtained for simplified BRDF's and moderate variations across the surface [Nayar et al. 1990] [Sato & Ikeuchi 1996], but the general problem remains open.

Appendix A

Proof of Theorem 5.1

Theorem 5.1

Given the integral:

$$I = \iiint h \left(x, y, z, \frac{\partial z}{\partial x}, \frac{\partial z}{\partial y} \right) dx dy dz$$

where:

$$z = f(x, y)$$

and the function h is of the form:

$$h \left(x, y, z, \frac{\partial z}{\partial x}, \frac{\partial z}{\partial y} \right) = e(x, y, z) \left[\left(-\frac{\partial z}{\partial x}, -\frac{\partial z}{\partial y}, 1 \right) \cdot \mathbf{v}(x, y, z) \right]$$

the function z that minimizes the integral satisfies the relation:

$$\mathbf{v} \cdot \nabla e + e \nabla \cdot \mathbf{v} = 0$$

Proof:

The solution lies in applying the calculus of variations, which has the fundamental result known as the Euler-Lagrange equation:

$$\frac{\partial h}{\partial z} - \frac{\partial}{\partial x} \frac{\partial h}{\partial(\partial z/\partial x)} - \frac{\partial}{\partial y} \frac{\partial h}{\partial(\partial z/\partial y)} = 0 \quad (\text{A.1})$$

We begin with the first term, $\partial h/\partial z$. We can rewrite h as:

$$\begin{aligned} h &= e \left[\left(-\frac{\partial z}{\partial x}, -\frac{\partial z}{\partial y}, 1 \right) \cdot \mathbf{v} \right] \\ &= e \left[-v_x \frac{\partial z}{\partial x} - v_y \frac{\partial z}{\partial y} + v_z \right] \end{aligned}$$

where we have dropped the explicit dependencies on (x, y, z) and where the components of \mathbf{v} are (v_x, v_y, v_z) . Then we can compute:

$$\frac{\partial h}{\partial z} = \frac{\partial e}{\partial z} \left[-v_x \frac{\partial z}{\partial x} - v_y \frac{\partial z}{\partial y} + v_z \right] + e \left[-\frac{\partial v_x}{\partial z} \frac{\partial z}{\partial x} - \frac{\partial v_y}{\partial z} \frac{\partial z}{\partial y} + \frac{\partial v_z}{\partial z} \right] \quad (\text{A.2})$$

Next, we compute the intermediate partials:

$$\frac{\partial h}{\partial(\partial z/\partial x)} = -ev_x$$

and:

$$\frac{\partial h}{\partial(\partial z/\partial y)} = -ev_y$$

The remaining partials are then:

$$\begin{aligned} \frac{\partial}{\partial x} \frac{\partial h}{\partial(\partial z/\partial x)} &= -\frac{\partial(ev_x)}{\partial x} - \frac{\partial z}{\partial x} \frac{\partial(ev_x)}{\partial z} \\ &= -v_x \frac{\partial e}{\partial x} - e \frac{\partial v_x}{\partial x} - \frac{\partial z}{\partial x} \left[v_x \frac{\partial e}{\partial z} + e \frac{\partial v_x}{\partial z} \right] \end{aligned} \quad (\text{A.3})$$

and:

$$\begin{aligned}
\frac{\partial}{\partial y} \frac{\partial h}{\partial(\partial z / \partial y)} &= -\frac{\partial(e v_y)}{\partial y} - \frac{\partial z}{\partial y} \frac{\partial(e v_y)}{\partial z} \\
&= -v_y \frac{\partial e}{\partial y} - e \frac{\partial v_y}{\partial y} - \frac{\partial z}{\partial y} \left[v_y \frac{\partial e}{\partial z} + e \frac{\partial v_y}{\partial z} \right]
\end{aligned} \tag{A.4}$$

Substituting Equations A.2, A.3, and A.4 into the Euler-Lagrange equation (Equation A.1), we arrive at:

$$v_z \frac{\partial e}{\partial z} + e \frac{\partial v_z}{\partial z} + v_x \frac{\partial e}{\partial x} + e \frac{\partial v_x}{\partial x} + v_y \frac{\partial e}{\partial y} + e \frac{\partial v_y}{\partial y} = 0$$

Rearranging:

$$\left(v_x \frac{\partial e}{\partial x} + v_y \frac{\partial e}{\partial y} + v_z \frac{\partial e}{\partial z} \right) + \left(e \frac{\partial v_x}{\partial x} + e \frac{\partial v_y}{\partial y} + e \frac{\partial v_z}{\partial z} \right) = 0$$

In “del” notation, this becomes:

$$\mathbf{v} \cdot \nabla e + e \nabla \cdot \mathbf{v} = 0$$

□

Appendix B

Stereolithography

The field of rapid prototyping, also known as agile manufacturing, is growing quickly to fill the need for visualizing and testing complex solid parts without the use of time consuming milling processes. These rapid prototyping technologies typically use a layered manufacturing strategy, where the object is built in horizontal sections, one atop another. This strategy allows for complex parts to be built without restrictions on internal cavities and accessibility issues that confront conventional milling methods. [Dolenc 1993] gives an overview of some of the rapid prototyping methods in use today.

One of the more successful layered manufacturing strategies has been the method of stereolithography, the method used for constructing the “hardcopy” of the Happy Buddha model described in Chapter 8. Figure B.1 shows how the process works. The computer model is first sliced horizontally, yielding a stack of polygonal outlines – well-defined regions that separate the inside of the model from the outside. Next, a support platform is raised to the surface in a vat containing a liquid photopolymer that hardens when exposed to ultraviolet light. A sweeper spreads a thin layer of the photopolymer over the surface of the platform, and an overhead UV laser scans and hardens the interior of the polygons in the first slice. The platform then lowers one slice thickness, the sweeper distributes a new layer of photopolymer, and the process repeats for the next slice. In this way, the object is constructed slice by slice. The process for building the Happy Buddha model required about 10 hours. Note how important it is that the model have no holes – such holes would lead to open polygons in the slicing step, and the definition of inside and outside the object would

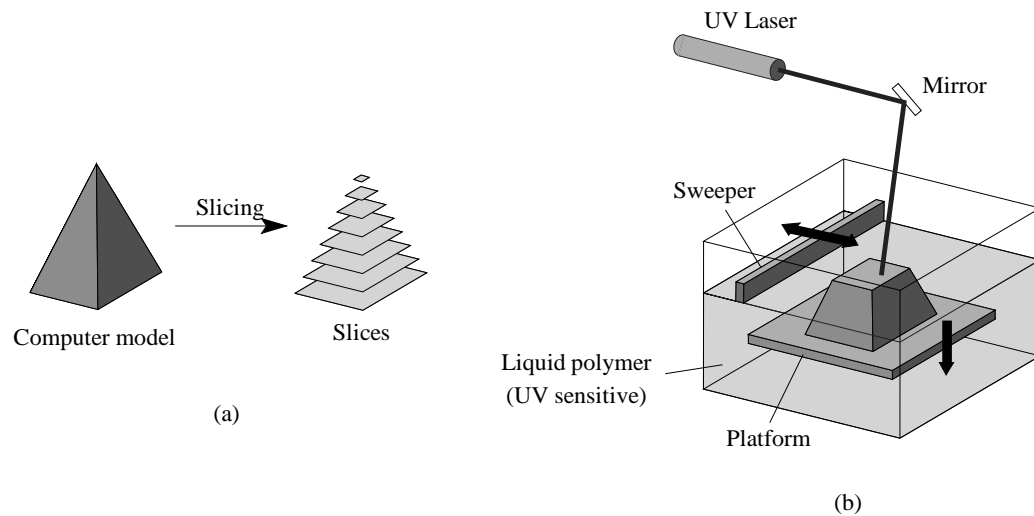


Figure B.1: The stereolithography process. (a) First the computer model is cut into horizontal slices. (b) The interior of each slice is hardened by a laser scanning over a photopolymer. The sweeper delivers even layers across the surface, while the platform lowers after each slice is hardened.

no longer be meaningful. Thus, the contribution of being able to make “watertight” models as described in this thesis is essential to the manufacture of three dimensional replicas of the original model using stereolithography.

When the layering process is finished, the solid object sits immersed in the vat of liquid. The object is then lifted out of the vat, and excess liquid is removed. To save time, the laser may only sweep the interior of the object enough to make it structurally stable, but not completely hard. In this case, the object is “baked” in an ultraviolet oven to complete the hardening process.

The thickness of the stereolithography slices in the Happy Buddha model is about 150 microns. This may seem very accurate, but it still leaves noticeable contouring artifacts between slices. Figure B.2 shows some of these contours. To remove the contours, a post-processing step of bead-blasting and manual sanding is typically required.

One difficulty in constructing models with stereolithography is the problem of overhanging surfaces. If a portion of the surface is not supported from below or from the side, then, when it is hardened, it will sink into the vat of liquid. As a result, a support must be inserted into the computer model before slicing and manufacture. This support is typically very narrow so that it requires little time to create as the model is being built. Further, it comes to a

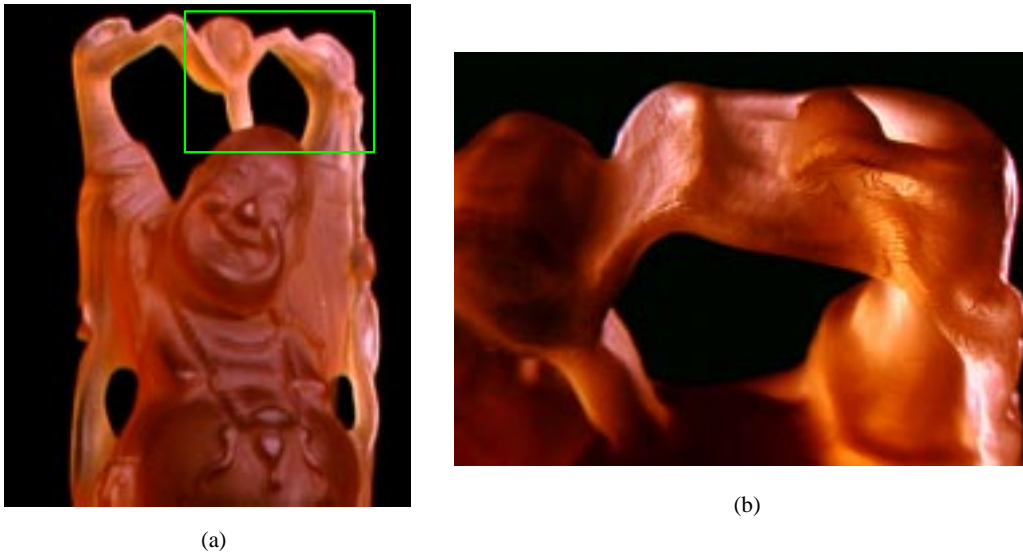
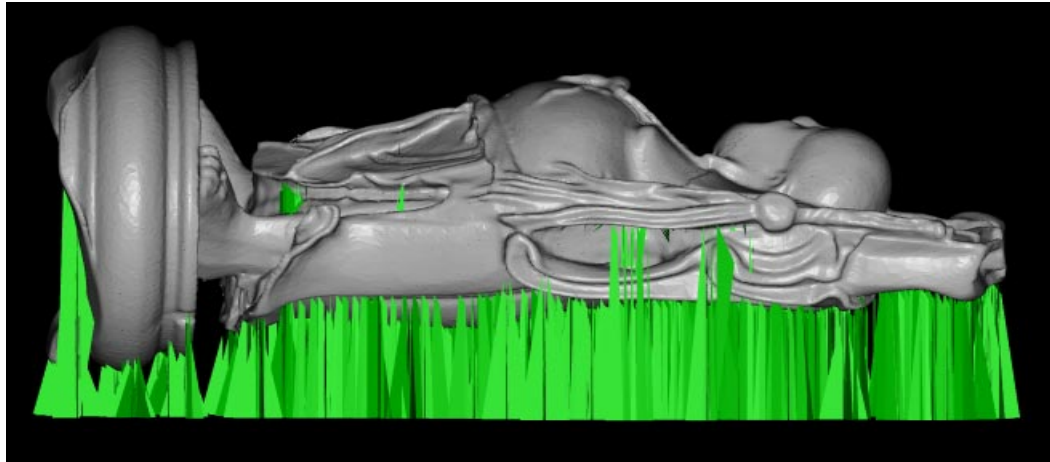
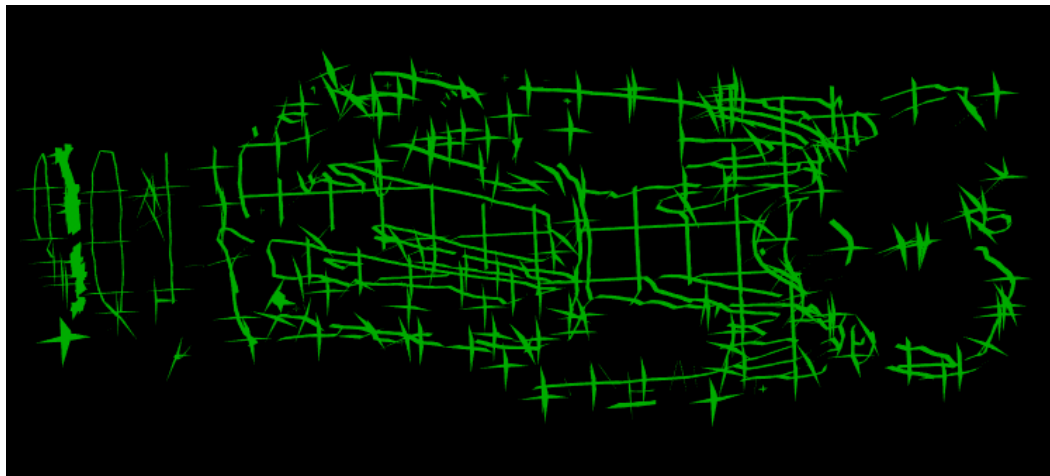


Figure B.2: Contouring due to layered manufacture. (a) The Happy Buddha stereolithography hard-copy. The green rectangle is viewed from a different angle and magnified in (b). Notice the contouring due to the layered manufacturing method. These contours are typically smoothed out with a post-process of bead blasting and hand sanding.

sharp point so that it may be removed easily after the model is finished. In general, a complex model will require a network of supports as shown in Figure B.3.



(a)



(b)

Figure B.3: Supports for stereolithography manufacturing. (a) Shaded rendering of the Happy Buddha model and the supports (show in green) that were needed to handle overhanging surfaces. These supports come to narrow points and break off easily after the model construction is finished. (b) A plan view of the supports by themselves.

Bibliography

- Bajaj, C., Bernardini, F. & Xu, G. [1995]. Automatic reconstruction of surfaces and scalar fields from 3D scans, *Proceedings of SIGGRAPH '95 (Los Angeles, CA, Aug. 6-11, 1995)*, ACM Press, pp. 109–118.
- Baribeau, R. & Rioux, M. [1991]. Influence of speckle on laser range finders, *Applied Optics* **30**(20): 2873–2878.
- Bergevin, R., Soucy, M., Gagnon, H. & Laurendeau, D. [1996]. Towards a general multi-view registration technique, *IEEE Transactions on Pattern Analysis and Machine Intelligence* **18**(5): 540–547.
- Besl, P. [1989]. *Advances in Machine Vision*, Springer-Verlag, chapter 1 - Active optical range imaging sensors, pp. 1–63.
- Besl, P. & McKay, H. [1992]. A method for registration of 3-d shapes, *IEEE Transactions on Pattern Analysis and Machine Intelligence* **14**(2): 239–256.
- Bickel, G., Haulser, G. & Maul, M. [1985]. Triangulation with expanded range of depth, *Optical Engineering* **24**(6): 975–977.
- Boissonnat, J.-D. [1984]. Geometric structures for three-dimensional shape representation, *ACM Transactions on Graphics* **3**(4): 266–286.
- Bracewell, R. [1986]. *The Fourier Transform and Its Applications*, second ed., McGraw-Hill.

- Buzinski, M., Levine, A. & Stevenson, W. [1992]. Performance characteristics of range sensors utilizing optical triangulation, *Proceedings of the IEEE 1992 National Aerospace and Electronics Conference, NAECON 1992*, pp. 1230–1236.
- Chien, C., Sim, Y. & Aggarwal, J. [1988]. Generation of volume/surface octree from range data, *The Computer Society Conference on Computer Vision and Pattern Recognition*, pp. 254–60.
- Connolly, C. I. [1974]. *Cumulative Generation of Octree Models from Range Data*, PhD thesis, Stanford University.
- Connolly, C. I. [1984]. Cumulative generation of octree models from range data, *Proceedings, Intl. Conf. Robotics*, pp. 25–32.
- Curless, B. & Levoy, M. [1995]. Better optical triangulation through spacetime analysis, *Proceedings of IEEE International Conference on Computer Vision*, pp. 987–994.
- Curless, B. & Levoy, M. [1996]. A volumetric method for building complex models from range images, *Proceedings of SIGGRAPH '96 (New Orleans, LA, August 5-9 1996)*, ACM Press, pp. 303–312.
- Dolenc, A. [1993]. Software tools for rapid prototyping technologies in manufacturing, *Acta Polytechnica Scandinavica: Mathematics and Computer Science Series Ma62*: 1–111.
- Dorsch, R., Hausler, G. & Herrmann, J. [1994]. Laser triangulation: fundamental uncertainty in distance measurement, *Applied Optics* **33**(7): 1306–1314.
- Duncan, J. [1993]. The beauty in the beasts, *Cinefex* **55**: 55–95.
- Eberly, D., Gardner, R., Morse, B., Pizer, S. & Scharlach, C. [1994]. Ridges for image analysis, *Journal of Mathematical Imaging and Vision* **4**(4): 353–373.
- Edelsbrunner, H. & Mücke, E. [1992]. Three-dimensional alpha shapes, *Workshop on Volume Visualization*, pp. 75–105.
- Edwards, C. & Penney, D. [1982]. *Calculus and Analytic Geometry*, Prentice Hall, Inc.

- Elfes, A. & Matthies, L. [1987]. Sensor integration for robot navigation: combining sonar and range data in a grid-based representation, *Proceedings of the 26th IEEE Conference on Decision and Control*, pp. 1802–1807.
- Foley, J., van Dam, A., Feiner, S. & Hughes, J. [1992]. *Computer Graphics: Principles and Practice*, Addison-Wesley Publishing Company.
- Francon, M. [1979]. *Laser Speckle and Applications in Optics*, Academic Press.
- Freyburger, B. [1994]. Personal communication. Stanford University.
- Fujii, H., Uozumi, J. & Asakura, T. [1976]. Computer simulation study of image speckle patterns with relation to object surface profile, *J. Opt. Soc. Am.* **66**(11): 1222–1217.
- Gagnon, H., Soucy, M., Bergevin, R. & Laurendeau, D. [1994]. Registration of multiple range views for automatic 3-D model building, *Proceedings 1994 IEEE Computer Society Conference on Computer Vision and Pattern Recognition*, pp. 581–586.
- Garcia, G. [1989]. Development of 3-d imaging systems for postal automation, *CAD/CAM Robotics and Factories of the Future. 3rd International Conference (CARS and FOF '88) Proceedings*, pp. 209–216.
- Goodman, J. [1984]. *Laser Speckle and Related Phenomena*, Springer-Verlag, chapter 1 - Statistical properties of laser speckle patterns, pp. 9–76.
- Goodman, J. W. [1968]. *Introduction to Fourier optics*, McGraw-Hill.
- Grosso, E., Sandini, G. & Frigato, C. [1988]. Extraction of 3D information and volumetric uncertainty from multiple stereo images, *Proceedings of the 8th European Conference on Artificial Intelligence*, pp. 683–688.
- Hausler, G. & Heckel, W. [1988]. Light sectioning with large depth and high resolution, *Applied Optics* **27**(24): 5165–5169.
- Hebert, P., Laurendeau, D. & Poussart, D. [1993]. Scene reconstruction and description: geometric primitive extraction from multiple viewed scattered data, *Proceedings of IEEE Conference on Computer Vision and Pattern Recognition*, pp. 286–292.

- Heeger, D. & Bergen, J. [1995]. Pyramid-based texture analysis/synthesis, *Proceedings of SIGGRAPH '94 (Orlando, FL, July 24-29, 1994)*, ACM Press, pp. 229–238.
- Hilton, A., Toddart, A., Illingworth, J. & Windeatt, T. [1996]. Reliable surface reconstruction from multiple range images, *Fourth European Conference on Computer Vision*, Vol. I, pp. 117–126.
- Hong, T.-H. & Shneier, M. O. [1985]. Describing a robot's workspace using a sequence of views from a moving camera, *IEEE Transactions on Pattern Analysis and Machine Intelligence* **7**(6): 721–726.
- Hoppe, H., DeRose, T., Duchamp, T., McDonald, J. & Stuetzle, W. [1992]. Surface reconstruction from unorganized points, *Computer Graphics (SIGGRAPH '92 Proceedings)*, Vol. 26, pp. 71–78.
- Horn, B. [1986]. *Robot Vision*, The MIT Press.
- Irani, M. & Peleg, S. [1991]. Improving resolution by image registration, *CVGIP: Graphical Models and Image Processing* **53**(3): 231–239.
- Jain, A. [1989]. *Fundamentals of Digital Image Processing*, Prentice Hall.
- Janesick, J., Elliot, T., Collins, S., Blouke, M. & Freeman, J. [1987]. Scientific charge-coupled devices, *Optical Engineering* **26**(8): 692–714.
- Jarvis, R. [1983]. A perspective on range-finding techniques for computer vision, *IEEE Trans. Pattern Analysis Mach. Intell.* **5**: 122–139.
- Juha, M. & Souder, C. [1987]. How 3d imaging simplifies surface mount inspection, *Proceedings of the Technical Program of the National Electronic Packaging and Production Conference - NEPCON West '87*, pp. 558–566.
- Kanade, T., Gruss, A. & Carley, L. [1991]. A very fast vlsi rangefinder, *1991 IEEE International Conference on Robotics and Automation*, Vol. 39, pp. 1322–1329.

- Krishnamurthy, V. & Levoy, M. [1996]. Fitting smooth surfaces to dense polygon meshes, *Proceedings of SIGGRAPH '96 (New Orleans, LA, August 5-9 1996)*, ACM Press, pp. 313–324.
- Lacroute, P. [1995]. Personal communication. Stanford University.
- Lacroute, P. [1996]. Analysis of a parallel volume rendering system based on the shear-warp factorization, *IEEE Transactions on Visualization and Computer Graphics* **2**(3): 218–231.
- Lacroute, P. & Levoy, M. [1994]. Fast volume rendering using a shear-warp factorization of the viewing transformation., *Proceedings of SIGGRAPH '94 (Orlando, FL, July 24-29, 1994)*, ACM Press, pp. 451–458.
- Li, A. & Crebbin, G. [1994]. Octree encoding of objects from range images, *Pattern Recognition* **27**(5): 727–739.
- Lorensen, W. & Cline, H. E. [1987]. Marching cubes: A high resolution 3D surface construction algorithm, *Computer Graphics (SIGGRAPH '87 Proceedings)*, Vol. 21, pp. 163–169.
- Martin, W. & Aggarwal, J. [1983]. Volumetric descriptions of objects from multiple views, *IEEE Transactions on Pattern Analysis and Machine Intelligence* **5**(2): 150–158.
- Montani, C., Scateni, R. & Scopigno, R. [1994]. A modified look-up table for implicit disambiguation of marching cubes, *Visual Computer* **10**(6): 353–355.
- Mundy, J. & Porter, G. [1987]. *Three-dimensional machine vision*, Kluwer Academic Publishers, chapter 1 - A three-dimensional sensor based on structured light, pp. 3–61.
- Nayar, S., Ikeuchi, K. & Kanade, T. [1990]. Shape from interreflections, *1990 IEEE International Conference on Computer Vision*, pp. 2–11.
- Nayar, S., Watanabe, M. & Noguchi, M. [1995]. Real-time focus range sensor, *Proceedings of IEEE International Conference on Computer Vision*, pp. 995–1001.

- Ning, P. & Bloomenthal, J. [1993]. An evaluation of implicit surface tilers, *IEEE Computer Graphics and Applications* **13**(6): 33–41.
- Papoulis, A. [1991]. *Probability, Random Variables, and Stochastic Processes*, third ed., McGraw-Hill.
- Pieper, S., Rosen, J. & Zeltzer, D. [1992]. Interactive graphics for plastic surgery: A task-level analysis and implementation, *1992 Symposium on Interactive 3D Graphics*, pp. 127–134.
- Pito, R. [1996]. A sensor based solution to the next best view problem, *Proceedings of the 13th International Conference on Pattern Recognition*, pp. 941–945.
- Potmesil, M. [1987]. Generating octree models of 3D objects from their silhouettes in a sequence of images, *Computer Vision, Graphics, and Image Processing* **40**(1): 1–29.
- Press, W. H., Flannery, B. P., Teukolsky, S. A. & Vetterling, W. T. [1986]. *Numerical Recipes in C*, Cambridge University Press.
- Rioux, M., Bechthold, G., Taylor, D. & Duggan, M. [1987]. Design of a large depth of view three-dimensional camera for robot vision, *Optical Engineering* **26**(12): 1245–1250.
- Rutishauser, M., Stricker, M. & Trobina, M. [1994]. Merging range images of arbitrarily shaped objects, *Proceedings 1994 IEEE Computer Society Conference on Computer Vision and Pattern Recognition*, pp. 573–580.
- Sato, Y. & Ikeuchi, K. [1996]. Recovering shape and reflectance properties from a sequence of range and color images, *1996 IEEE/SICE/RSJ International Conference on Multi-sensor Fusion and Integration for Intelligent Systems*, pp. 493–500.
- Schey, H. [1992]. *Div, Grad, Curl, and All That*, W.W. Norton and Company.
- Schroeder, W. & Lorensen, W. [1992]. Decimation of triangle meshes, *Computer Graphics (SIGGRAPH '92 Proceedings)*, Vol. 26, pp. 65–70.
- Siegman, A. [1986]. *Lasers*, University Science Books.

- Slevogt, H. [1974]. *Technische Optik*, pp. 55–57.
- Soucy, M. & Laurendeau, D. [1992]. Multi-resolution surface modeling from multiple range views, *Proceedings 1992 IEEE Computer Society Conference on Computer Vision and Pattern Recognition*, pp. 348–353.
- Soucy, M. & Laurendeau, D. [1995]. A general surface approach to the integration of a set of range views, *IEEE Transactions on Pattern Analysis and Machine Intelligence* **17**(4): 344–358.
- Soucy, M., Laurendeau, D., Poussart, D. & Auclair, F. [1990]. Behaviour of the center of gravity of a reflected gaussian laser spot near a surface reflectance discontinuity, *Industrial Metrology* **1**(3): 261–274.
- Stoddart, A. & Hilton, A. [1996]. Registration of multiple point sets, *Proceedings of the 13th International Conference on Pattern Recognition*, pp. 40–44.
- Strand, T. [1983]. Optical three dimensional sensing, *Optical Engineering* **24**(1): 33–40.
- Succi, G., Sandini, G., Grosso, E. & Tistarelli, M. [1990]. 3D feature extraction from sequences of range data, *Robotics Research. Fifth International Symposium*, pp. 117–127.
- Szeliski, R. [1993]. Rapid octree construction from image sequences, *CVGIP: Image Understanding* **58**(1): 23–32.
- Tarbox, G. & Gottschlich, S. [1994]. IVIS: An integrated volumetric inspection system, *Proceedings of the 1994 Second CAD-Based Vision Workshop*, pp. 220–227.
- Taubin, G. [1995]. A signal processing approach to fair surface design, *Proceedings of SIGGRAPH '95 (Los Angeles, CA, Aug. 6-11, 1995)*, ACM Press, pp. 351–358.
- Turk, G. & Levoy, M. [1994]. Zippered polygon meshes from range images, *Proceedings of SIGGRAPH '94 (Orlando, FL, July 24-29, 1994)*, ACM Press, pp. 311–318.

- Wada, T., Hiroyuki, H. & Matsuyama, T. [1995]. Shape from shading with interreflections under proximal light source, *1995 IEEE International Conference on Computer Vision*, pp. 66–71.
- Weinstock, R. [1974]. *The Calculus of Variations, with Applications to Physics and Engineering*, Dover Publications.